UCRL-16168

University of California

Ernest O. Lawrence Radiation Laboratory

A COMPARISON OF THE POSITIVE AND NEGATIVE MUON DECAY SPECTRA IN COPPER

TWO-WEEK LOAN COPY

This is a Library Circulating Copy which may be borrowed for two weeks. For a personal retention copy, call Tech. Info. Division, Ext. 5545

Berkeley, California

DISCLAIMER

This document was prepared as an account of work sponsored by the United States Government. While this document is believed to contain correct information, neither the United States Government nor any agency thereof, nor the Regents of the University of California, nor any of their employees, makes any warranty, express or implied, or assumes any legal responsibility for the accuracy, completeness, or usefulness of any information, apparatus, product, or process disclosed, or represents that its use would not infringe privately owned rights. Reference herein to any specific commercial product, process, or service by its trade name, trademark, manufacturer, or otherwise, does not necessarily constitute or imply its endorsement, recommendation, or favoring by the United States Government or any agency thereof, or the Regents of the University of California. The views and opinions of authors expressed herein do not necessarily state or reflect those of the United States Government or any agency thereof or the Regents of the University of California.

Research and Development

UCRL-16168

UNIVERSITY OF CALIFORNIA

Lawrence Radiation Laboratory
Berkeley, California

AEC Contract No. W-7405-eng-48

A COMPARISON OF THE POSITIVE AND NEGATIVE MUON DECAY SPECTRA IN COPPER

Philip Bert Beilin
(Ph. D. Thesis)

November 28, 1966

A COMPARISON OF THE POSITIVE AND NEGATIVE MUON DECAY SPECTRA IN COPPER

Contents

Abstract iii

I. Introduction. 1

A. Theoretical Free Decay 3

B. Theoretical Bound Decay. 6

C. Experimental Review. 9

II. Experimental Aspects. 16

A. Set-Up and Procedures. 16

B. Magnetic Spectrometer. 21

C. Plastic Scintillation Counters Description 22

D. Scintillation Counters Relative Efficiencies. 24

E. Electronics Discussion 26

III. Calculations. 31

A. Theoretical Spectrum 31

1. Positive Spectrum 31

2. Bound Decay Spectrum. 31

B. Multiple Scattering Effect on Electron Path Length 34

C. Bremsstrahlung 35

D. Ionization Straggling. 37

E. Solid Angle Effect on the Spectrum 40

F. Counter Solid Angle Calculation 42

G. Resolution Function 45

H. Electron Scattering from Spectrometer Pole Tips. 45

I. Pair Annihilation 49

J. Effect of Multiple Scattering on the Solid Angle Calculation 56

K. Background Subtraction. 56

IV. Data Analysis. 58

A. Procedure 58

B. Results 62

C. Comparison of Results and Conclusions 79

Acknowledgments 83

Appendices. 84

A. Theoretical Spectrum. 84

B. Bremsstrahlung. 85

C. Ionization Straggling 97

D. Chi Square Test 98

E. Summary of Systematic Errors. 100

F. OMEGAH Orbit Tracking Program 100

References. 103

A COMPARISON OF THE POSITIVE AND NEGATIVE MUON DECAY SPECTRA IN COPPER

Philip Bert Beilin

Lawrence Radiation Laboratory
University of California
Berkeley, California

November 28, 1966

ABSTRACT

Negative muons from the Berkeley 184-in. Synchrocyclotron were stopped in a copper plate target. The momenta of the decay electrons were measured by an Elbek type wide gap, broad range, magnetic spectrometer. Eleven scintillation counters served to define the focal plane for trajectories from the target, through the spectrometer, to the focal plane. For comparison, positive pions were stopped in the copper target giving rise to positive muons upon their decay. The positrons from the subsequent positive muon decay were momentum analyzed under the same experimental conditions as the electrons.

The measured positive and negative electron momenta spectra are compared to the theoretical predictions taking into account energy loss straggling and various other experimental resolution effects.

Reasonably good agreement was obtained between the positive data and theory. The comparison between the negative decay spectrum and theory seems to be in a less satisfactory state of agreement, the data favoring a faster fall-off with energy at the upper end of the spectrum than theoretically predicted.

I. INTRODUCTION

Although the shape of the electron and positron spectra from the decay of unpolarized negative and positive muons has been studied extensively, (see Table A) the experiments until 1961 dealt exclusively with muon decays occurring in materials of low atomic number. Any influence of the nucleus on the shape of the bound decay spectrum which would cause it to be different from the positive spectrum was expected to be small. For details of the theoretical predictions regarding the bound decay spectra see Section I B.

Since 1961 there have been three prior measurements of the bound decay spectra in medium and high Z materials where the effect of the bound state would be expected to show up more prominently. These experiments are discussed in Section I C and again in Section IV C. An inherent difficulty in measuring the shape of the bound decay spectrum in a medium or high Z material is the necessity of making rather large energy loss corrections. The reason for the selection of a copper target is discussed in detail in Sections III B and III C.

The purpose of this experiment will be first, to measure the shape of both the positive and negative decay spectra with sufficient precision to clearly distinguish between the two spectra and, secondly to make a direct comparison of the experimental results with the theoretical predictions regarding the shapes of the two spectra. Since theory predicts that the largest deviations of the bound decay spectrum from the positive occur on the high momentum side this experiment, utilizing a magnetic spectrometer, was designed to cover this region, namely from 20 MeV/c to 60 MeV/c. Details of the magnetic spectrometer

are discussed in Section II B. The analysis of the experimental data and the results obtained are discussed in Section IV.

A. Theoretical Free Decay

The first experiments established the muon decay mode to be

$$\mu^{\pm} \rightarrow e^{\pm} + \text{two neutral particles.}^{1} \qquad (1)$$

Tiomno, Wheeler, and Rau were the first to make a detailed study of the shape of the muon decay spectrum.[2] Based partially on available experimental evidence and the analogy with nuclear beta decay, they decided to treat the four particles as Dirac particles satisfying the Dirac wave equation. Using standard quantum mechanical perturbation theory they wrote the transition probability, dW, as

$$dW = \left(\frac{2\pi}{\hbar}\right) \left(\frac{4\pi\, p_e^2\, dp_e}{h^6}\right) \left(\frac{1}{dE}\right) \times \int I\, d^3p_\nu \qquad (2)$$

dW is the probability per second of a muon decay in which the electron emerges in the momentum interval p_e to $p_e + dp_e$. The square of the transition matrix element, I, was averaged over the spin of the initial muon and summed over all spin directions of the three decay particles. The integral is over that part of the momentum space of the decay neutrino consistent with energy-momentum conservation. Tiomno et al. considered eq. (1) under two different hypotheses, either

$$\mu^{\pm} \rightarrow e^{\pm} + \mu_o + \nu \qquad (3)$$

or

$$\mu^{\pm} \rightarrow e^{\pm} + 2\nu \qquad (4)$$

(μ_o was chosen to represent a light neutral meson. The first experiments placed an upper limit of 30 m_e on the combined mass of the two neutral

decay particles.) In analogy with nuclear beta decay, only the couplings between the wave functions themselves, exclusive of their derivatives, were considered. Depending on their transformation properties these couplings were called scalar, pseudo-scalar, vector, pseudo-vector (or axial), and tensor.

From results of their calculations Tiomno and Wheeler predicted that, if the two neutral decay particles were neutrinos, a study of the high energy end of the spectrum might provide a means of telling whether or not the two neutrinos were the same. Experiments indicated that the decay electrons did favor the maximum momentum end of the spectrum. The Pauli exclusion principle required the conclusion that the two neutral particles were a) either particle and anti-particle, or b) two different species of neutral particles.

The discovery of parity violations in weak interactions led Bouchiat and Michel to consider the effect of parity violations on the shape of the muon decay spectrum.[3-5] They showed that the spectrum for unpolarized positive muons decaying at rest, P(E), could be represented by the expression

$$P(E) = \frac{Qm_\mu \, p_e E}{4 \, 8\pi^3} \left\{ 3(W-E) + \frac{2\rho}{3} \left(4E-3W - \frac{m_e^2}{E}\right) + 3\eta \, \frac{m_e}{E}(W-E) \right\} \qquad (5)$$

Q, ρ, η, are bilinear combinations of the coupling constants. E, p_e, and m_e are the electron total energy, momentum, and mass, respectively. M_μ is the muon mass and $W = (m_\mu^2 + m_e^2)/2m_\mu$ is the maximum energy of the electron. The neutrino masses have been neglected in the derivation of eq. (5). Neglecting terms in m_e/E, eq. (5) reduces to

$$P(E) = \frac{Q\, M_\mu E^2}{4\ 8\pi^3} [3(W-E) + \frac{2\rho}{3} (4E-3W)] \qquad (6)$$

The Two-Component theory of the neutrino and the Universal V-A theory made definite predictions regarding the magnitude of the parameter, ρ, known as the Michel parameter.[6,7] If the neutrinos emitted in muon decay were identical, $\rho = 0$, but if they are distinguishable, $\rho = 3/4$.

Eq. (5) was derived assuming the decay was a local interaction between four fermions with non-derivative type couplings. Deviations from $\rho = 3/4$ have been interpreted as possible evidence for a non-local interaction.[8-10] The range of this interaction is characterized by m_W^{-1}, where m_W is the mass of the particle exchanged between the pairs of fermions. Work by Lee and Yang indicated that the presence of such a particle could be accounted for provided the Michel parameter was represented by the following expression

$$\rho = 3/4 + 1/3 \left(\frac{m_\mu}{m_W}\right)^2$$

where m_μ and m_W are the muon and exchange particle masses, respectively.[8]

Before eq. (6) can be compared with experimental data, corrections for internal radiative processes must be made. These processes, involving the emission and reabsorption of virtual photons, have been discussed by Kinoshita, Sirlin, and others.[11-14] In effect, the numbers of electrons emitted at the extreme upper end of the spectrum are reduced. These radiative corrections result in the ρ value being 5.6% higher when experiment and theory are compared in the region $0 < p_e/p_{e.max} < 0.95$. The details of the correction are discussed

in Appendix A.

B. Theoretical Bound Decay

Until now only the shape of the unpolarized free decay spectrum has been discussed. Porter and Primakoff were the first to discuss the effect of Bohr orbit binding on negative muon decay.[15] They showed that the orbital motion of the bound muon would cause a Doppler smearing of the high momentum end of the spectrum, which shifts the maximum momentum upward. The order of magnitude smearing based on the conservation laws was given as

$$(p_{e-})_{max} \approx (p_{e+})_{max} (1 + Z\alpha) \; (\alpha = 1/137) \qquad (7)$$

for lowest Bohr orbit binding in a nucleus of charge Ze. In their calculation of the shape of the negative decay spectrum using standard perturbation methods, bound state wave functions were used for the μ^-, Dirac plane-wave functions for the e^-, and Majorana plane-wave functions for the neutrinos. The nucleus was treated as if it were a point charge.

Uberall pointed out that, since the bound muon decays close to the nucleus, the electron wave function could not be represented by a plane wave.[16] It must be represented by a relativisitc wave function having an amplitude larger than a plane wave function near the nucleus. The large overlap between the nuclear and electron wave functions should result in a Coulomb attractive potential. In escaping from this potential the electrons would appear with reduced energy. Uberall asserted that the most significant deviation of the bound from the free spectrum should occur at the upper end of the spectrum contrary to the predictions of Tenaglia.[17] Uberall obtained the electron wave function,

$\psi_e(r)$, by iteration of the Dirac wave equation

$$(i\,\vec{\alpha}\cdot\vec{\nabla} + p - V(r))\,\psi_e(r) = 0 \tag{8}$$

using for the nuclear potential, $V(r)$, the Yukawa potential

$$V(r) = -\frac{1}{r}\,\gamma_e \exp(-\beta r) \tag{9}$$

where

$$\gamma_e = Z/137 \tag{10}$$

Later in his calculation Uberall let the parameter $\beta \to 0$ so that $V(r)$ would coincide with the Coulomb potential.

Since the Dirac equation with a Coulomb potential cannot be solved in a closed form solution, Gilinsky and Mathews chose to use Sommerfeld-Maue type wave functions as a simple closed form approximation to the electron wave function. They represented the muon by a relativistic wave function, $\psi_\mu(\vec{X})$, where

$$\psi_\mu(\vec{X}) = \frac{1}{(4\pi)^{1/2}}\,[g(r) + f(r)\; i\,\vec{\alpha}\cdot\hat{X}]\; U_o \tag{11}$$

and

$$g(r) = \frac{2}{(1+\Lambda^2)^{1/2}}\;\mu^{3/2}\,e^{-\mu r} \tag{12}$$

$$f(r) = \Lambda\, g(r) \tag{13}$$

The parameters μ and Λ were adjusted to give best fits to numerical solutions of the Dirac equation with the potential of a uniformly charged nucleus.

Huff noted, however, that the use of the Sommerfeld-Maue wave

function for electrons and the fitted muon wave functions of Gilinsky and Mathews became less accurate for medium and high Z elements.[19] Huff considered the polar form of the Dirac equation

$$\begin{pmatrix} Q - V(r) - 1 & -\frac{r}{dr} - \frac{2}{r} \\ \frac{d}{dr} & Q - V(r) - 1 \end{pmatrix} \begin{pmatrix} V^{+} \\ V^{-} \end{pmatrix} = 0 \qquad (14)$$

$$\begin{pmatrix} E - V(r) & \frac{d}{dr} + \frac{j}{r} \\ -\frac{d}{dr} + \frac{j}{r} & E - V(r) \end{pmatrix} \begin{pmatrix} W_j^{+} \\ W_j^{-} \end{pmatrix} = 0 \qquad (15)$$

$V^{\pm}$ and $W^{\pm}$ are the muon and electron (positive and negative state) wave functions, respectively.

The muon wave functions, $V^{\pm}$, and the binding energies, Q, were obtained from work by Ford and Wills who fitted the nuclear charge distributions to electron scattering data.[20] In constructing the electron wave functions $W_j^{\pm}$, the nuclear charge distribution was replaced by a uniformly charged sphere whose total charge and r.m.s. radius, r_o, were chosen to be equal to those used by Ford and Wills. The nuclear potential, V(r), was represented as

$$V(r) = -\left(\frac{Z\alpha}{r_o}\right)\left(\frac{3}{2} - \frac{1}{2}\frac{r^2}{r_o^2}\right), \; r < r_o \qquad (16)$$

$$V(r) = -\frac{Z\alpha}{r}, \quad r > r_o \qquad (17)$$

The largest computational error in Huff's calculations results from experimental uncertainties regarding the nuclear charge distribution

and included the effect of replacing the nucleus by a uniformly charged sphere in computing the electron wave functions. This error is estimated to be 1% to 2%. Other approximations in Huff's calculation include setting the electron and neutrino masses equal to zero and the neglect of nuclear recoil. A more serious neglect to date has been the fact that no one has computed the effect on the shape of bound spectrum of the internal radiative corrections which have been shown to be so important in free decay.

Calculations by Kruger and Rothleitner also give results closely comparable to those of Huff.[21] Other calculations have also been made by M. V. Terent' ev.[22]

C. Experimental Review

Since the difference between the bound and free decay spectra increases with atomic number, A, an experiment to measure the shape of the bound spectrum should employ as high a Z material as is experimentally feasible. Early experiments measuring the negative muon decay spectrum were all done in low Z material where any difference in the shape from the free decay spectrum would be small.[1, 23,27,28,35]

The first accelerator experiment, using only negative muons rather than a mixture of positive and negative cosmic ray muons, was that by Sargent et al.[27] Negative muons were stopped in a high pressure hydrogen-filled diffusion cloud chamber and their endings scanned for decay electrons. The electron momenta were determind from curvature and angle measurements and the value of the magnetic field. 35 ± 15% of the muons were estimated to decay from the K shells of the 0.4% impurities

of oxygen, nitrogen, and carbon in the gas. The experimental results were compared with Michel's spectrum modified by the binding effect as treated by Porter and Primakoff. A value of 0.68 ± 0.11 for the Michel parameter was obtained. The uncertainty of the result was due mainly to the small sample of events analyzed.

A helium bubble chamber exposed to a K^- beam provided a large number of negative muon decays for the Duke experimental group of Block et al.[35] The principle contributors to the 5% error in the average momentum measurement were due to a) curvature measurements and b) multiple scattering. The effect of binding on the negative muon, as computed by Uberall, introduced an estimated spread of 1-1/2% at the upper end of the momentum spectrum. The Duke group obtained a value of 0.751 ± 0.034 for the Michel parameter lending additional support to the two component and universal V-A theories.

Since 1961 the negative spectrum for higher Z values has been measured by Bergeson in Al, Fe, and Zn; by Nielsen in Fe and Pb; and by Culligan et al., in Fe.[38,39,40]

The experiment by Bergeson utilized a CCl_4 total absorption Cerenkov counter in order to insure insensitivity to neutrons. The decay electron energy was determined by pulse height calibration using artificial pulses and fast muons. Bergeson concluded, however, that the experimental spectra lacked sufficient accuracy to compare with Huff's predictions.

The experiment by Culligan, et al., utilized a large (20 cm x 20 cm) NaI(Tℓ) counter to measure the energy distribution of the decay electrons. The NaI counter had a resolution of 17% for 50 MeV electrons,

with a 5 MeV low energy cut-off. The Fe target in which the muons decayed was ~ 1.8 g/cm^2 in the direction of the NaI detector. The experimental Fe spectrum was compared with the theoretical predictions of Uberall. There appeared to be a considerable excess of low energy events.

Since the region of greatest difference in shape between free and bound spectra occurs on the high momentum side of the spectrum peak my experiment was designed to cover this region. The magnetic spectrometer current was adjusted until the upper end of the decay spectrum appeared in the high momentum end of the array of eleven focal plane counters. The choice of the thickness of the copper target, 2.8 g/cm^2, was dictated by the conflicting requirements of a high Z target versus adequate electron decay rates and low energy loss corrections. For purposes of comparison, the free decay spectrum was obtained by stopping positive pions in the target and observing the positron decay spectrum. The experimental results were compared with the theoretical predictions of Huff modified by energy loss corrections and experimental resolution effects.

Table A immediately following, contains a complete summary of the many experiments which have measured the muon decay spectrum, both positive and negative.

Table A. Experiments

	Author	(Ref.)	Year	Source	Method	Charge	No. Events	ρ
1.	R. Leighton C. Anderson A. Seriff	(1)	1949	cosmic rays	cloud chamber	+,-	75	0.4
2.	A. Lagarrique C. Peyrou	(23)	1951	cosmic rays	cloud chamber	+,-	150	0.4
3.	H. Bramson W. Havens A. Seifert	(24)	1952	accel.	emulsions	+	301	0.41 ± 0.13
4.	H. Hubbard	(25)	1952	accel.	cloud chamber	+	400	0.26 ± 0.26
5.	J. Vilain R. Williams	(26)	1954	accel.	cloud chamber	+	280	0.50 ± 0.13
6.	C. Sargent M. Rinehart L. Lederman K. Roger	(27)	1955	accel.	cloud chamber	-	415	0.68 ± 0.11
7.	A. Bonnetti R. Levi-Setti M. Panetti G. Rossi E. Tomasini	(28)	1956	cosmic rays	emulsions	+,-	506	0.57 ± 0.14

	Author	(Ref.)	Year	Source	Method	Charge	No. Events	ρ
8.	K. Crowe R. Helm G. Tautfest	(29)	1956	accel.	double focusing spectrometer	+		0.62 ± 5%
9.	L. Rosenson	(30)	1958	accel.	cloud chamber	+	1300	0.67 ± 0.05
10.	A. Vaisenberg	(31)	1959	accel.	nuclear emulsion	+		0.72 ± 0.10
11.	H. Anderson T. Fujii R. Miller L. Tau	(32)	1959	accel.	magnetic spectrometer	+		0.74 ± 0.03
12.	W. Dudziak R. Sagane J. Vedder	(33)	1959	accel.	spiral orbit spectrometer	+		0.72 ± 8%
13.	R. Plano	(34)	1960	accel.	bubble chamber	+	9213	0.780± 0.025
14.	M. Block G. Fiorini T. Kikuchi	(35)	1960	accel.	bubble chamber	-	2276	0.764± 0.032**
15.	A. Vaisenberg V. Smirnit-skii E. Kolganova	(36)	1960	accel.	nuclear emulsion	+	3580	0.66 ± 0.07
16.	H. Kruger	(37)	1961	accel.	double focusing spectrometer	+		0.774± 0.042

Author	(Ref.)	Year	Source	Method	Charge	No. Events	ρ
17. H. Bergeson	(38)	1961	cosmic rays	Cerenkov counter	+,-		
18. G. Culligan D. Harting N. Lipman G. Tibell	(39)	1961	accel.	NaI counter	+,-	2000 + and -	
19. L. C. Nielsen	(40)	1962	cosmic rays	Cerenkov counter	+,-		
20. A. Hogan	(41)	1962	cosmic rays	liquid scintillator	+,-		0.77 ± 0.03
21. J. Barlow P. Booth L. Carroll G. Court J. Davies D. Edwards R. Johnson J. Wormald	(42)	1964	accel.	magnetic spectrometer	+,-		$\rho(\mu^+) =$ .661 ± 0.016 $\rho(\mu^-) =$ .64 ± 0.04
22. M. Bardon P. Norton J. Peoples A. Sachs	(43)	1965	accel.	sonic spark chambers	+	8×10^5	0.747 ± 0.005
23. Bounin Ehrlich Fryberger Powers B. Sherwood V. Telegdi	(43a)	1965	accel.	wire chambers	+	10^5	*0.746 ± 0.01

Author	(Ref.)	Year	Source	Method	Charge	No. Events	ρ
24. A. Vaisenberg E. Pesotskaya V. Smirnit-skii	(41a)	1962	accel.	nuclear emulsion	+ -	2969 604	0.68
25. J. B. Pontecorvo R.M. Sulyaev	(44)	1965	accel.	diffusion chamber	-		0.867 ± 0.035

*Preliminary

**1962 Nuovo Cimento V. 23, ρ = 0.751 ± 0.034

II. EXPERIMENTAL ASPECTS

A. Set-Up and Procedures

Pions produced by 740 MeV protons impinging on an internal beryllium target were momentum selected by the magnetic field of the 184" Cyclotron (see Figure 1). Upon leaving the vacuum tank of the Cyclotron through a thin aluminum window the pions passed through an 8" quadrupole doublet magnet, then through a slit in the meson wheel, and emerged into the experimental area. Here the beam was deflected toward the experimental target by means of a bending magnet and then focussed once more by a second quadrupole doublet. The beam now passed through a four counter telescope. The first three counters μ_1, μ_2, and T monitored the incident beam intensity. These three, together with $\overline{\mu}_4$ in prompt anti-coincidence, gave the stopping rate. Differential range curves were obtained by varying the thickness of polyethylene (CH_2) placed between counters μ_1 and μ_2. See Figures 2 and 3. In the positive spectrum measurement, the range was 24.5 g/cm^2 polyethylene (CH_2) for stopping positive pions in the copper target while in the negative measurement the range was increased to 35.0 g/cm^2 of polyethylene to stop negative muons.

The mean momentum of the incident beam was 195 MeV/c as determined from the differential range curves. The copper plate which served as the target was 4" x 7" x 1/8". It was oriented so that the downstream normal to its surface was approximately 50° from the incident beam direction, thus presenting a thickness of 3.7 g/cm^2 in the beam direction. This particular orientation was chosen to optimize conflicting requirements, i.e., stopping as much of the beam as possible,

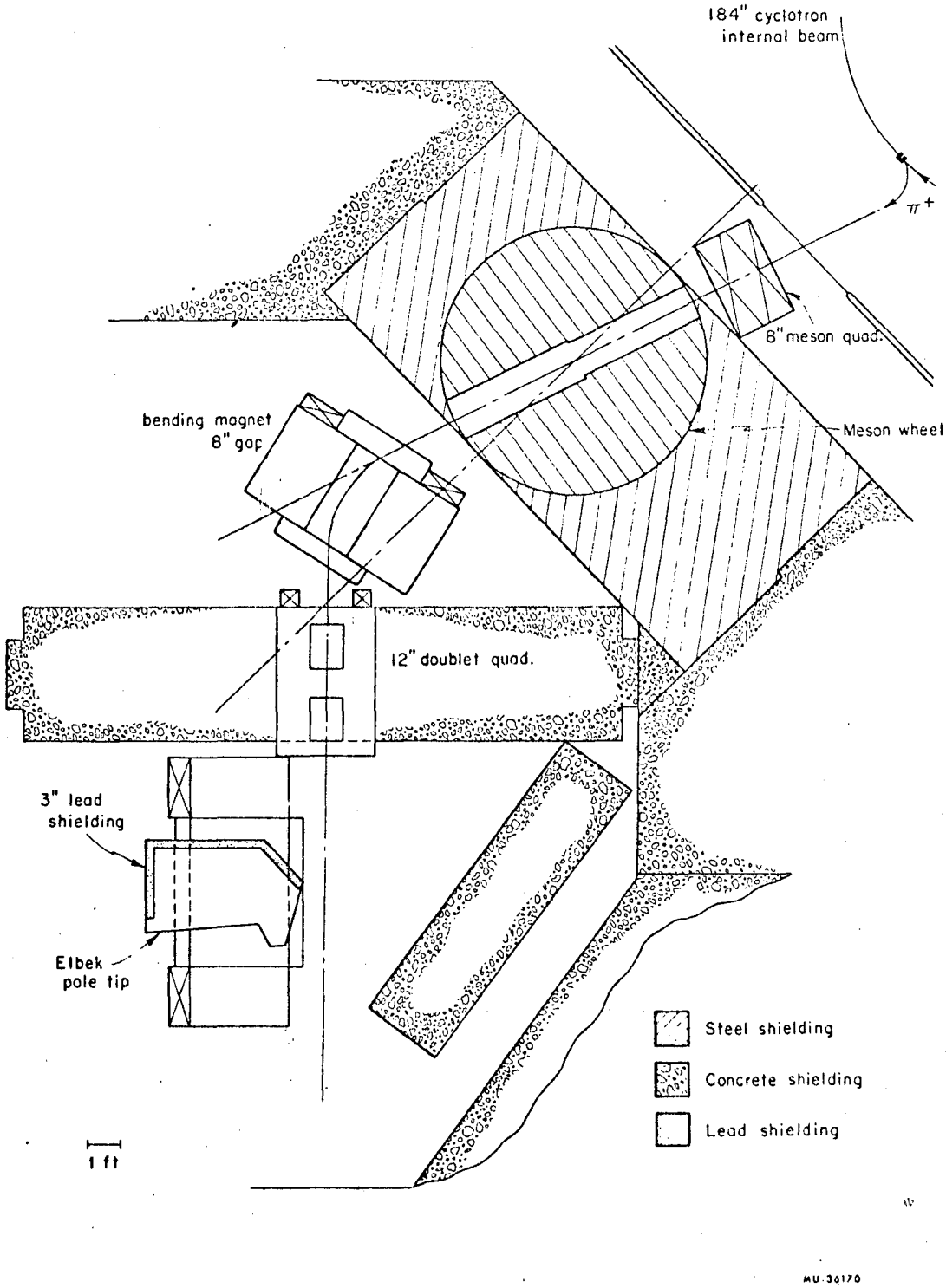

Fig. 1. Experimental set-up in the meson beam cave of the Berkeley 184" Synchrocyclotron.

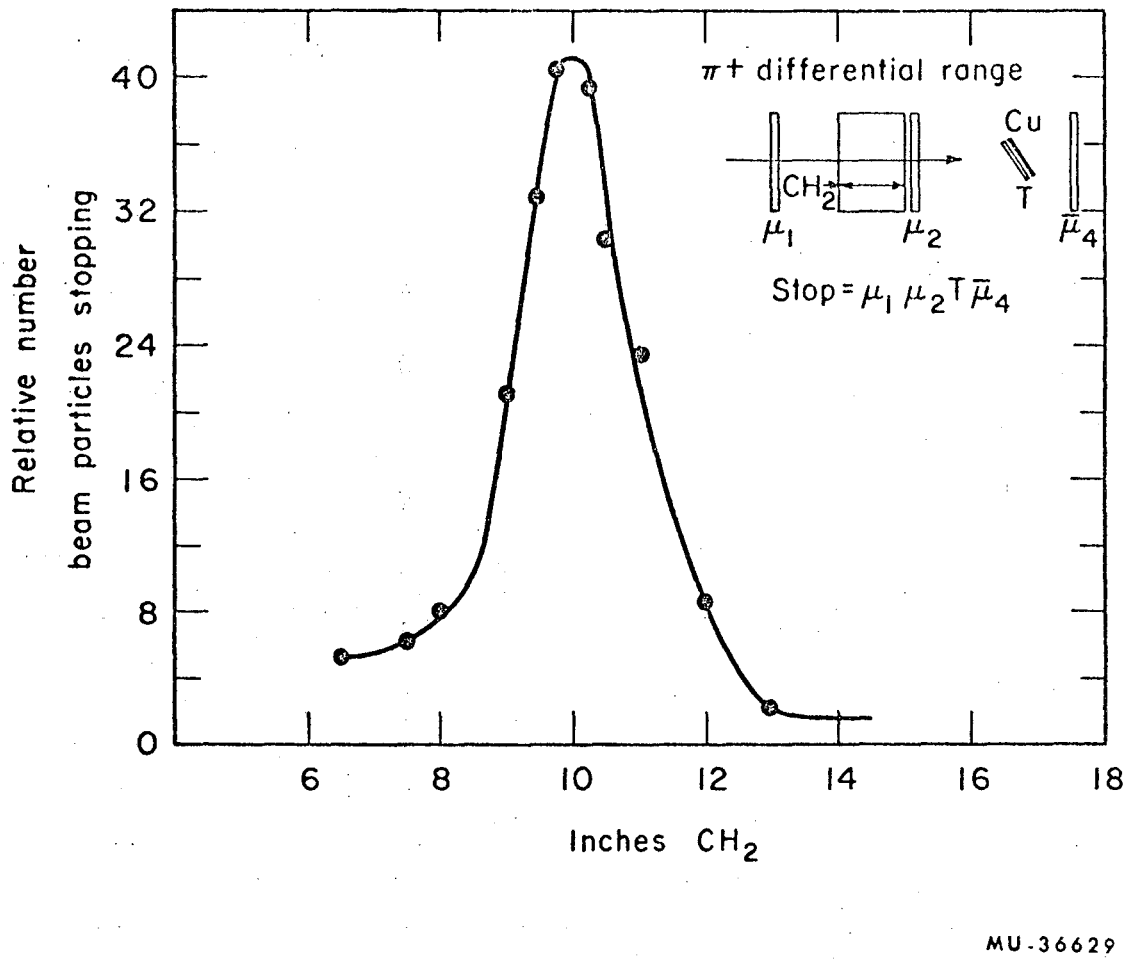

Fig. 2. Differential range curve for stopping positive pions.

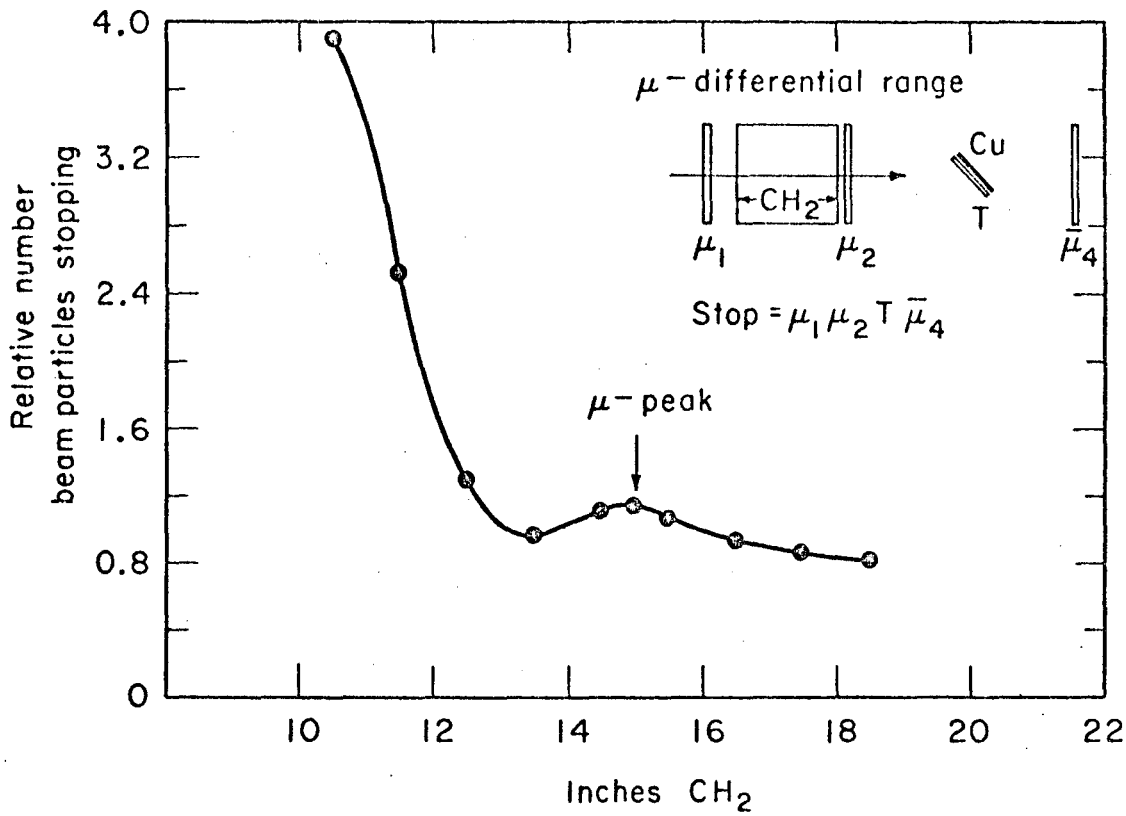

MU-36628

Fig. 3. Differential range curve for stopping negative muons.

and minimizing the energy losses which the decay electrons undergo upon leaving the copper plate. The choice of copper as a target was likewise a compromise between several factors. The largest differences between the positive and negative decay spectra lie on the high momenta side of the decay spectra and these differences get larger as Z increases. See Figure 8. On the other hand as Z gets larger the fraction of bound muons in the 1s shell that escape nuclear capture decreases. In the case of copper the fraction that decays is only about 6%.[45] Another important factor is that as Z increases the energy loss corrections become larger and consequently more important. This dictates the necessity of using as thin a target as possible consistent with obtaining a useful stopping rate. Counter T which had the same physical dimensions as the copper target was immediately in front of the copper. Counter T, as part of the incident beam telescope, served to define particles entering the target. It also served as part of the decay event telescope composed of T, β_A, and any one of counters β_1, β_2, β_3 and β_4. (See Fig. 4.)

The magnetic field in the spectrometer was adjusted at the beginning of each run with the aid of a Varian F-8 Nuclear Fluxmeter. The fluxmeter probe holding a water sample, was positioned in a marked region in the central region of the spectrometer gap approximately in the median plane of the pole tip gap. A Hewlett-Packard 524B frequency counter was used to monitor the Varian transmitter frequency and permitted reading the frequency to five significant figures. Setting the frequency meter at the reading corresponding to the desired magnetic field the current in the magnet coils was then

adjusted until the resonant condition was achieved. This condition required the proper pattern to be displayed on the Varian scope. The probe was subsequently withdrawn from the gap. The regulator on the generator furnishing current to the spectrometer controlled current fluctuations to better than one part per 10^4 over the duration of the data taking runs.

B. Magnetic Spectrometer

The design for the spectrometer pole tip shape was selected on the basis of its favorable characteristics such as relatively large solid angle, small second order focal plane aberrations and a reasonably long, linear focal plane. Details regarding the design of the spectrometer may be obtained in an article by J. Borggreen, B. Elbek, and L. Perch Nielsen.[46] The magnet gap was 8-1/2". An "H" type magnet was modified by removing one side of the steel yoke and replacing the rectangular pole tips, with the special Elbek pole tips. This allowed the decay particles from the source to pass through the magnet and emerge toward the focal plane counter arrays. The magnetic field in the spectrometer was measured by the integrator search coil method. The median plane as well as planes 2.25" and 3.28" off the median plane, both above and below were measured. In each plane the distance between measured points was one inch.

In the vicinity of the pole tip edges plots of lines of constant field value indicated that these lines were parallel to the pole tip edges over most of their length, except at the extreme corners. The geometry of the experiment was designed to keep possible particle

orbits well away from these corners.

For details of the magnetic spectrometer and scintillation counters geometry, refer to Figure 4. Note that the upper edge of the pole tip is represented by a broken view.

C. Plastic Scintillation Counters Description

All the scintillators were made by the Lawrence Radiation Laboratory. By weight the composition is 97.5% polystyrene solvent, 2.5% p-terphenyl activator, and .03% tetraphenylbutadiene shifter. There is an additional .01% zinc stearate used to prevent surface stress formation in production.

The dimensions of the beam telescope counters μ_1, μ_2, T, and $\overline{\mu}_4$ were 9" x 9" x 1/4", 8" x 8" x 1/4", 4" x 7" x 1/8", and 9" x 9" x 1/4" respectively. The decay electron telescope consisted of counters β_A, β_1, β_2, β_3, β_4 as well as the T counter which was required in both telescopes. The dimensions of β_A were 6" x 8" x 1/16" while the counters β_1, β_2, β_3, β_4 were all 1-1/2" x 8" x 1/16". The focal plane counter array consisted of a front row of eleven counters each 3-1/2" x 8" x 1/4". This front row was backed by two more rows of counters. Counters 12, 13, 14, and 15, in the second row, were 10-3/4" x 8" x 1/4", 12" x 8" x 1/4", 12" x 8" x 1/4", and 10-3/4" x 8" x 1/4" respectively. The third row counters 16, 17, and 18 were 14-3/4" x 8" x 1/4", 16-1/4" x 8" x 1/4", and 14-3/4" x 8" x 1/4" respectively.

The counters all used RCA 6810A 14 stage photo-multiplier tubes. The plane of the scintillators were oriented normal to the median plane of the magnetic spectrometer. Their relative position may be seen in Figure 4.

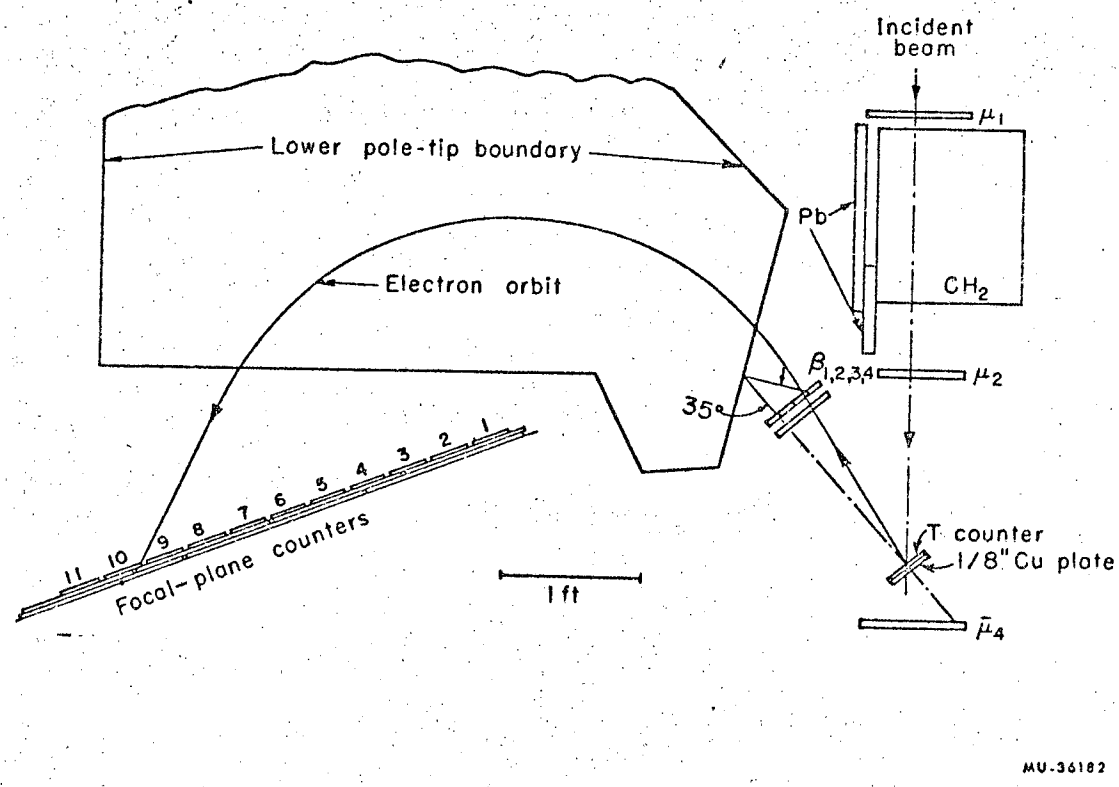

Fig. 4. Layout of magnetic spectrometer and scintillation counters.

D. Scintillation Counters Relative Efficiencies

The focal plane counter efficiencies were measured with the aid of two scintillation counters utilizing the time of flight technique. The first reference counter was placed upstream in the beam at the entrance to the bending magnet while the second reference counter was placed (in the beam) far downstream against the rear wall of the cave area. The difference in time-of-flight between pions and muons was about two nanoseconds while between electrons and muons the difference was approximately five nanoseconds. The resolution of the zero crossing coincidence circuit designed by Nunamaker and Bjerke[47] was of the order of one nanosecond. The delays of the two reference counters were set to count only electrons. The delay of the focal plane counter was then adjusted so that the signal from the focal plane counter was in coincidence with the "doubles" coincidence signal from the two reference counters. The "triples" to "doubles" ratio is taken to be the efficiency,

$$Eff_i = \frac{(TF_1)\cdot(TF_2)\cdot(F.P._i)}{(TF_1)\cdot(TF_2)}$$

Each of the eighteen focal plane counters was positioned immediately in front of the second reference counter.

The signal from each focal plane counter was passed through the same electronic channels it normally went through during the data taking runs. Hence the overall electronic and counter efficiency was measured.

The efficiency of each of the front eleven focal plane counters was then multiplied by the product of the efficiencies of the second

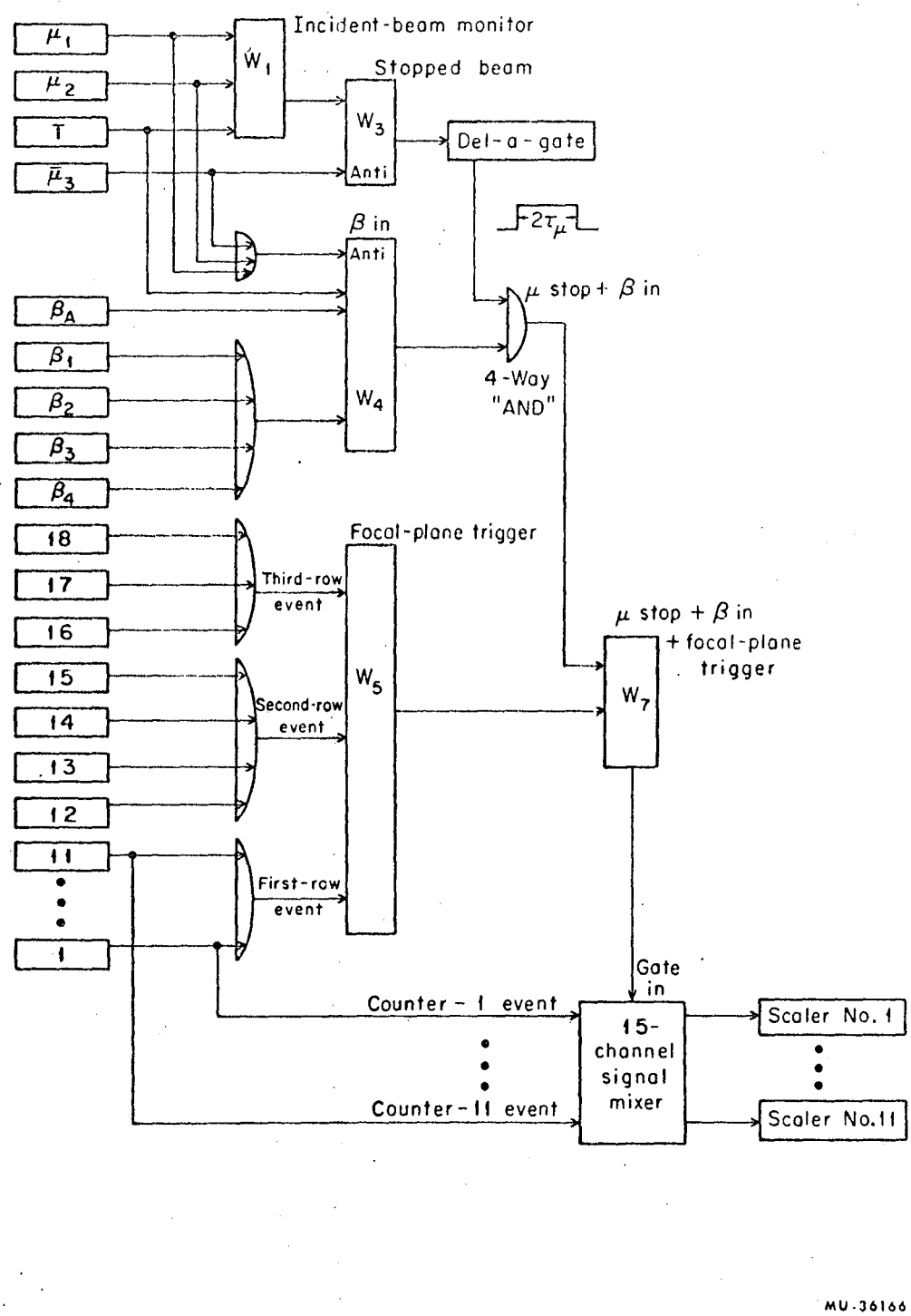

Fig. 5. Block logic diagram of electronics.

and third row counters directly behind each front row counter. The second and third row efficiencies were weighted by the fraction of the area of the front row counter they covered. The final result is indicated in Table B.

Table B. Focal Plane Counter Efficiencies

	1	2	3	4	5	6	7	8	9	10	11
Eff(%)	95.0	95.3	90.9	93.4	95.6	85.	93.2	100.0	89.0	77.5	87.8

The triples to doubles ratios were measured in two successive runs of 5000 counts each. The two runs repeated to within 2%. However, since the two reference counters only subtended a small fraction of the area of the much larger counters on the second and third rows, the triples to doubles ratios did not represent the efficiency averaged over the entire scintillator surface. Consequently, an error of 4% was assigned to the effective efficiency of the front row counters given in Table B.

E. Electronics Discussion

The target incident beam particles were detected by a scintillation counter telescope consisting of counters μ_1, μ_2 and T. The pulses from these counters were passed through constant delay discriminators and then suitably delayed by cable delay boxes so as to arrive together at the three-fold transistorized Wentzel coincidence circuit labeled in Fig. 5 as W_1. The output of W_1, after passing through a subsequent constant delay discriminator was fed into a 10 MC

scalar and constituted the incident beam monitor.

Counter $\overline{\mu}_4$ placed 5 inches downstream from the copper target served together with counters μ_1 and μ_2, and T to give a $\mu_1\ \mu_2\ T\ \overline{\mu}_4$ output from W_3 signaling a stopped particle signal. The stopped particle was a positive pion for the case where the positive spectrum was to be determined while for the negative spectrum negative muons were stopped. In each case the range of polyethylene degrader placed between counters μ_1 and μ_2 was varied to provide the maximum stopping rate. The stopping rate given by coincidence unit W_3 was also monitored by a count rate meter providing a constant check on the incident beam rate. The stopped signal fired a del-a-gate which provided a gate whose width was adjusted to correspond to approximately two decay lifetimes of the muon. In the positive case the gate width was 4.4 μs while in the negative case it was set at 350 ns. This gate was applied to a 4-way "AND" circuit after a 10 ns delay to allow prompt scattered beam particles which might enter the spectrometer to disappear. The 4-way "AND" would then only fire if a decay event occurred within the two lifetime gate width.

The decay electron entering the magnetic spectrometer was signaled by the firing of the counters T, β_A, and any one of the four smaller counters β_1, β_2, β_3, or β_4. To further minimize the chance that a beam particle would scatter into the β telescope beam counters μ_1, μ_2, and μ_4 were placed in anti-coincidence with the T and β counters in the coincidence circuit W_4. The output of W_4 was then fed into the 4-WAY "AND" circuit. Provided the W_4 signal arrived during the two lifetime long gate being applied by the stopped signal event

the 4-WAY "AND" circuit would fire. The output of the 4-WAY "AND" circuit signaled that a muon had stopped and that within two decay lifetimes the decay electron had entered the magnetic spectrometer.

On the focal plane of the spectrometer three rows of scintillation counters looked for the decay electron associated with a stopped muon and entering electron signal. The outputs of each row of counters were fed into mixer circuits which fired whenever one or more pulses were received. The criteria used to signify the occurrance of a focal plane event was that at least one counter in each of the three rows fired and the three mixer outputs feeding the coincidence circuit W_5 occurred within its resolution time.

The 4-WAY "AND" output together with the W_5 output are fed into another coincidencecircuit W_7. A "good event" trigger is defined as a coincidence output from W_7. Namely, a "good event" trigger is a muon stop signal, an associated electron decay, and at least one counter on each of the three focal planes firing. These "good event" triggers fired a tunnel diode discriminator. Two outputs from this discriminator gated on a fifteen channel signal mixer. The gate was 30 nanoseconds long and was determined by the extra cable delay of one of the two cables from the tunnel diode discriminator to the signal mixer. The shorter delay cable pulse opened the gate while the second cable pulse provided the signal closing it.

The front row of eleven focal plane counters besides being part of the focal plane trigger signal also determined where the decay electron crossed the focal plane. The single output from each focal plane counter was fed into a constant delay discriminator. One of

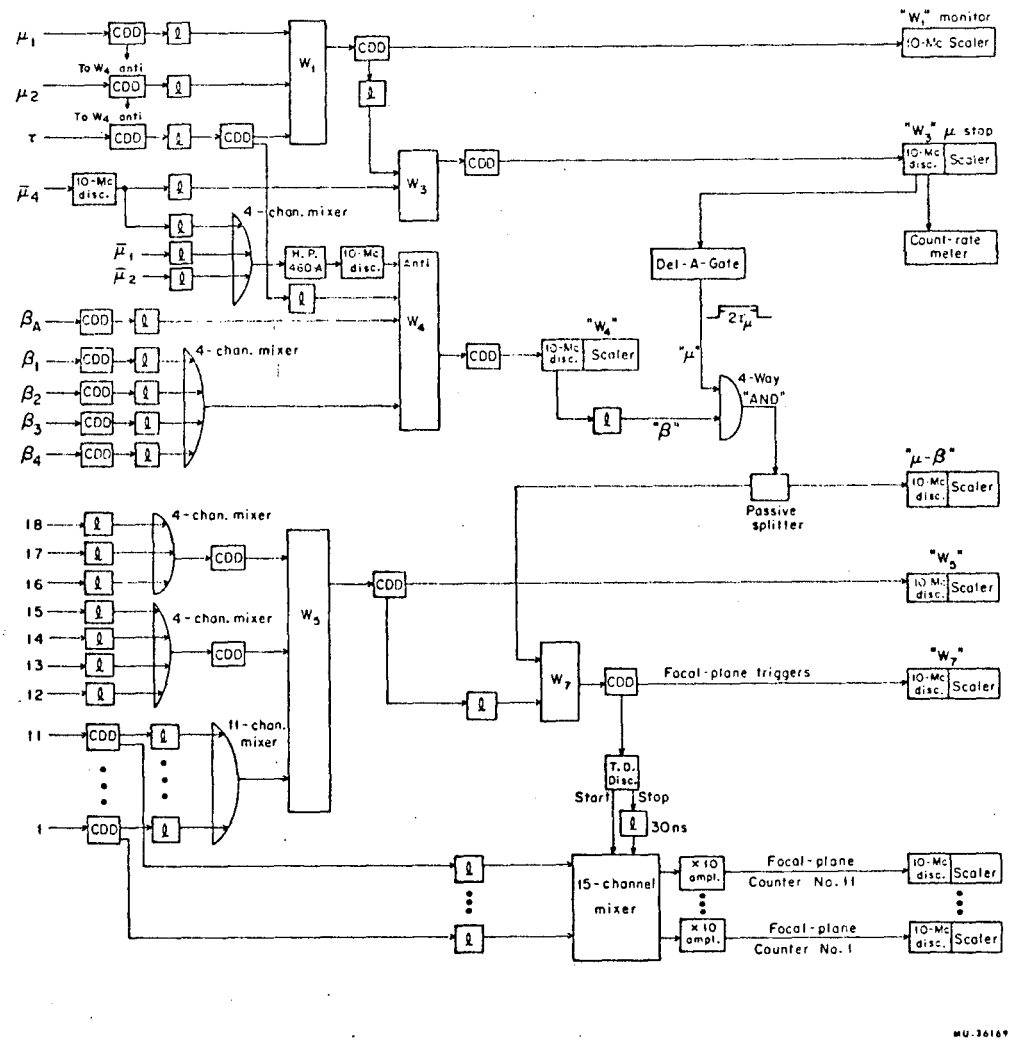

Fig. 6. Electronic circuit diagram details. CDD refers to constant delay discriminator and ℓ denotes delay box. The characteristics of the fast electronic circuits are discussed in the Lawrence Radiation Laboratory Counting Handbook, UCRL-3307 (Rev.) while the various nanosecond logic circuits are discussed in the engineering note EE-883 by S. Klezmer, also of Lawrence Radiation Laboratory.

the two discriminator outputs went into the focal plane trigger requirement. The second discriminator output was delayed until it would arrive at the 15 channel signal mixer when the 30 ns gating signal was being applied. Those pulses from the front eleven focal plane counters getting through the 15 channel signal mixer were considered "good events" and were sent directly into a bank of eleven scalers, one for each of the eleven counters.

III. CALCULATIONS

A. Theoretical Spectrum

1. Positive Spectrum

The expression, equation (6), for unpolarized positive muons, decaying at rest, may be rewritten as

$$R_1^+(X) = 4X^2\{3(1-X) + 2\rho_M[(4/3)\ X-1]\} \tag{18}$$

where X is the electron momentum in units of the maximum electron momentum, 52.83 MeV. The constants in front of the momentum dependent portion of equation (6) have been absorbed by the left hand term $R_1^+(X)$. ρ_M is the Michel rho parameter.

When internal radiative corrections are included the shape of the spectrum is presented as

$$R_2^+\ (X) = \left[\frac{1 + h\ (X)}{1 + \Lambda_1 + (2/3)\rho_M(\Lambda_2 - \Lambda_1)}\right] R_1^+(X) \tag{19}$$

The constants Λ_1, Λ_2 and the energy dependent term h(X) are defined in Appendix A. The expression $R_1^+(X)$ and $R_2^+(X)$ are normalized to 1. The expression, $R_2^+(X)$, is the theoretical starting point. Energy losses and resolution effects must be folded into $R_2^+(X)$ before comparison can be made with the experimental results. $R_1^+(X)$ and $R_2^+(X)$ are shown in Figure 7, labeled R_1^+ and R_2^+ respectively.

2. Bound Decay Spectrum

The negative muon decay spectrum in copper was obtained by interpolation from the iron, antimony, and lead tabular results of Huff using vector coupling. The iron, antimony, and lead curves as

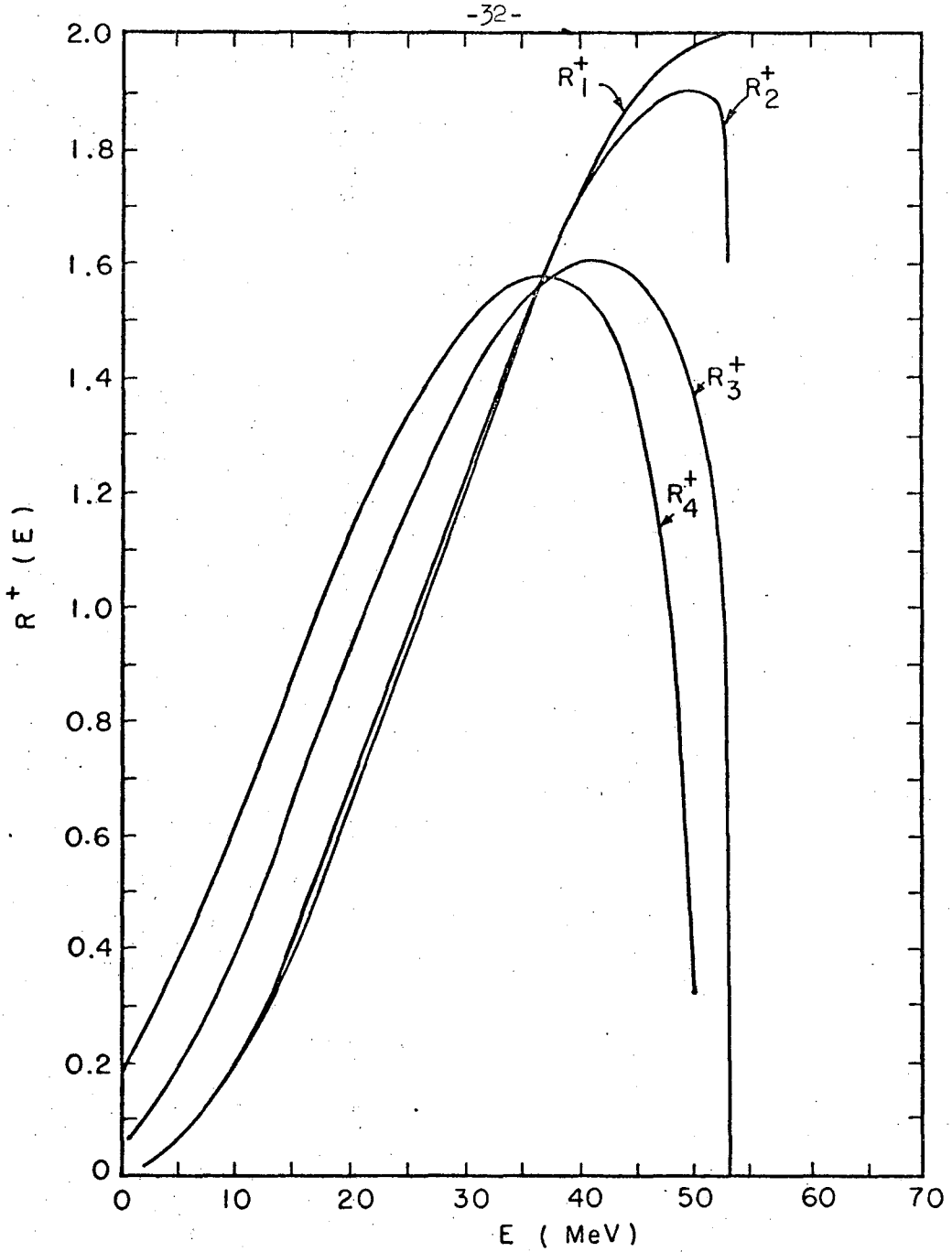

MUB-13151

Fig. 7. Positive spectrum curves. Curve R_1^+ represents the elementary spectrum for unpolarized positive muon decay. The curve R_2^+ represents the spectrum when internal radiative corrections are included. Curve R_3^+ represents the spectra when bremsstrahlung is included. Finally curve R_4^+ shows the spectrum after both bremsstrahlung and ionization losses are included.

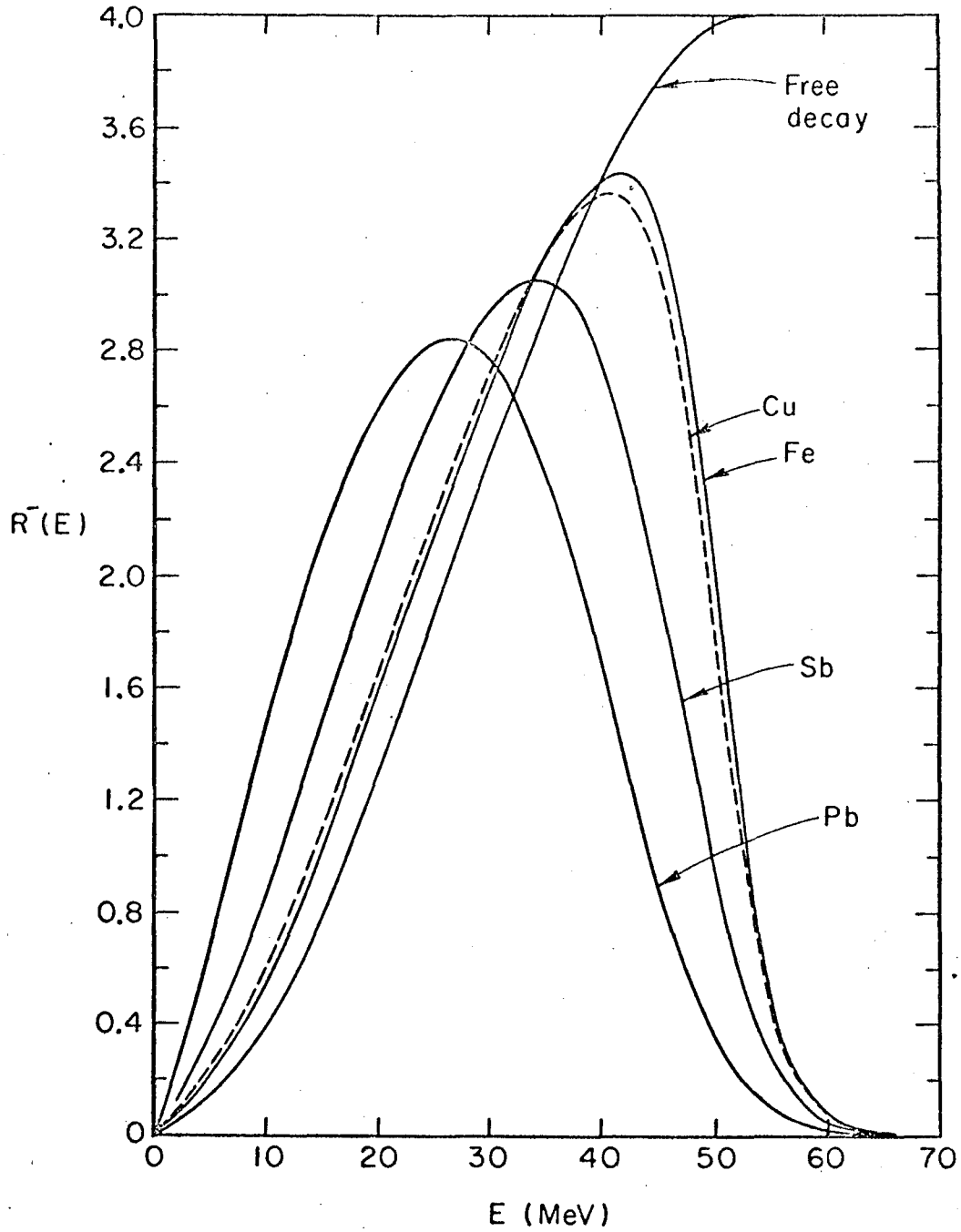

MU-36682

Fig. 8. The negative bound decay spectra in iron, antimony, and lead. The dotted curve represents the interpolated copper spectrum. For comparison the free decay spectrum is also shown.

well as the interpolated copper curve are presented in Figure 8. For comparison the free decay spectrum is also shown.

B. Multiple Scattering Effect on Electron Path Length

In computing the energy losses which an electron undergoes upon passing through matter, account must be taken of the multiple scattering effect on the electron path length. This effect has been studied by W. T. Scott[48] and C. N. Yang.[49] The effect of the multiple scattering is to effectively increase the straight line path length. The actual path length, l, is given by

$$l = t(1 + t/(\lambda\rho)) \qquad (1)$$

where

t = straight line path length in gms/cms^2

ρ = density in gms/cms^3

and λ is the characteristic length (cms) describing the amount of scattering. λ is given by

$$1/\lambda = \frac{2\pi e^4 Z^2 N}{p^2 v^2} \rho \ \ell n \ (150 \ pc/mc^2 Z^{1/3}), \ cm^{-1} \qquad (2)$$

Each material thickness through which the electron passes is increased by the above formulae in computing the bremsstrahlung and ionization energy losses.

For copper, where the effect is largest, multiple scattering increases the effective path length for 20 MeV electrons by $\sim$ 17%. At the upper end of the spectrum near 60 MeV the increase falls off to $\sim$ 2%.

C. Bremsstrahlung

The main cause of energy loss straggling in the energy range, 20 to 60 MeV, is due to photon emission by the electrons in passing through matter. In order to determine the effect of this bremsstrahlung on the shape of the initial electron spectrum one has to consider the solution of the basic transport equation,

$$\frac{\partial[n(E,t)dE]}{\partial t} = \int_{E}^{E_o} \Phi(E',E)dE\ n(E',t)dE' - \int_{0}^{E} \Phi(E,E')dE'\ n(E,t)dE \qquad (1)$$

Basically one seeks to find the change in the number of electrons in the energy interval E to E + dE when the entire electron distribution moves from a depth t to a depth t + dt, where dt represents an infinitesimal change in thickness. The first integral on the right in eq. (1) represents the contribution from higher energy electrons falling into the energy interval E to E + dE. $\Phi(E',E)dE$ represents the probability that an electron of energy $E' > E$ will lose energy by bremsstrahlung such that its final energy lies in the energy interval E to E + dE. $n(E',t)dE'$ represents the number of electrons at a depth t with energies lying in the interval E' to E' + dE'.

The second integral on the right side of eq. (1) represents the decrease in the number of electrons in the energy interval E to E + dE when passing through a thickness, dt, to all lower energies $E' < E$.

Through the application of Laplace transformations the following solution of eq. (1) was obtained, (see Appendix B for details of the derivation):

$$n(E,t) = \int_E^{E_o} \left\{ \frac{dE'}{E'} n(E',0) \frac{\ln \frac{E'}{E}^{a_o t-1}}{\Gamma(a_o t)} [1-t \int_0^{E'} \frac{dE''}{E'} \left[\Phi_{L.W}(E',E'') + \frac{a_o}{\ln \frac{E}{E'}}](\ln \frac{E'}{E})^{a_o t} \right] \right\} + t \int_E^{E_o} \left\{ \frac{dE'}{E'} n(E',0)(\ln \frac{E'}{E})^{a_o t} \left[\Phi_{L.W}(E',E) + \frac{a_o}{\ln \frac{E}{E'}} \right] \right\} \quad (2)$$

In order to evaluate the expression on the right side account must be taken of the singularity in the bremsstrahlung cross section for zero energy losses. This is done by breaking the integral whose limits are E to E_o into two integrals thusly,

$$n(E,t) = \int_E^{E+\Delta} I_1 + \int_{E+\Delta}^{E_o} I_1 + t \left[\int_E^{E+\Delta} I_2 + \int_{E+\Delta}^{E_o} I_2 \right] \quad (3)$$

where

$$I_1 = \left\{ \frac{dE'}{E'} n(E',0) \frac{(\ln \frac{E'}{E})^{a_o t-1}}{\Gamma(a_o t)} \left[1-t \int_0^{E'} \frac{dE''}{E'} [\Phi_{LW}(E',E'') + \frac{a_o}{\ln(\frac{E}{E'})}](\ln \frac{E'}{E})^{a_o t} \right] \right\} \quad (4)$$

and

$$I_2 = \left\{ \frac{dE'}{E'} n(E',0)(\ln \frac{E'}{E})^{a_o t} \left[\Phi_{L.W}(E',E) + \frac{a_o}{\ln \frac{E}{E'}} \right] \right\} \quad (5)$$

Equation (3) is finally averaged over the copper target and summed over the remaining materials such as polystyrene, aluminum, and air through which the electrons pass before reaching the focal plane

counters.

$n(E',0)$ = electron energy distribution before energy losses occur.

t = material thickness in gms/cm^2

$a_o = (\frac{4}{3}) \frac{1}{L_R}$ where L_R is the radiation length in gms/cm^2.

Γ = gamma function

Δ = 0.1 MeV represents the width of the singularity region

$\Phi_{L.W}(E',E)$ = Lamb-Wheeler expression for the probability per unit distance that an electron of initial energy E will radiate a photon of energy k such that its final energy will be $E' = E-k$. (See Appendix B). The Lamb-Wheeler expression includes the effect of the atomic electrons as well as the effect of the nucleus upon the radiative probability.[50]

The final solution of eq. (3) is labeled by the symbol $R_3^{\pm}(E_f)$. $R_3^{+}(E_f)$ is the curve for positrons and is labeled R_3^{+} in Figure 7. $R_3^{-}(E_f)$ is similarly the curve for electrons and is labeled R_3^{-} in Figure 9.

D. Ionization Straggling

The decay electrons not only lose energy by bremsstrahlung but also by ionization. Because of the statistical nature of the collision losses account must be taken of the straggling in energy losses.[51,52] It should be noted, however, that a completely correct treatment of the effect on the spectrum of the energy losses would include both bremsstrahlung and ionization losses together in the basic transport equation. Unfortunately, due to the mathematical complexity of this problem, a complete solution has never been

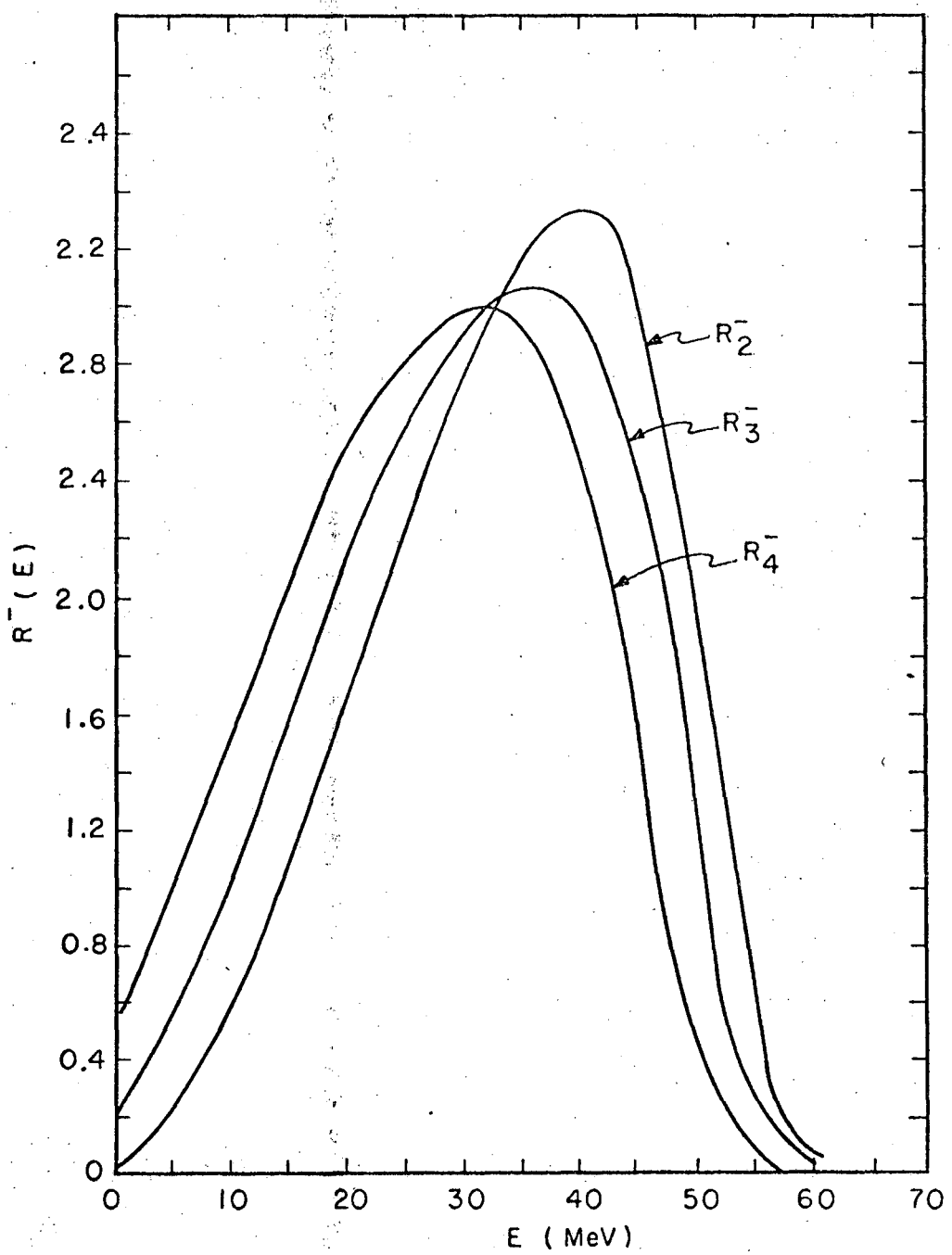

MUB 13150

Fig. 9. Negative spectrum curves. Curve R_2^- represents the initial copper spectrum before any energy corrections have been made. Curve R_3^- represents the spectrum after bremsstrahlung losses have occurred. Curve R_4^- represents the final spectrum after both bremsstrahlung and ionization losses have occurred.

achieved.

In practice one assumes that first one energy loss process occurs, followed in turn by the second energy loss process. Now provided that the thicknesses of materials through which the electrons pass are sufficiently small, it should not matter in which sequence the energy losses occur. In averaging over the entire one-eighth inch copper target it was found that reversing the energy loss sequence resulted in, at most, a 2% difference. This difference could in principle, be reduced by mathematically subdividing the target and then propagating the distribution from each subslice out to the surface and finally averaging over all the distributions. However, since this procedure was not done, an error of $\sim 2\%$ is presumed to exist in the result of the energy loss calculations. The sequence followed in the calculations presented here is that first bremsstrahlung occurs, followed by ionization losses.

Consequently, if $R_3^{\pm}(E_i)$ is the spectrum after losses by bremsstrahlung, then

$$R_4^{\pm}(E_f) = \sum_{E_i > E_f} R_3^{\pm}(E_i) \cdot L^{\pm}(E_i, E_f) \cdot \Delta E_i$$

where $R_4^{\pm}(E_f)$ is the value of the spectrum at the energy E_f, after both bremsstrahlung and ionization have occurred. $L^{\pm}(E_i, E_f)$ is the probability that electrons whose initial energies lie in the interval ΔE_i centered at E_i will loose energy by ionization such that their final energy is E_f. For details of the straggling calculations see Appendix C.

It should be noted that the straggling effect due to ionization losses was much less significant than the bremsstrahlung in terms of changing the shape of the input distribution in the energy range 20 to 60 MeV. The main effect of the ionization losses appeared to be a shift of the input spectrum toward lower energy by the average ionization loss, ΔE_{AVE}, equal to $\sim$ 4.2 MeV.

The curve labeled R_3^+ in Figure 7 represents the spectrum after bremsstrahlung alone has occurred, while R_4^+, in the same figure, represents the spectrum after both bremsstrahlung and ionization straggling have occurred. In Figure 9 the corresponding curves for the negative spectrum are labeled R_3^- and R_4^-, respectively. In Figure 9 the curve R_2^- represents the unsmeared theoretical copper spectrum, uncorrected for any internal radiative processes (R_2^- is identical with the copper curve in Figure 8).

E. Solid Angle Effect on the Spectrum

$R_4^{\pm}(E_f)$ is the momentum spectrum after corrections for energy losses have been made. Before a comparison can be made between theory and experiment, account must be taken of the individual focal plane counter dependence on solid angle, $\Omega_i(pc)$, as a function of momentum. Using the computed results from the OMEGAH program (see Figure 10) the $\Omega_i(pc)$ were folded into the energy smeared spectra $R_4^{\pm}(E_f)$.

Then,

$$N^{i,\pm}_{THEOR.} = \sum_{E_f} R_4^{\pm}(E_f) \cdot \Omega_i(E_f) \cdot \Delta E_f \quad i = 1, \ldots . 11.$$

where $N^{i,\pm}_{THEOR.}$ is the theoretically predicted number (unnormalized) of

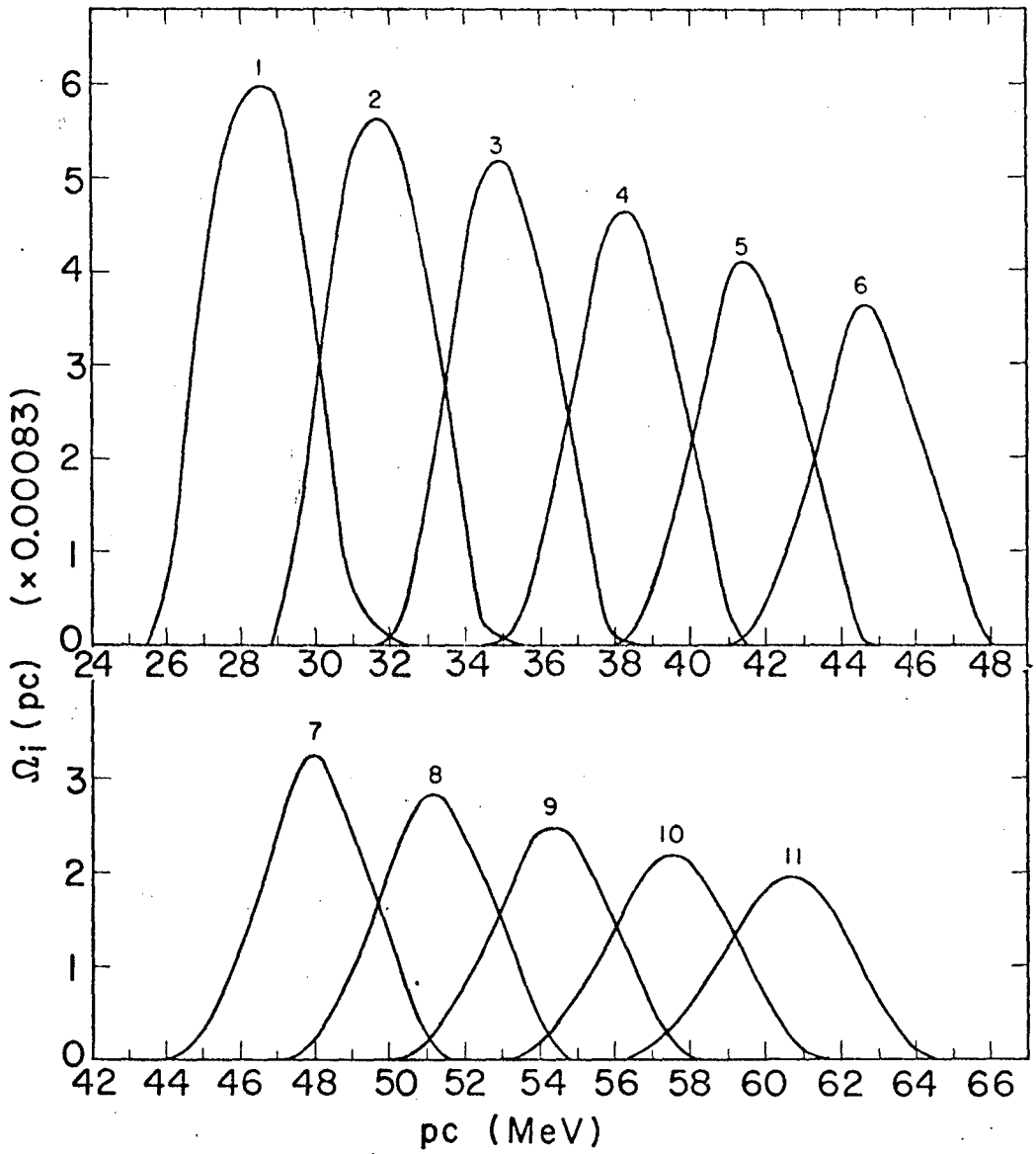

Fig. 10. Solid angle dependency on momentum for the front row focal plane counters. Note that the momentum scale corresponds to a central field value of 2730 gauss. In calculations the momentum is linearly scaled down to correspond to the lower fields present during the data taking runs.

expected decay events occurring in the ith counter. (See Appendix F for details of the OMEGAH program, which computes the $\Omega_i(pc)$).

F. Counter Solid Angle Calculation

A particle orbit tracking program called OMEGAH was written utilizing the results of the magnetic field measurements. (See Appendix F for details of the OMEGAH program.) At a point located within the copper target a unit sphere was constructed whose surface was subdivided in elements each equal to 2.5×10^{-5} of the total surface area. Orbits from the source point and through the centers of each surface element were tracked through the spectrometer and onto the focal plane. The orbit calculations were made over the entire range of acceptable momenta in one-half MeV/c increments. Finally the results were summed over the entire volume of the copper target. The numbers of orbits striking each of the eleven front row focal plane counters (weighted by the factor 8.3×10^{-7}) were recorded as a function of momentum. (See Figure 10).

The total fractional solid angle of the spectrometer as a function of momentum is shown in Figure 11.

The magnetic field measurements were taken when the central field values were 2730 gauss on the average. The data runs were taken under two different central field settings, one at 2300 gauss and the other at 2400 gauss. In subsequent calculations the mean momentum $\overline{pc}_i$ is linearly scaled down to correspond to the lower magnetic field conditions. Because of the low fields involved no errors due to any pole tip saturation effects are expected in this scaling down procedure.

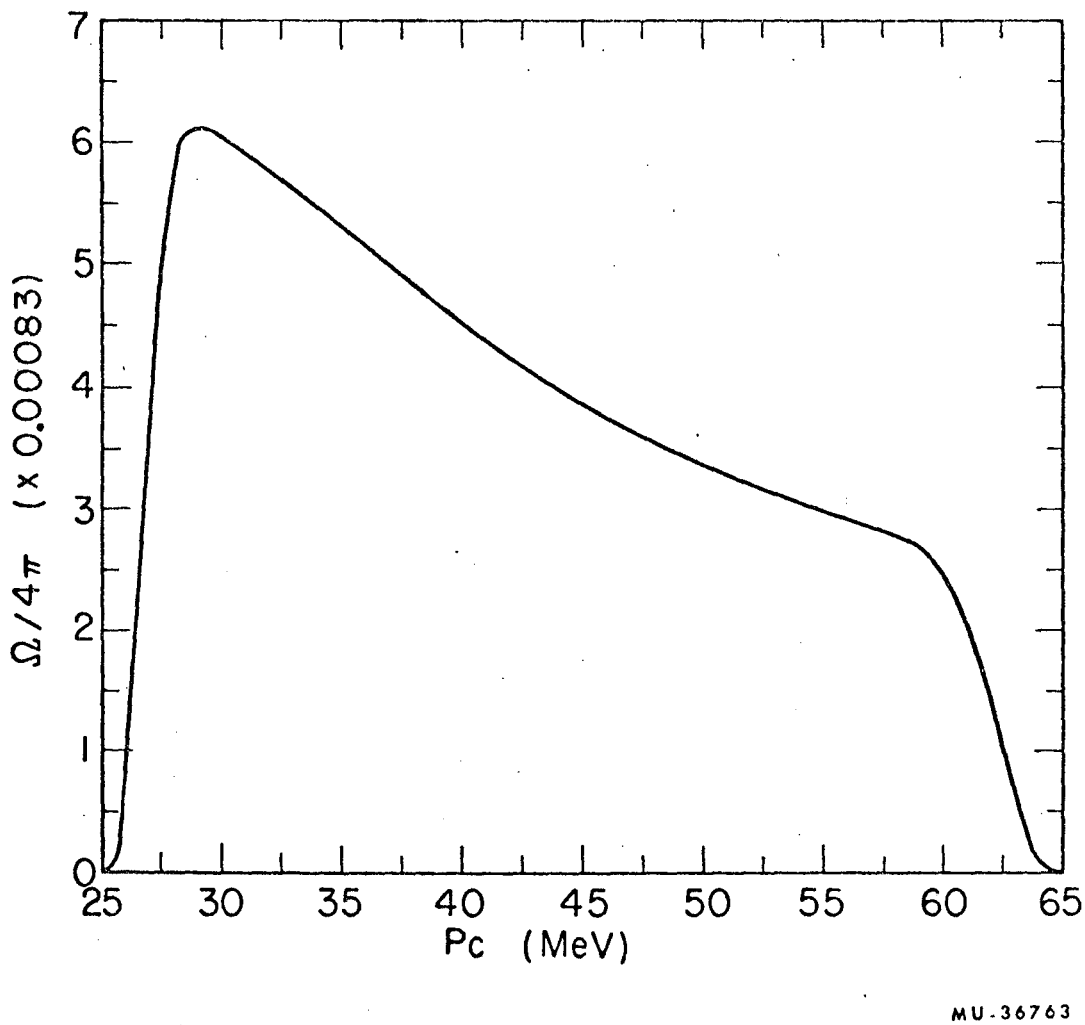

Fig. 11. Total fractional solid angle of the spectrometer as a function of momentum.

Electron scattering from the spectrometer pole tips introduces a high momentum tail to each of the $\Omega_i(pc)$. This modification is discussed in section G.

The results of the OMEGAH program were checked independently by another technique of generating orbits through the spectrometer. This alternate method used the raw magnetic field measurements directly rather than mathematical fits to the raw data in the various regions. Using the local values of the magnetic field, the differential equation of motion of a charged particle in a magnetic field was transformed into a system of six first order differential equations. This system of first order differential equations was then numerically integrated using a fourth-order Adams Moulton Predictor-corrector method.[53] Several thousand individual orbits were generated by both techniques. A comparison of orbits with the same initial conditions generated by the alternate methods showed that the orbits crossed the focal plane usually within a 1/4" of one another. The displacement in the direction parallel to the median plane was invariably negligible compared to the direction normal to the median plane. This effect is, of course, directly related to the fact that off-median plane magnetic measurements existed only at a distance 2-1/4" and 3-1/4" from the median plane, whereas within each plane the axial field values were measured in 1" steps in both directions. Adding up all the orbits falling within 1/4" of the top and bottom edges of the focal plane counters it was determined that these orbits constituted $\sim 7\%$ of the total number striking the entire focal plane. As a measure of the uncertainty in the solid angle calculation we shall say that 10% of these edge

orbits may, in fact be in error. Consequently they constitute a gross overall error of 0.10 x 0.07 = 0.007, or $\sim$ 1.0% in the solid angle computed results.

G. Resolution Function

To illustrate the smearing effect of the energy losses and the spectrometer resolution on the energy distribution of the decay electrons the following calculation was carried out. A "delta" function, approximated by a 0.2 MeV wide, 264.3 MeV tall rectangle, was chosen as the theoretical input spectrum. These dimensions normalized the area to the maximum electron energy, 52.83 MeV. The distribution was arbitrarily centered at 44.1 MeV and subsequently smeared by bremsstrahlung and ionization losses and finally by the spectrometer resolution. The results are presented in Figure 12. The F. W. H. M. spread for 44.1 MeV electrons is shown to be approximately 12-1/2%. The contributions to the spread from energy losses and the spectrometer resolution are roughly comparable.

H. Electron Scattering from Spectrometer Pole Tips

Since the solid angle presented by the spectrometer pole tips is comparable in magnitude to that of the focal plane counters an estimate must be made of the probability that an incident electron or positron scatter from the pole tips and still manages to reach one of the focal plane counters.

The initial conditions of direction and momentum at the pole tip surface are given by the main orbit tracking program OMEGAH. Inside the iron the electron is tracked in fixed (0.0125 radiation

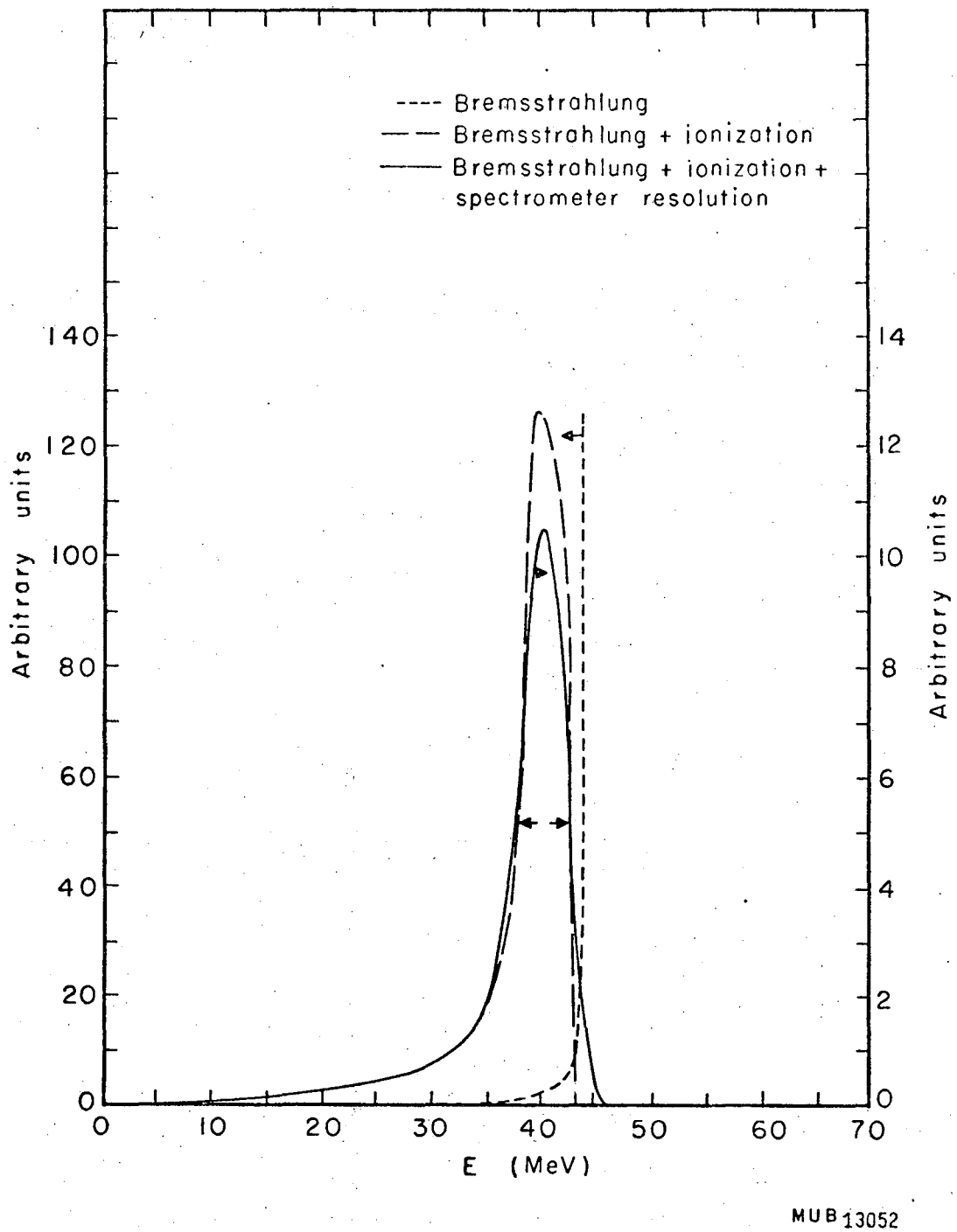

Fig. 12. Delta function resolution.

lengths) step increments. The new direction in space relative to the direction of the previous step is specified by the polar and azimuthal scattering angles. These angles are generated by means of the Monte Carlo technique. The polar angle is selected from a gaussian distribution representing the multiple scattering process with an r.m.s. scattering angle given by

$$< \theta^2 >^{1/2} = (21/pc)\cdot(L/L_R)^{1/2} \text{ radians}$$

where $L/L_R = 0.0125$. L_R is the radiation length in iron and L the step size. pc is the momentum in MeV units. The azimuthal angle is selected from a uniform distribution between 0 and 2π radians. Plural and large angle single scatters are considered to occur infrequently compared to the multiple scattering process and hence are ignored. The lateral displacement of the electron in traversing each step of iron is also neglected.

The energy lost by the electron in each step was subtracted from its energy at the beginning of the step. The amount of energy lost was obtained from the tables of electron energy losses by Berger and Seltzer.[54] These energy losses included both radiative and ionization losses. The error in $(dE/dX)_{ION.}$ does not exceed 2% while $(dE/dX)_{RAD.}$ is accurate to within 5% between 2 and 15 MeV and to within 3% above 15 MeV. The energy loss is very closely the same for both electrons and positrons. When the energy of the electron fell below 10 MeV it was presumed lost and the tracking ceased. At the end of each step the new spatial coordinates were tested to see if the electron had re-entered the magnet gap. If the electron did re-enter the gap

control of its tracking was returned to the main orbit tracking control of the OMEGAH program.

Several processes were neglected in this pole tip scattering calculation. Photons from bremsstrahlung which could conceivably pair produce were considered to be of negligible importance. Positron annihilation was likewise considered to be of negligible importance, (see Section H). Bhabha (e^+e^-) and Møller (e^-e^-) scattering from the atomic electrons were also ignored. The effect of ignoring these processes is unlikely to be larger than the uncertainties (a few per cent) inherent in using the Monte Carlo technique to generate the polar and azimuthal scattering angles from multiple scattering. This may be seen by a comparison of the Møller, Bhabha, and bremsstrahlung cross sections. Rossi[55] gives these cross sections as

$$\Phi^{M}_{COL}(E,E') = 2Cm_eC^2\left\{\frac{E^2}{(E-E')^2}\frac{1}{(E')^2}\left[1-\frac{E'}{E}+\left(\frac{E'}{E}\right)^2\right]^2\right\}, \quad \text{- Møller}$$

$$\Phi^{B}_{COL}(E,E') = 2Cm_eC^2\left\{\frac{1}{(E')^2}\left[1-\frac{E'}{E}+\left(\frac{E'}{E}\right)^2\right]^2\right\}, \quad \text{Bhabha}$$

where

$$C = \pi N_A \frac{Z}{A} r_e^2 = 0.150 \frac{Z}{A} g^{-1}cm^2$$

$E \gg m_eC^2$ or $\beta \simeq 1$

E = initial electron energy

E' = energy transferred or lost.

The bremsstrahlung cross section is given by Rossi[55] as

$$\Phi_{RAD}(E,E') = 4 \frac{N_A}{A} Z^2 r_e^2 \frac{1}{E'} F(U,v) \quad \text{(ignores influence of atomic electrons)}$$

where

$$\alpha = e^2/\hbar c = 1/137.027$$

$$U = E + m_e c^2$$

$$v = E'/U$$

F(U,v) is a slowly varying function of U and v. Note that the above formula considers only the nuclear effect on the bremsstrahlung. For the purpose of simplicity the smaller effect of the atomic electrons, treated by Wheeler and Lamb,[50] is ignored here. The cross sections are presented in Figures 13-15. Only the bremsstrahlung curves for no screening ($\gamma \gg 1$) and complete screening ($\gamma \approx 0$) are shown. It should be understood that the intermediate cases of bremsstrahlung lie between the two extremes. The Møller and Bhabha cross sections are comparable to the bremsstrahlung only when E' is small. However, it is precisely when E' becomes small that the Bhabha and Møller cross sections approach one another. Consequently, ignoring both Møller and Bhabha cross sections should not introduce any significant energy bias into the spectra.

The principle effect of pole tip scattering (see graphs 16 and 17) is to provide a high momentum tail to the probability distribution for any focal plane counter to detect an electron of given momentum emerging from the target.

I. Pair Annihilation

One of the energy dependent effects which affects the positive

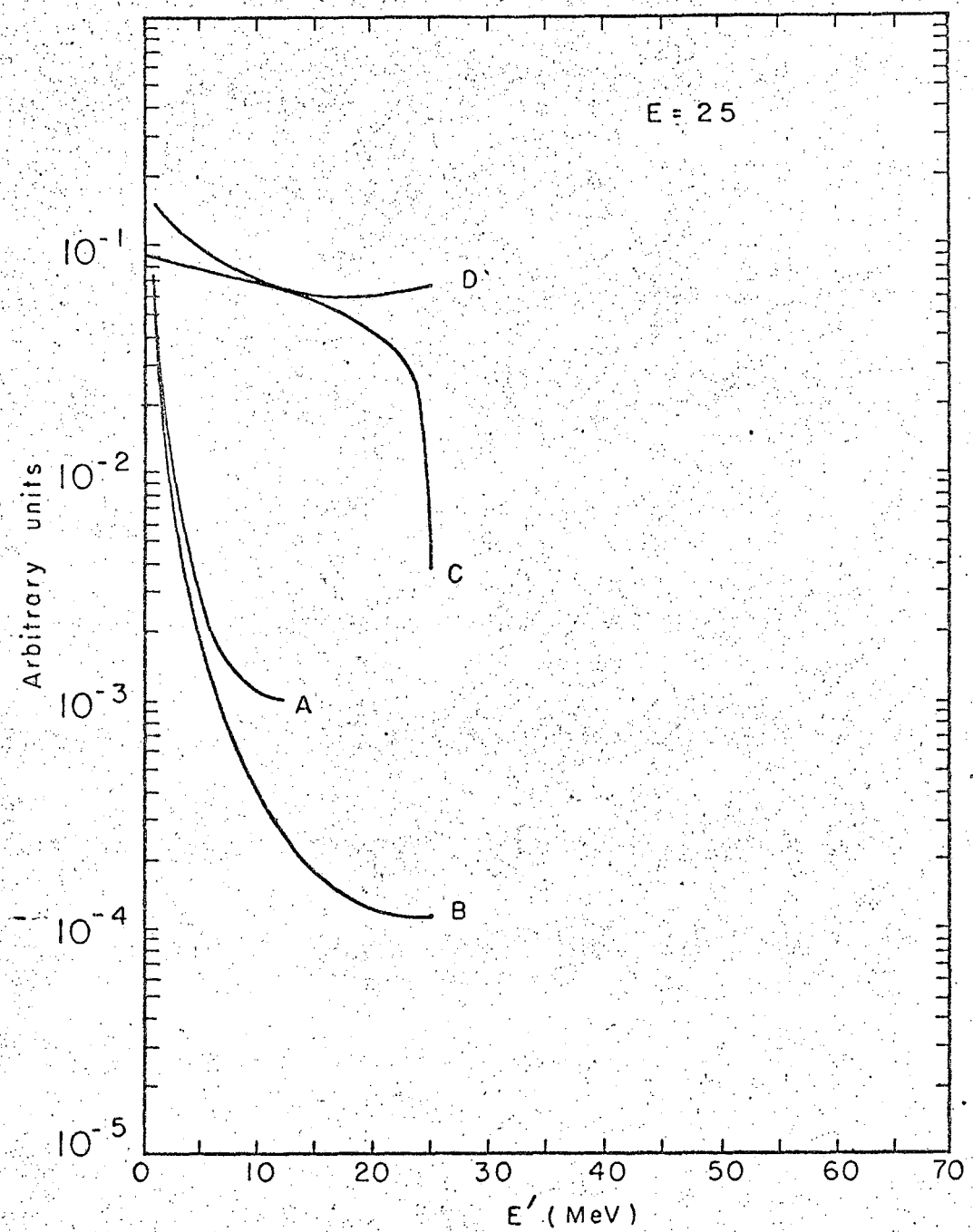

MUB 13153

Fig. 13. Comparison of Møller, Bhabha, and bremsstrahlung cross-sections (E = 25 MeV). (A = Møller, B = Bhabha, C = No screening, D = complete screening.) E = initial energy, E' = final energy.

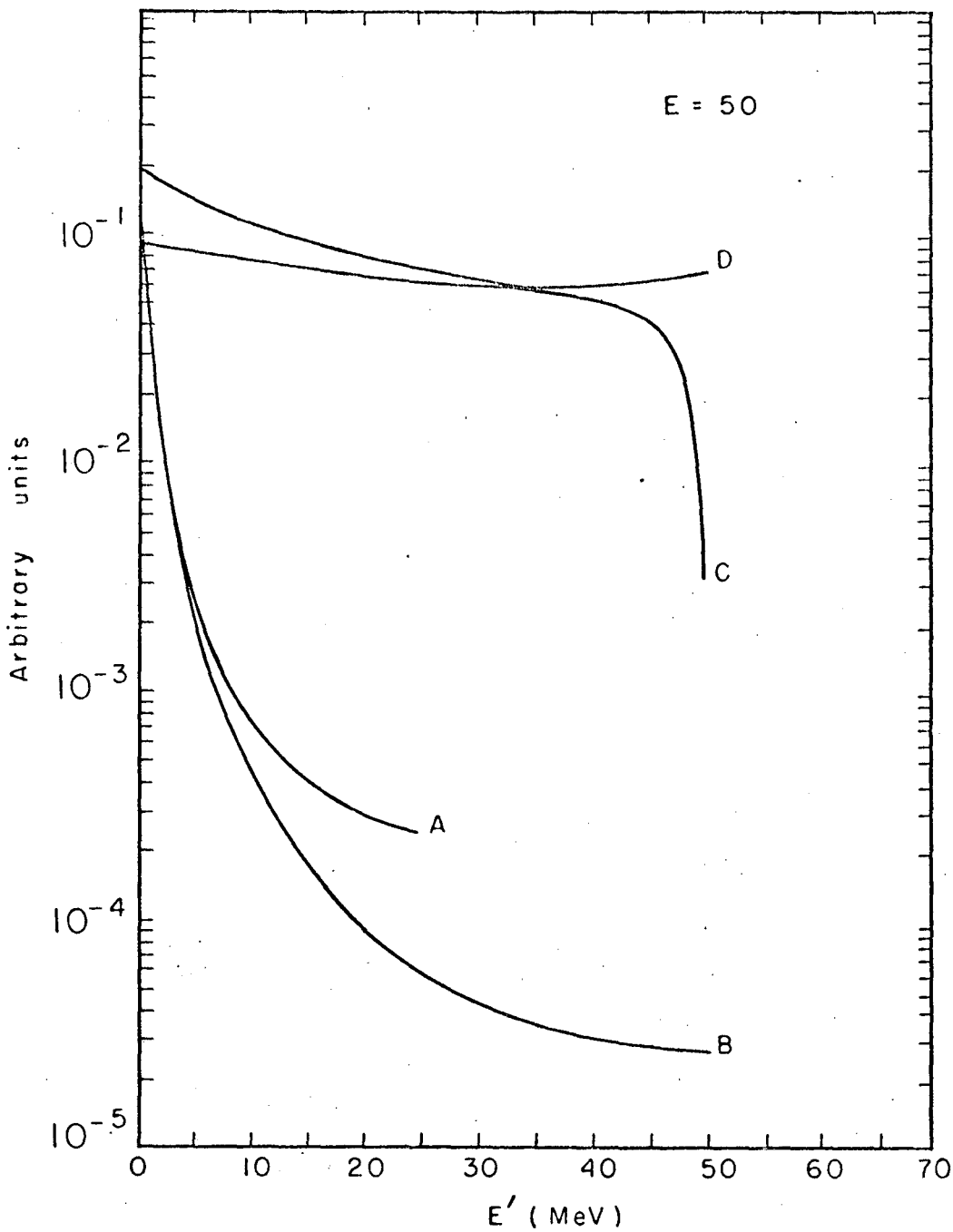

MUB 13152

Fig. 14. Comparison of Møller, Bhabha, and bremsstrahlung cross-sections (E = 50 MeV). (A = Møller, B = Bhabha, C = No screening, D = complete screening.) E = initial energy, E' = final energy.

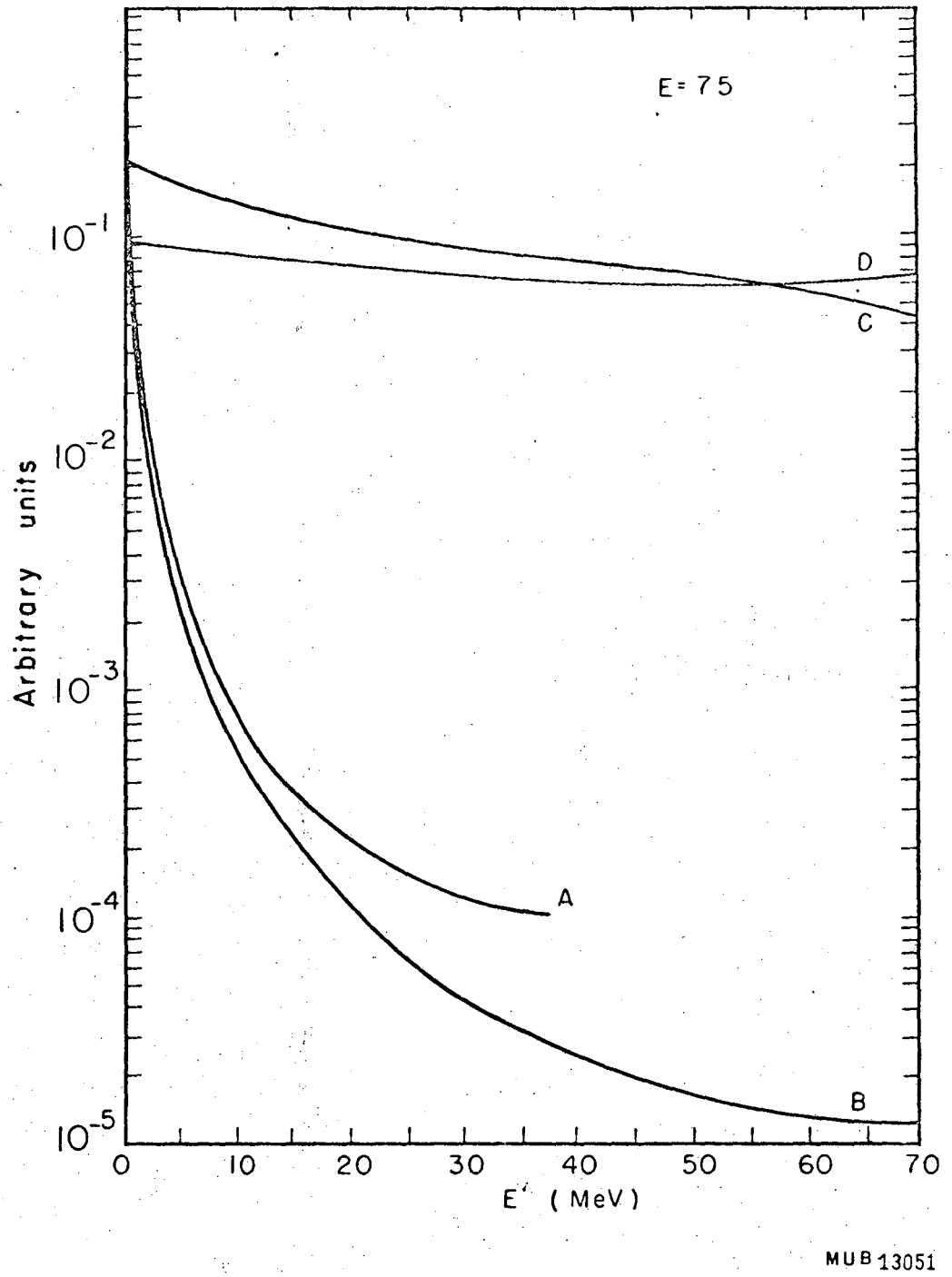

Fig. 15. Comparison of Møller, Bhabha, and bremsstrahlung cross-sections (E = 75 MeV). (A = Møller, B = Bhabha, C = No screening, D = complete screening.) E = initial energy, E' = final energy.

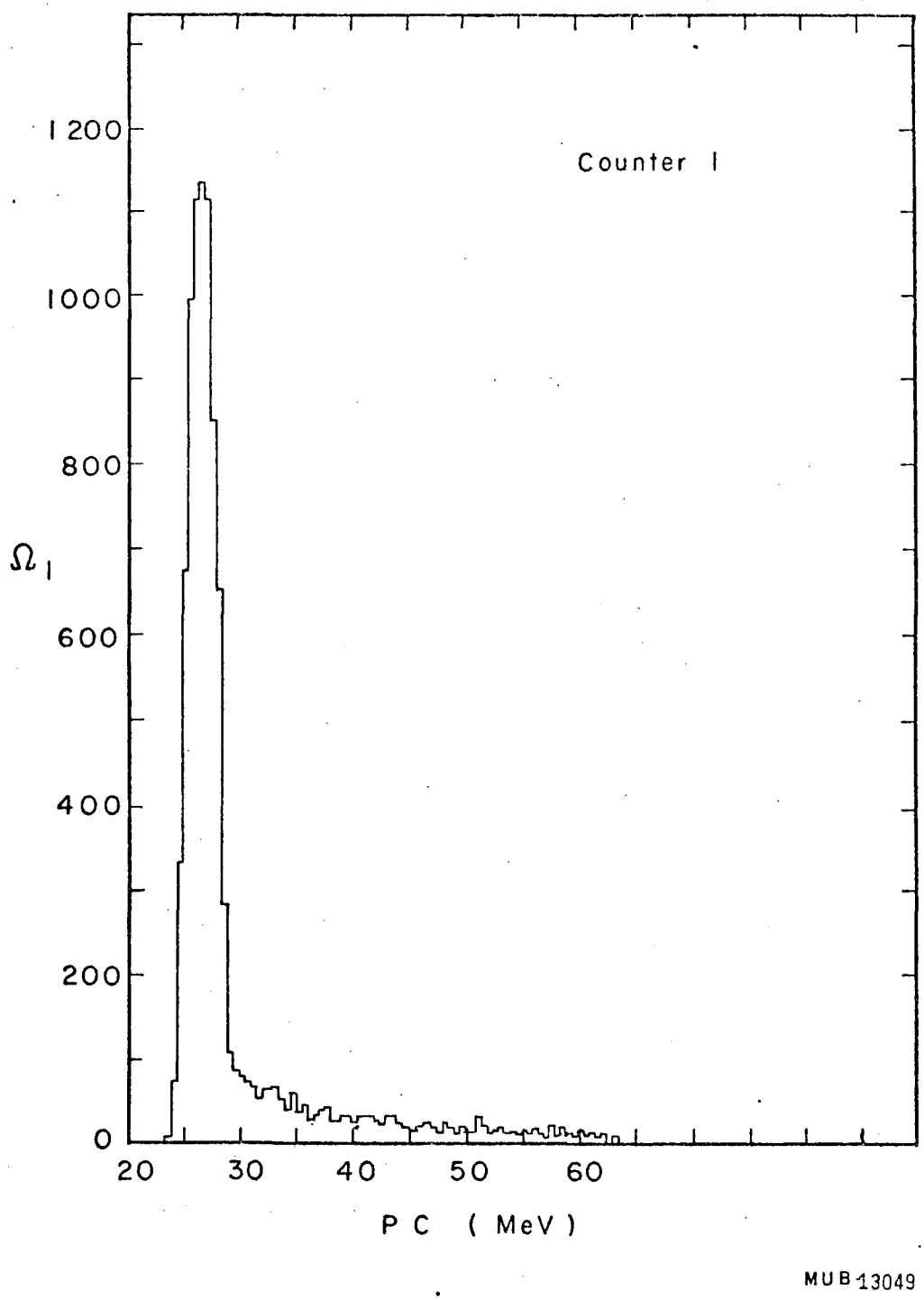

Fig. 16. Effect of pole tip scattering on solid angle as seen by focal plane counter 1.

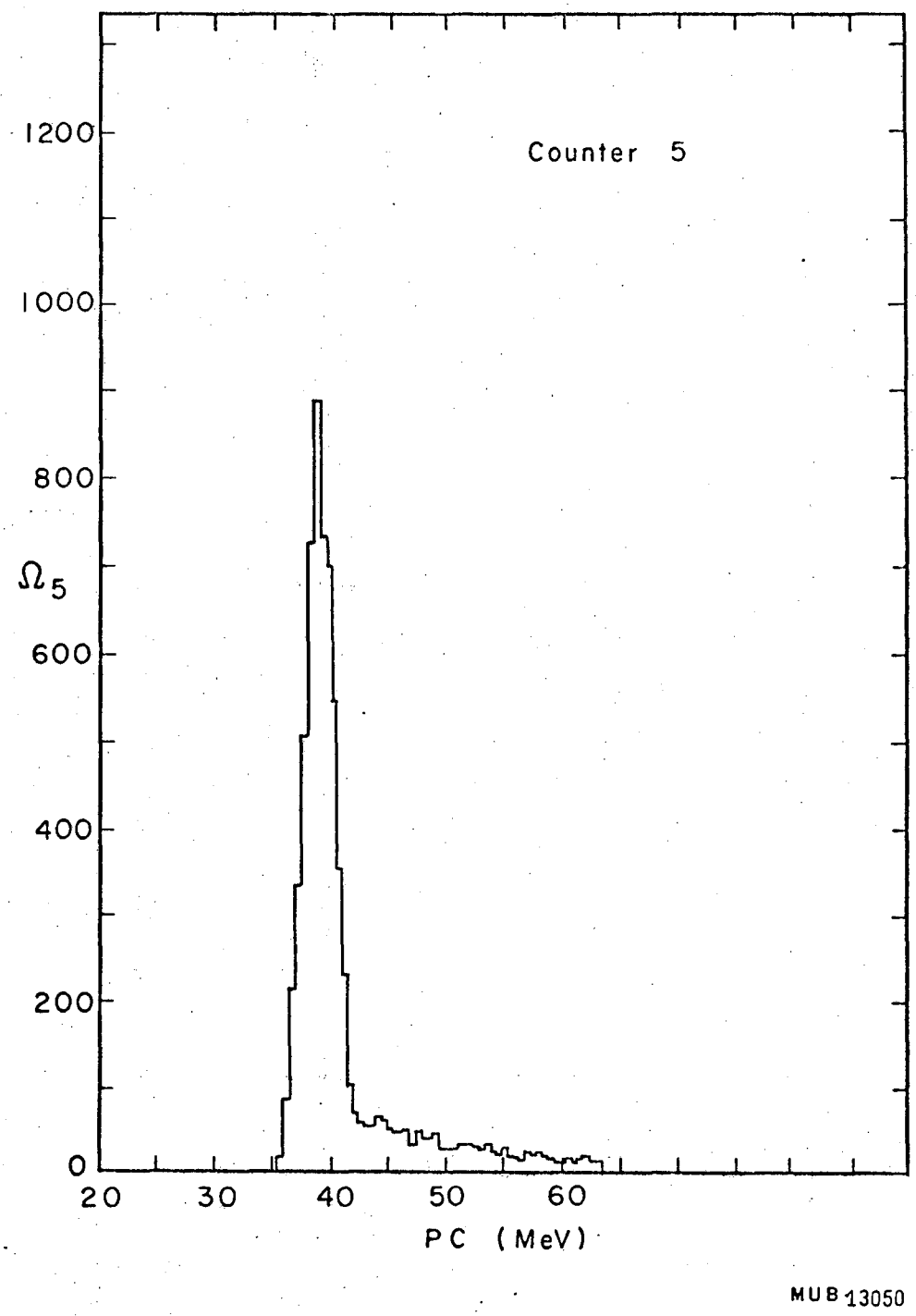

Fig. 17. Effect of pole tip scattering on solid angle as seen by focal plane counter 5.

decay spectrum but not the negative is pair annihilation. First, derived by Dirac,[56] the formula for the cross section of annihilation of a positron of energy E_+' with an electron at rest is given by

$$\phi(E_+') = \pi r_o^2 \frac{1}{\gamma+1} \left[\frac{\gamma^2 + 4\gamma + 1}{\gamma^2-1} \ln \{\gamma + \sqrt{(\gamma^2-1)}\} - \frac{\gamma+3}{\sqrt{(\gamma^2+1)}}\right]$$

where

$$\gamma = E_+'/m_e C^2$$

$$r_o = e^2/m_e C^2 = 2.818 \times 10^{-13} \text{ cms.}$$

The "differential annihilation probability" per energy interval dE' is given by Heitler[57] as,

$$w(E') = \frac{N\ Z\ \phi(E_+')}{-dE'/dx}$$

where

N = number of atoms/cm^3 ($= 8.46 \times 10^{22}$ for Cu)

For a 20 MeV positron there is only a 0.2% probability of annihilation in copper (as well as for iron). Since the cross-section decreases for higher energies, it is safe to ignore the effect of pair annihilation over the energy range measured in this experiment.

J. Effect of Multiple Scattering on the Solid Angle Calculation

An estimate of the effect of including multiple scattering in the entering electron telescope showed that $\sim 4\%$ fewer orbits would reach the focal plane. However, a study of the difference in the relative numbers of orbits reaching the eleven focal plane counters, i.e., with and without multiple scattering, showed no significant dependence on momentum. Consequently, the effect of multiple scattering on the solid angle calculation was ignored.

K. Background Subtraction

The principle source of background comes from the scintillation counter immediately in front of the copper target. This background will be unchanged whenever the copper target is removed for a target out run.

A possible secondary source of background is the anti-coincidence counter $\overline{\mu}_4$ located 5" downstream from the copper target. From the measured efficiency of $\overline{\mu}_4(\sim 90\%)$ and the fraction of the counter which can "see" the entering electron telescope, it is estimated that as much as $\sim 10\%$ of the background may come from $\overline{\mu}_4$. Any detectable background originating in $\overline{\mu}_4$ must pass through the copper target location. If the target is in position, the electrons will lose energy in passing through it, whereas they will not if the copper is removed. Consequently there is a possible small component of the background that depends on whether or not the copper target is in place. A crude estimate of this effect indicates that the principle change would be an increase of 3 - 6% in the experimental points in counters 10 and 11, with much smaller changes in the remaining counters. This would be in the direction of

providing slightly better agreement with the theoretically predicted values. Since counters 10 and 11 contain only a relatively small fraction of the total data and because of their very poor signal to noise ratio it was decided to exclude the data of these two counters and to ignore the much smaller effect on the remaining counters.

IV. DATA ANALYSIS

A. Procedure

The raw data is presented in Tables I, II, and III. The order in which the data runs were presented is chronological. Data runs with the same run number identification were taken on different days. Table I represents data runs taken when the central field in the magnetic spectrometer was 2400 gauss. Tables II and III represent data runs for which the field was reduced to 2300 gauss. Usually each sequence of data runs was started with the taking of one or more positive runs. The higher decay rate for positive decay events allowed a rapid check of the incident beam conditions and of the associated decay rates obtained by the focal plane counters.

The most straight forward comparison between theory and experiment can be made by application of the chi-square test whereby the numbers of decay events experimentally counted in each of the eleven focal plane counters is compared with the number predicted by theory.

In both the positive and negative theoretical spectra the Michel rho parameter, ρ_m, is given the value of 0.75 predicted by the V-A theory and very well confirmed experimentally by Sachs, et al.[43] for the positive spectrum and by Block, et al.[35] for the negative. It should again be stressed that the internal radiative corrections have never been calculated for the negative spectrum and are consequently not included in the negative spectrum predictions. One knows, however, that in the case of the positive spectrum, neglecting the effect of the internal radiative corrections would lead to a 5.6% lower prediction, i.e. 0.706 for ρ_m, rather than 0.75. Provided one can ignore

Table I. Raw data from eleven focal-plane counters.

Run	$W_1(\times 10^8)$	Counter 1	2	3	4	5	6	7	8	9	10	11
Target in; μ^-												
6	4.00	29	25	24	18	10	14	8	10	4	1	1
9	4.00	47	21	22	18	22	10	11	11	6	1	1
12	4.00	23	30	26	25	14	12	20	13	4	1	1
14	4.00	24	22	26	21	13	26	10	13	4	1	0
15	4.00	32	21	21	18	23	14	7	5	0	0	0
17	4.00	28	26	30	19	15	12	4	7	4	1	0
19	4.00	28	24	32	13	23	8	12	9	4	1	0
21	4.00	22	23	22	14	15	20	12	1	4	2	0
23	4.00	21	34	19	19	16	11	16	11	4	2	1
25	4.00	24	22	23	18	12	13	10	12	3	2	0
	$\Sigma = 40.00$	278	248	245	183	163	140	110	92	37	12	4
Target out; μ^-												
7	2.00	0	1	1	2	5	6	4	2	1	5	2
8	1.25	4	1	1	0	2	2	0	2	0	1	0
10	2.00	4	6	4	2	2	2	1	2	2	0	0
13	2.00	4	3	4	3	6	4	3	5	1	0	1
14	2.00	5	4	2	4	6	2	0	4	2	0	0
16	2.00	4	4	3	5	2	5	0	3	1	1	0
18	2.00	1	4	3	2	2	1	2	5	1	0	1
20	2.00	4	1	3	3	2	3	3	8	0	0	0
22	2.00	6	5	3	4	2	2	2	1	2	1	0
24	2.00	6	2	2	3	4	3	5	0	3	0	1
	$\Sigma = 19.25$	38	31	26	28	33	30	20	32	13	8	5
Target in; μ^+												
3	2.00	835	830	769	709	543	574	451	391	227	40	6
5	4.00	1769	1718	1531	1450	1300	1064	967	818	443	83	8
	$\Sigma = 6.00$	2604	2548	2300	2159	1843	1638	1418	1209	670	123	14
Target out; μ^+												
4	2.00	98	108	93	81	76	60	64	74	42	15	1

Table II. Raw data from eleven focal-plane counters.

Run	$W_i (\times 10^8)$	Counter 1	2	3	4	5	6	7	8	9	10	11
Target in; μ^-												
27	4.00	17	28	26	22	27	11	10	5	4	2	0
29	4.00	21	25	20	16	21	11	12	5	6	4	0
33	4.00	15	25	22	17	15	9	10	7	3	8	2
35	8.00	53	49	41	41	28	34	18	25	13	3	0
37	8.00	52	53	41	48	30	21	20	17	18	8	4
39	2.70	21	18	16	14	10	6	5	8	2	1	0
1	6.00	48	39	36	23	22	19	13	18	10	5	1
3	6.00	43	34	30	23	27	15	19	15	11	4	5
5	6.00	47	30	26	21	15	14	13	11	11	1	2
7	8.00	56	41	32	40	33	27	19	27	12	8	1
1	6.00	49	28	36	31	37	25	23	15	7	7	4
3	8.00	56	43	66	39	36	29	25	21	8	9	6
5	8.00	60	45	56	48	24	31	22	22	17	7	2
7	5.00	35	26	33	31	20	28	12	24	12	6	2
	$\Sigma = 83.70$	573	484	481	414	345	280	221	220	134	73	29
Target out; μ^-												
26	2.00	4	3	0	4	2	9	2	4	0	1	0
28	2.00	3	4	4	4	1	4	3	3	3	2	0
30	2.00	3	4	5	2	7	4	0	4	0	1	0
34	2.00	5	2	2	3	3	1	2	4	3	0	0
36	4.00	10	6	4	6	10	4	7	5	1	3	1
38	4.00	9	12	10	6	5	4	3	6	2	0	0
40	1.35	2	4	1	2	0	2	3	2	1	0	0
2	3.00	8	2	6	4	5	3	4	5	4	1	0
4	3.00	7	5	7	1	1	5	3	6	3	2	1
6	3.00	8	5	10	8	6	11	2	3	2	2	0
8	3.54	8	10	7	6	8	5	4	5	4	2	0
2	2.15	4	3	7	4	4	2	1	3	5	2	0
4	4.11	9	6	4	6	5	1	6	8	6	3	0
6	3.89	5	5	5	3	7	2	4	4	6	3	2
8	2.50	5	6	8	4	4	4	3	7	2	1	2
	$\Sigma = 42.54$	90	77	80	63	68	61	47	69	42	23	6
Target in; μ^+												
31	4.00	1672	1679	1527	1408	1317	1122	967	932	679	264	54
Target out; μ^+												
32	2.00	88	96	83	98	82	76	87	76	60	46	20

Table III. Raw data from eleven focal-plane counters.

Run	$W_t (\times 10^8)$	Counter 1	2	3	4	5	6	7	8	9	10	11
Target in; μ^-												
3	8.00	55	47	41	35	40	32	26	14	8	8	1
5	8.00	44	46	42	24	28	15	17	20	12	4	5
7	6.00	25	27	21	28	16	15	11	17	7	2	2
9	8.00	37	22	34	26	24	20	18	18	13	5	5
11	8.00	38	51	32	31	36	25	13	14	8	2	1
13	8.00	39	28	33	35	26	24	13	13	10	3	3
15	8.00	37	44	36	40	23	24	15	19	7	2	2
17	8.00	32	45	34	31	31	17	18	17	8	4	0
21	8.00	51	34	42	36	20	14	9	19	7	7	1
23	8.00	40	37	36	29	32	24	14	20	6	13	3
25	4.30	31	21	15	23	16	13	8	8	4	1	2
3	8.00	36	36	20	29	22	15	22	18	9	2	1
5	8.00	46	38	30	28	32	23	15	22	5	0	2
7	1.28	10	6	4	6	4	4	4	3	1	1	2
2	8.00	37	31	32	25	30	23	12	18	16	2	3
4	8.00	49	33	29	27	25	21	24	17	7	8	2
6	8.00	43	44	35	24	27	14	19	14	9	1	2
8	8.00	43	42	42	26	21	17	17	15	11	2	2
10	8.00	31	46	33	28	34	20	14	13	7	6	1
12	8.00	41	42	34	32	25	22	20	11	11	2	0
14	8.00	52	40	26	29	24	24	20	19	5	6	2
18	8.00	46	44	35	32	38	32	20	19	10	7	3
	Σ= 163.58	863	804	686	624	574	438	349	348	181	88	45
Target out; μ^-												
4	4.00	1	3	7	6	6	7	3	3	1	0	2
6	4.00	7	3	4	6	6	2	4	6	7	0	0
8	3.40	5	6	3	5	1	3	1	2	2	0	0
10	4.00	8	6	3	5	4	2	3	4	3	1	0
12	4.00	8	5	4	10	5	5	6	4	0	3	1
14	4.00	6	10	6	2	6	3	5	2	2	0	1
16	4.00	6	10	7	5	1	1	6	7	4	4	1
18	4.00	9	4	4	4	3	4	4	6	3	2	0
20	2.00	3	2	1	3	4	0	0	2	0	3	1
22	4.00	5	5	6	9	3	2	6	6	1	1	0
24	3.00	6	4	9	4	3	2	2	5	1	3	0
4	4.00	7	4	4	3	2	5	3	4	4	5	0
6	4.00	5	4	4	6	2	4	4	4	3	2	0
3	4.00	5	6	4	6	7	3	10	1	3	1	1
5	4.00	4	4	5	1	5	6	5	6	2	3	0
7	4.00	6	8	6	2	4	5	3	1	4	1	0
9	4.00	3	5	6	6	1	6	7	8	1	2	1
11	4.00	12	5	6	0	6	2	7	4	3	2	1
13	4.00	5	3	5	4	5	2	3	8	4	4	1
15	4.00	5	2	2	7	4	3	7	5	0	3	0
19	4.61	12	9	5	5	6	6	5	8	7	0	0
	Σ= 81.01	129	108	101	99	84	73	94	96	55	40	10
Target in; μ^+												
1	6.00	2573	2487	2275	2191	2044	1755	1517	1420	1007	444	72
1	6.00	2356	2520	2198	2064	1938	1612	1490	1279	1012	410	85
	Σ= 12.00	4879	5007	4473	4255	3982	3367	3007	2699	2019	854	157
Target out; μ^+												
2	3.00	152	144	157	160	159	130	110	116	100	64	15
2	3.00	138	147	139	118	136	119	113	107	82	71	9
	Σ= 6.00	290	291	296	278	295	249	223	223	182	135	24

the presence of the nearby massive nucleus one can compute the negative spectrum for $\rho_m = 0.70$, say, and compare with the experimental data.

B. Results

When the experimental results were obtained and plotted several points became apparent. At the high momentum end of the measured spectrum the signal to noise (i.e. background) ratio in the last two focal plane counters 10 and 11 was very poor, a consequence of the background being comparable to the upper momentum tail of the spectrum. Hence the data from counters 10 and 11, constituting 2% of the total positive data and 3% of the total negative data was not used in the chi-square test. Due to the much smaller sample of negative decay events than positive events, statistical fluctuations have a more serious effect on the relative smoothness of the measured negative spectrum than upon the positive. Although only a small fraction of the running time was spent collecting positive data, we still collected roughly ten times as many positrons ($\sim$ 60,000 e^+) as electrons ($\sim$ 6,000 e^-).

Table IV gives the results of the chi-square tests. Column 4 in Table IV presents the results for the negative spectrum for $\rho_M = 0.70$. Figures 18 through 29(after Table V) show the experimental data together with the theoretical predication for the various groups of data. The data labeled II + III is the result of combining the data in groups II and III into one group. For comparison the positive and negative data of group II + III (constituting the bulk of the data)

are shown together in Figures 31 and 32. Note that the positive (solid) curve for $\rho_M = 0.75$ is the same in both Figures 31 and 32 while the negative (dashed) curves are for $\rho_M = 0.75$ (Figure 31) and for $\rho_M = 0.70$ (Figure 32), respectively. Appendix D contains the formulas used in the chi-square test.

Table IV. Chi-square test results ($\rho = 0.75$)

Data From	(+) Spectrum	(-) Spectrum	(-)($\rho = 0.70$)
Table I	10.0	14.6	13.1
Table II	9.5	15.5	13.0
Table III	5.8	25.8	22.0
Table II+III	7.0	32.0	26.7

For seven degrees of freedom the corresponding probabilities that another measurement of the same quantities would give larger chi-squares is presented in Table V following.

Table V. Probabilities for larger chi-squares

Data From	(+) Spectrum	(-) Spectrum	(-)($\rho = 0.70$)
Table I	.19	< .05	.07
Table II	.23	< .05	.07
Table III	.56	< .05	< .05
Table II+III	.43	< .05	< .05

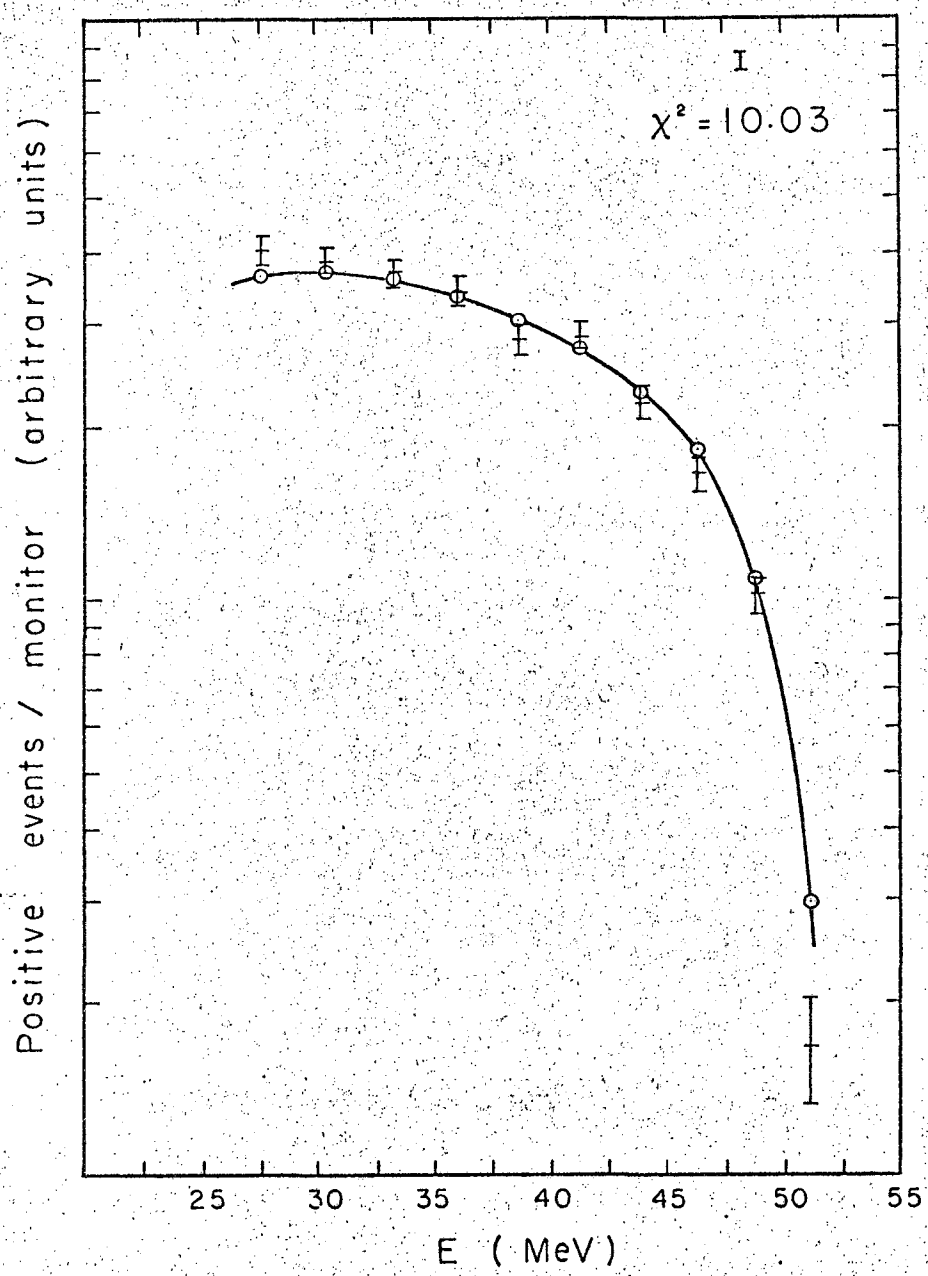

MUB-13023

Fig. 18. Positive spectrum from Table I. $\rho_M = 0.75$

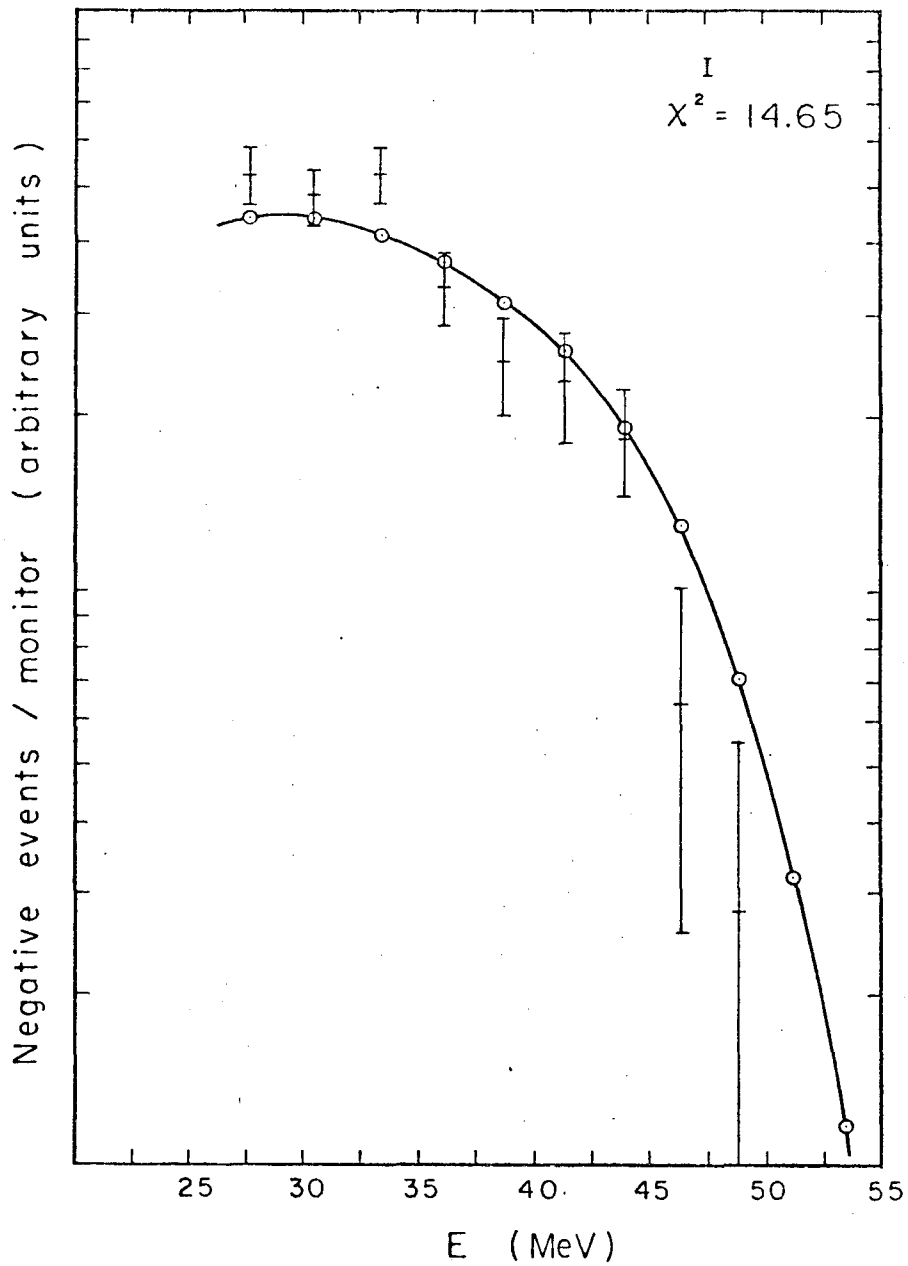

MUB-13022

Fig. 19. Negative spectrum from Table I. $\rho_M = 0.75$

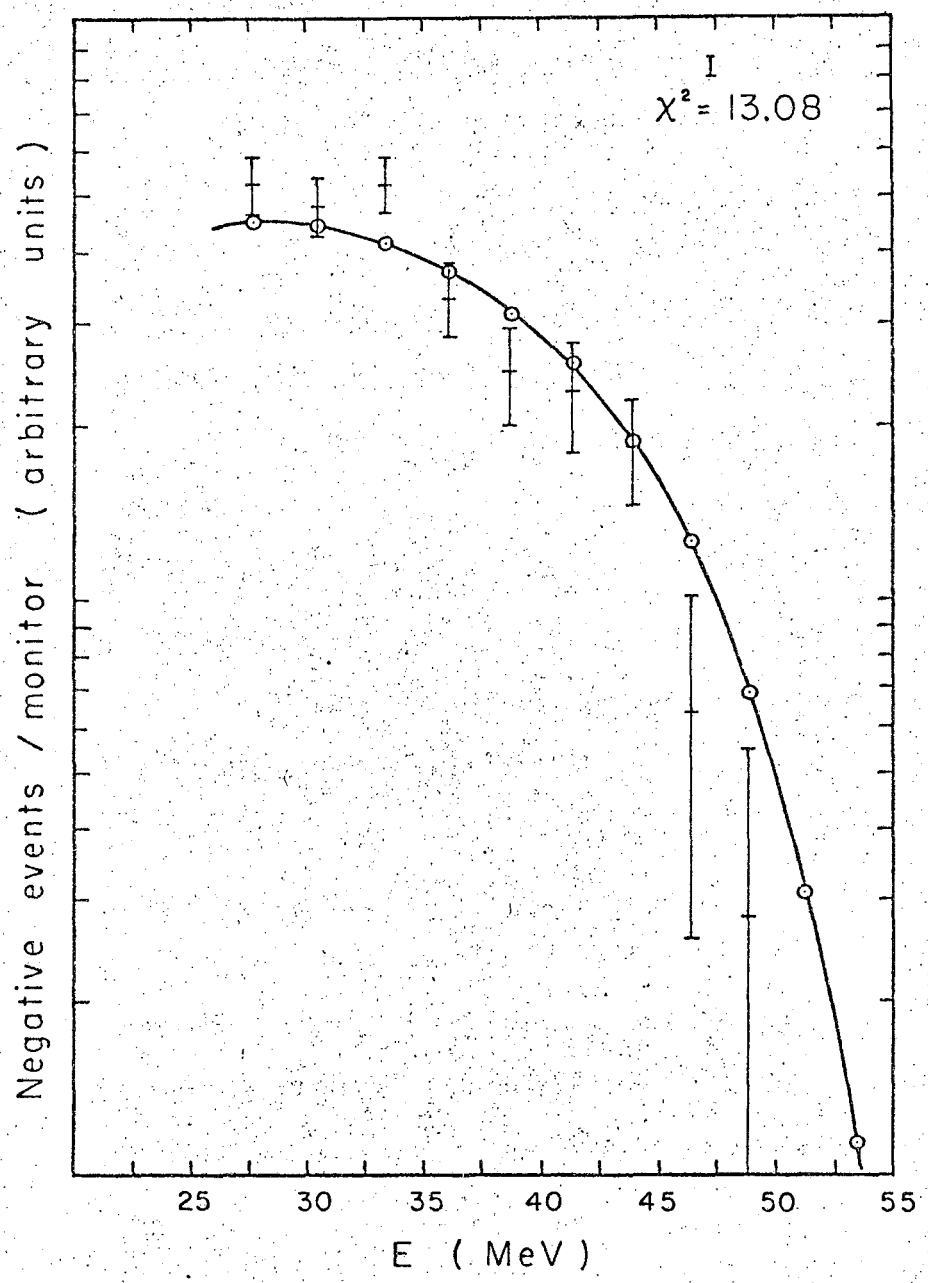

MUB-13020

Fig. 20. Negative spectrum from Table I. $\rho_M = 0.70$.

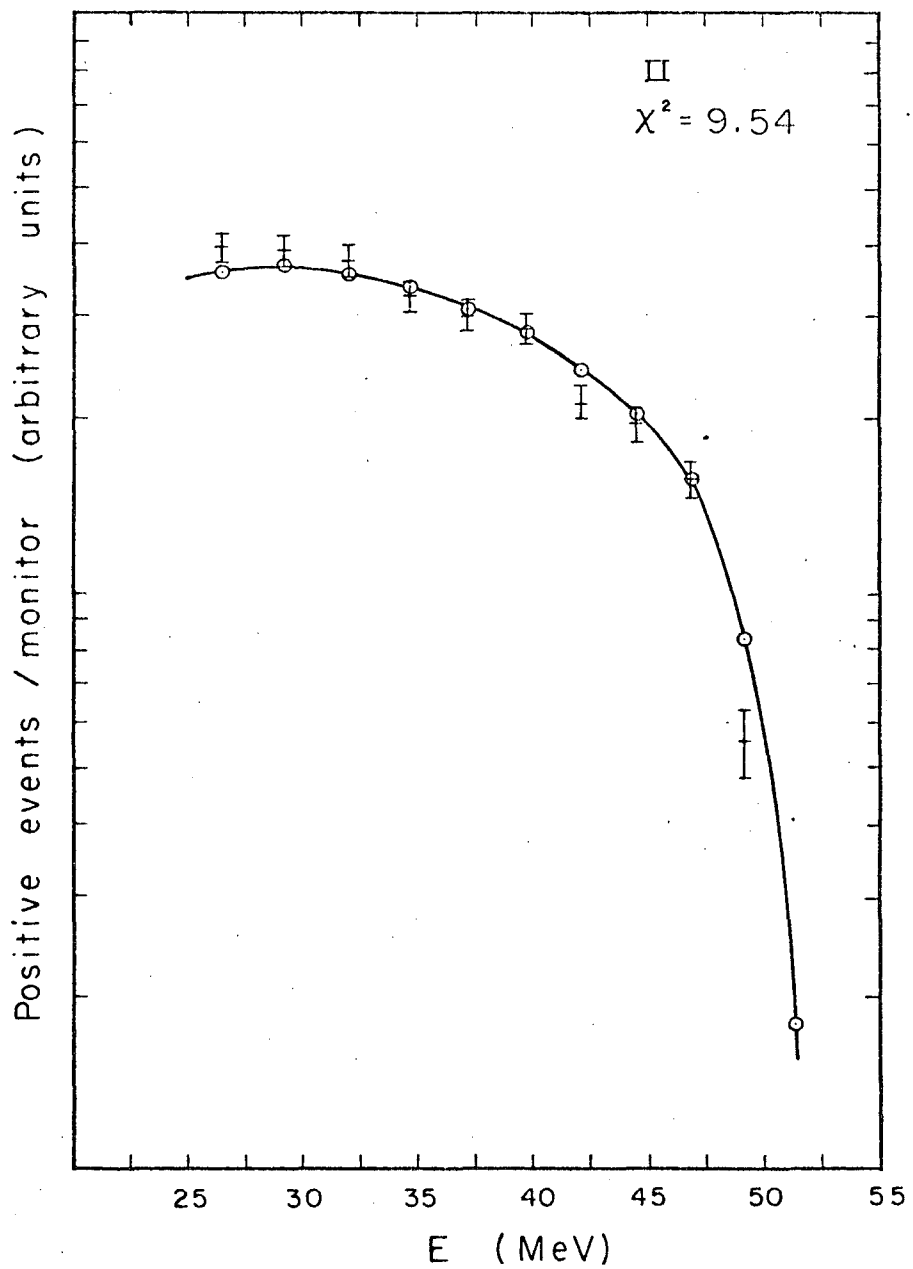

MUB-13021

Fig. 21. Positive spectrum from Table II. $\rho_M = 0.75$.

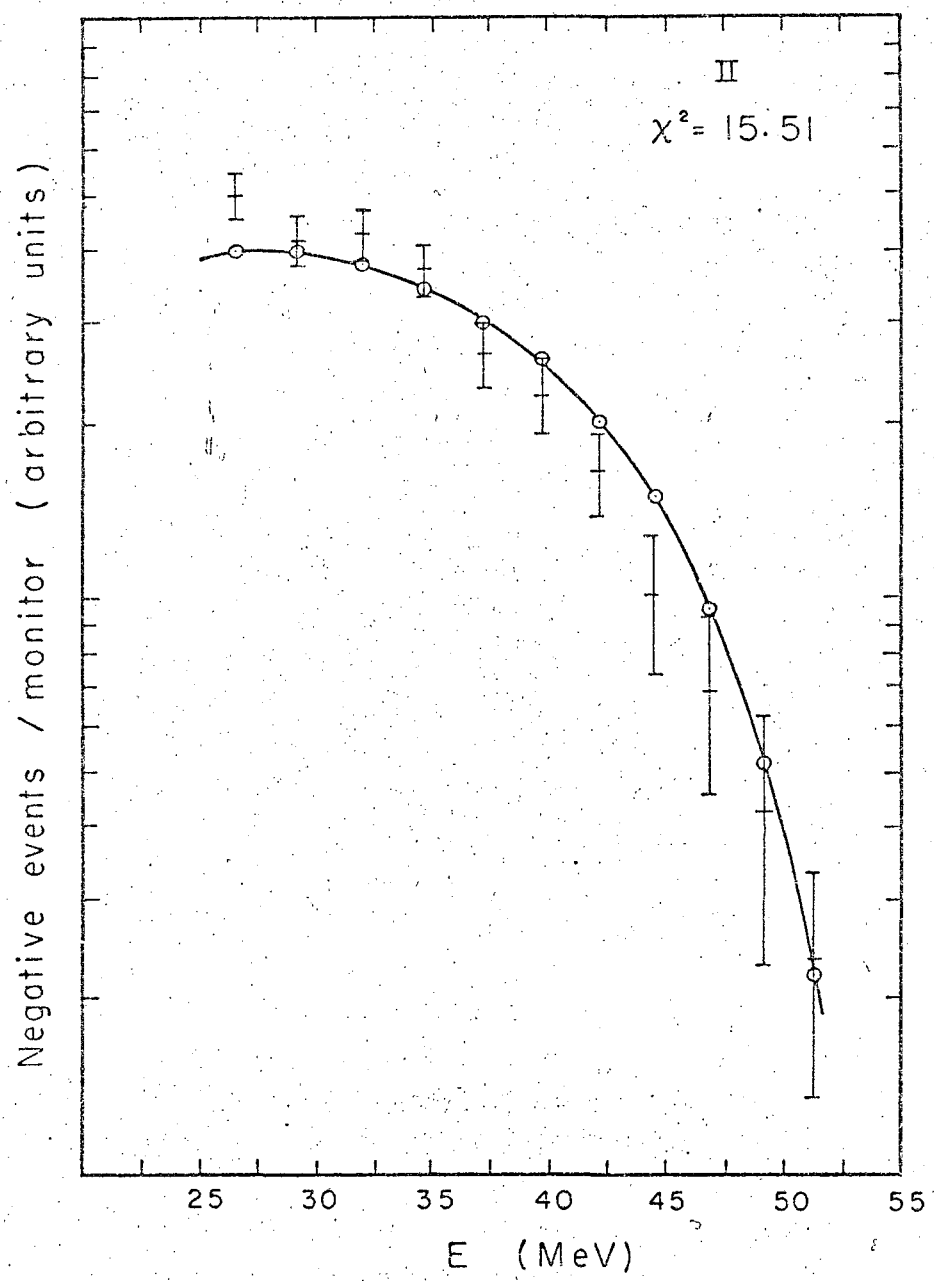

MUB-13026

Fig. 22. Negative spectrum from Table II. $\rho_M = 0.75$.

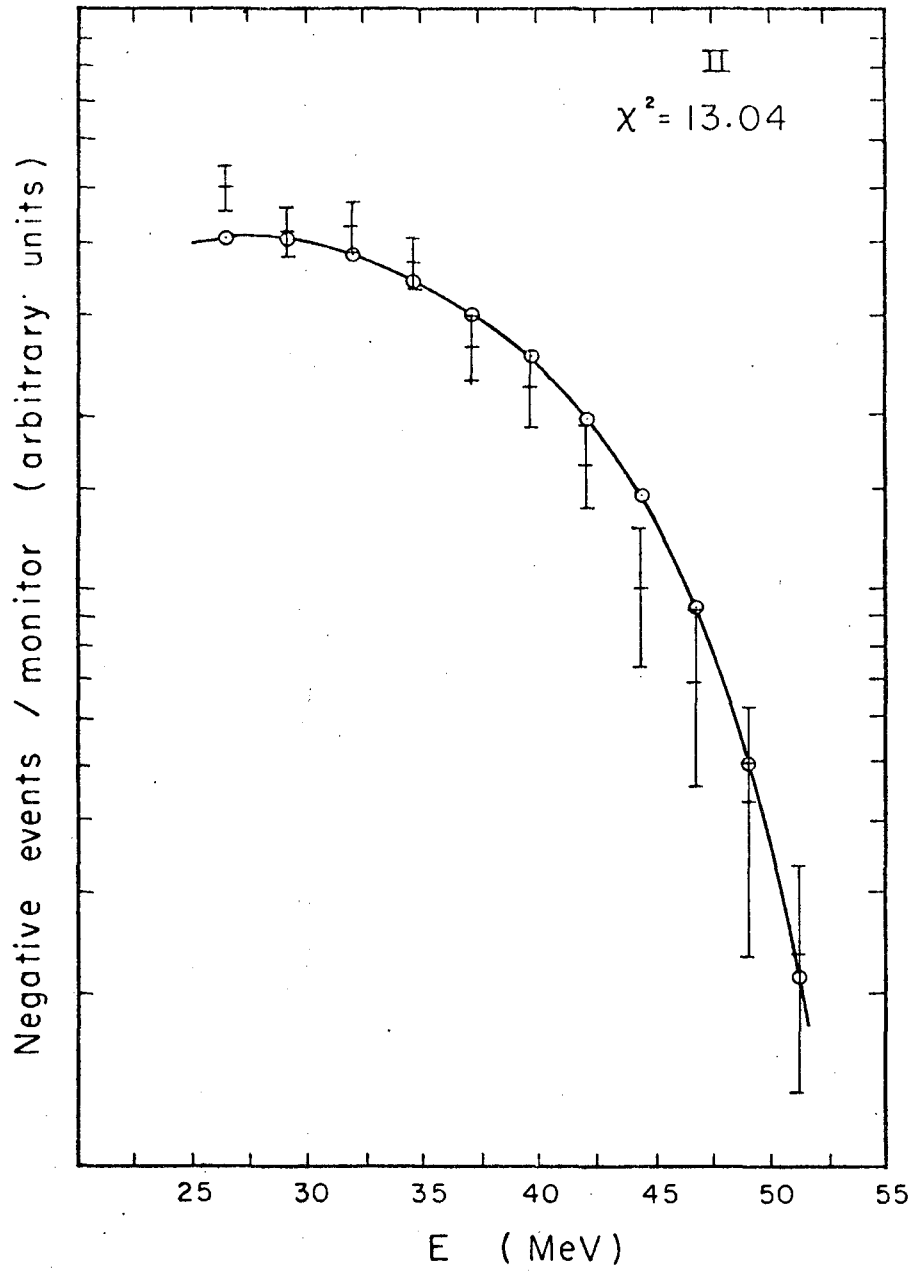

MUB-13025

Fig. 23. Negative spectrum from Table II. $\rho_M = 0.70$.

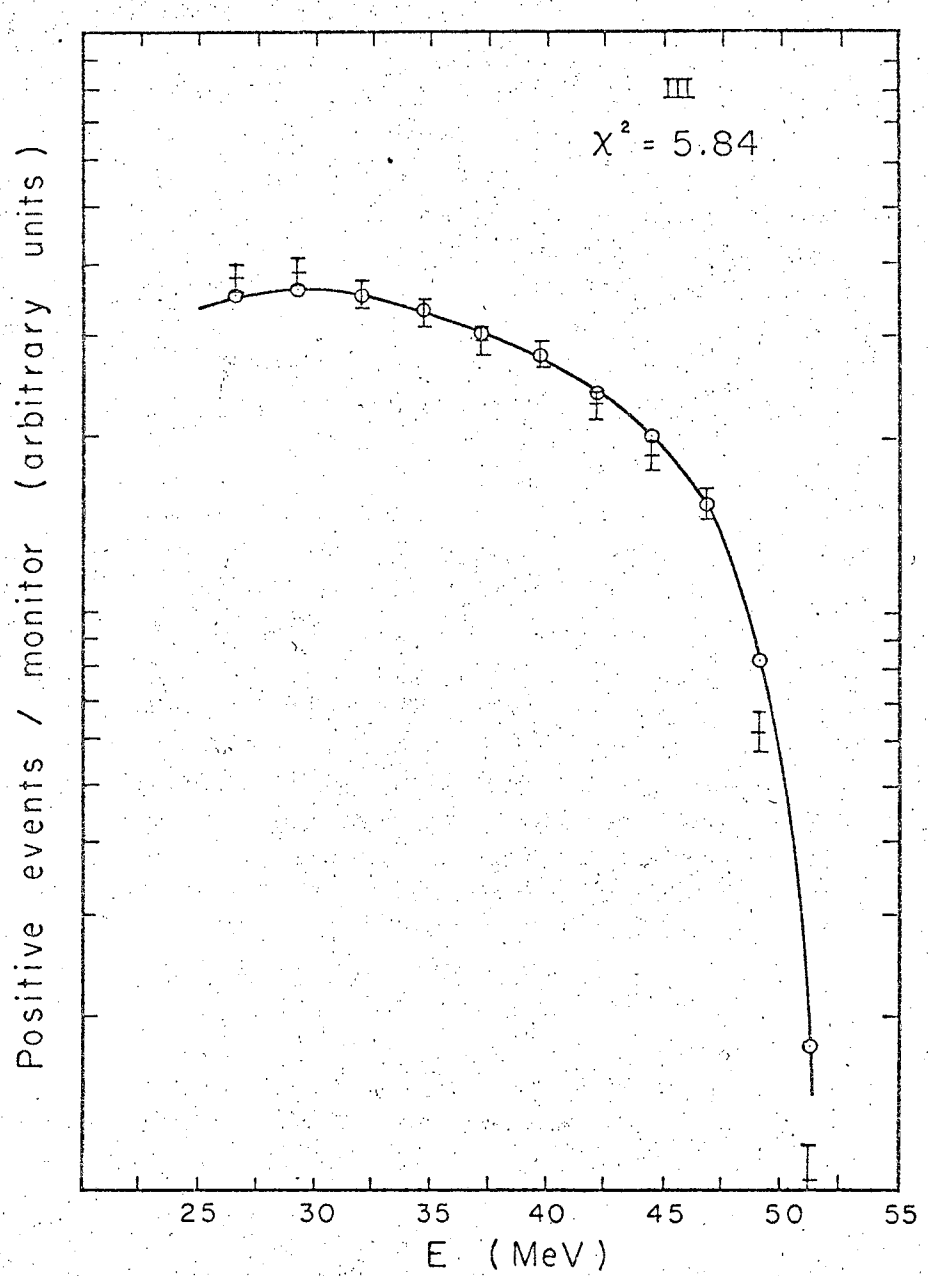

MUB-13024

Fig. 24. Positive spectrum from Table III. $\rho_M = 0.75$.

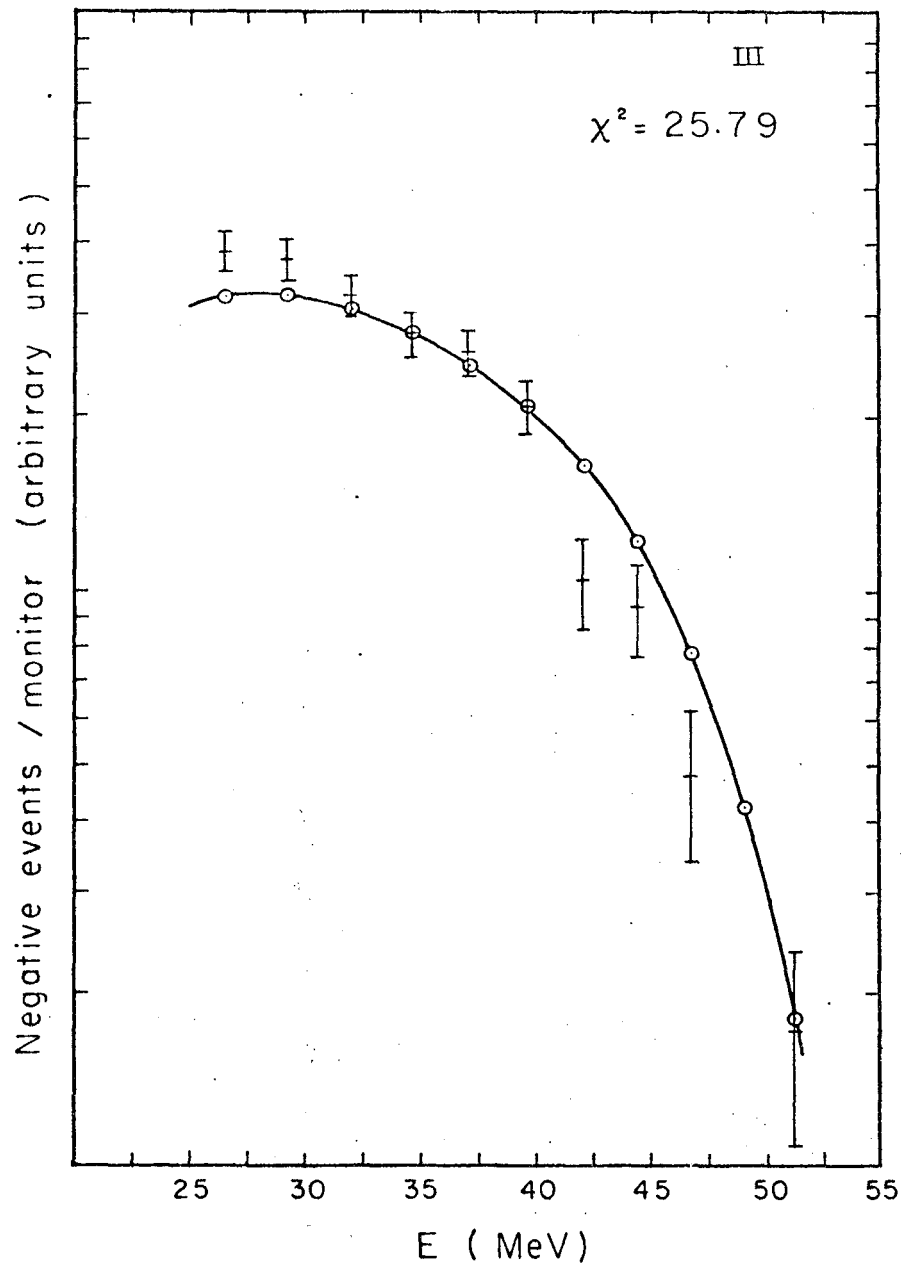

MUB-13027

Fig. 25. Negative spectrum from Table III. $\rho_M = 0.75$.

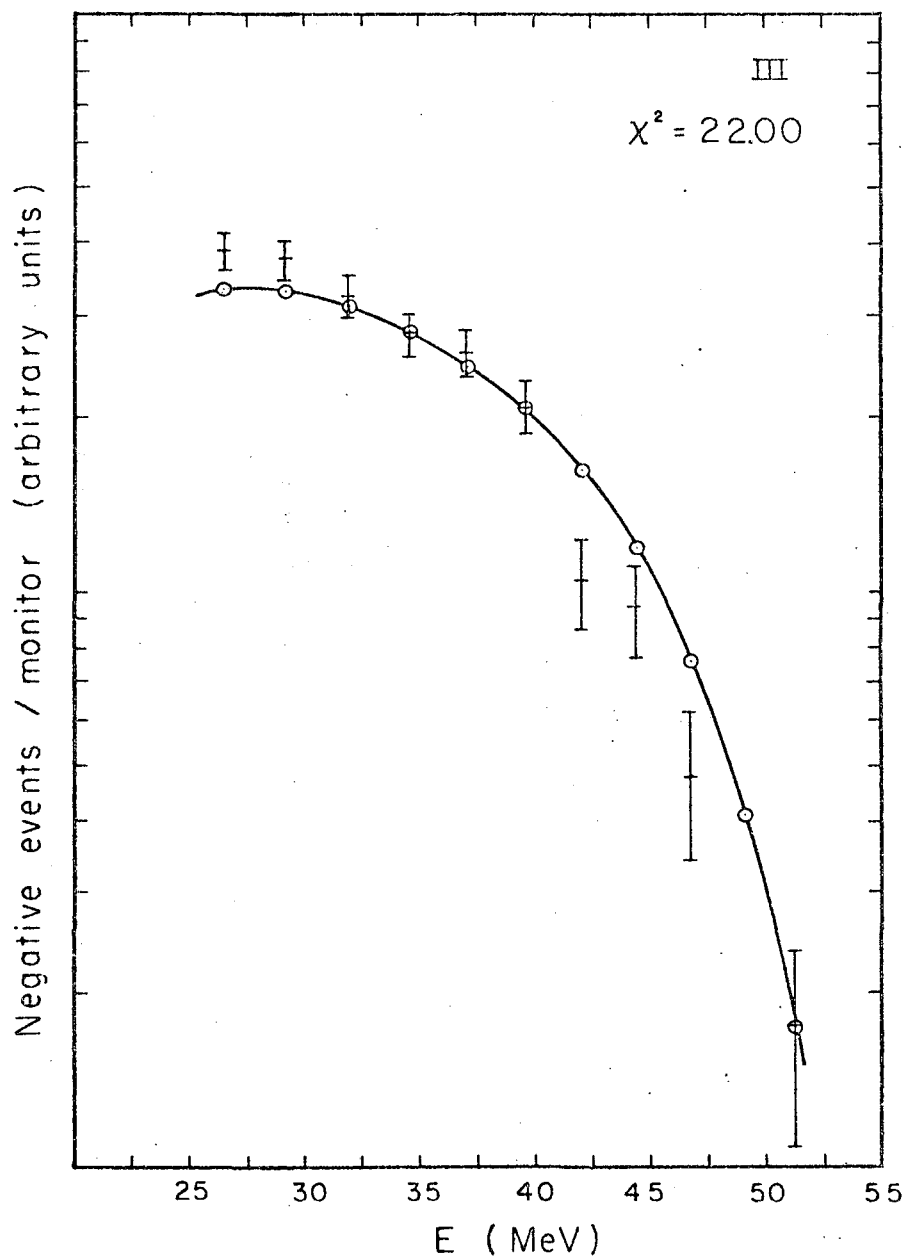

MUB-13028

Fig. 26. Negative spectrum from Table III. $\rho_M = 0.70$.

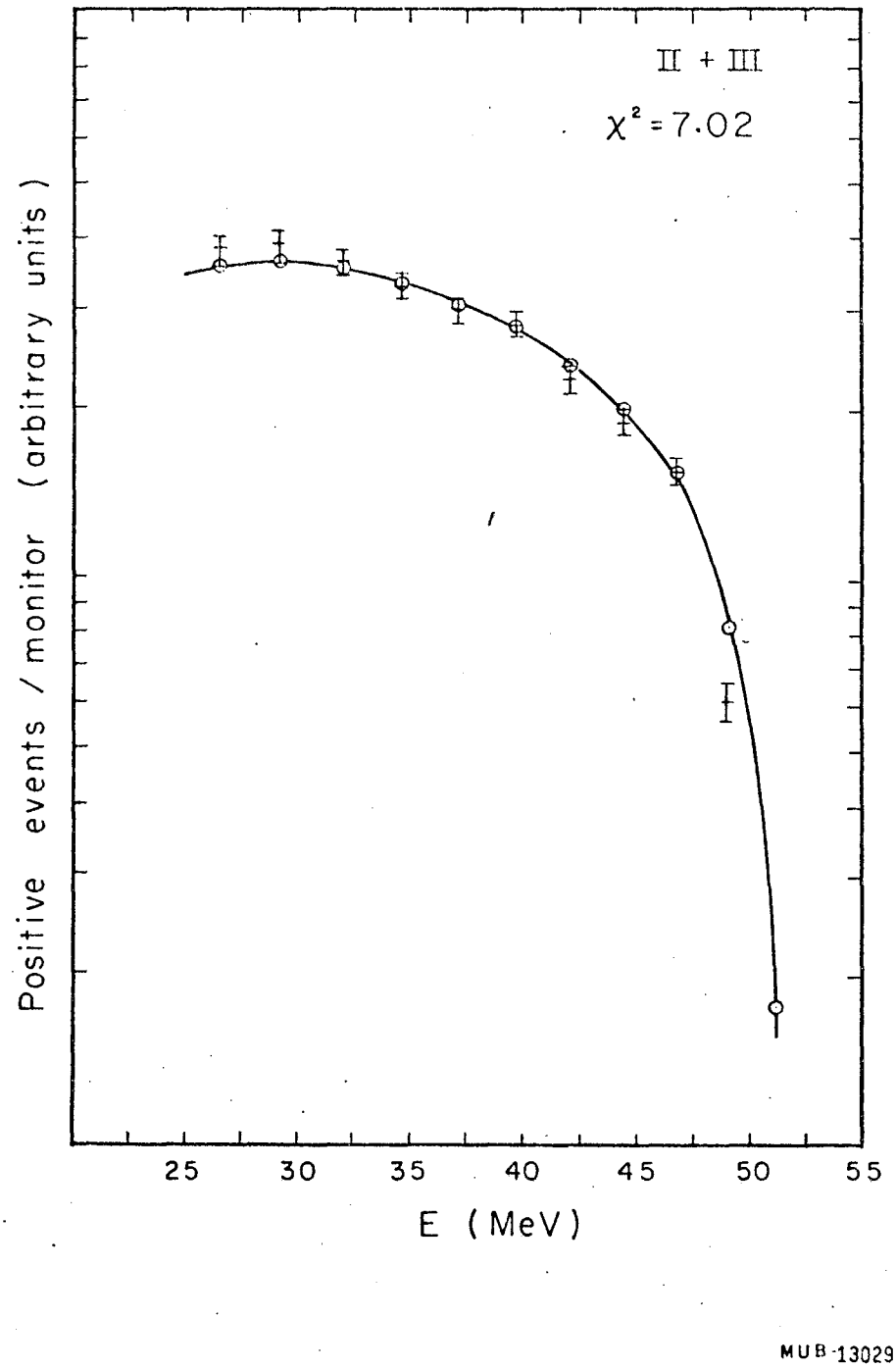

Fig. 27. Positive spectrum from Tables II + III. $\rho_M = 0.75$.

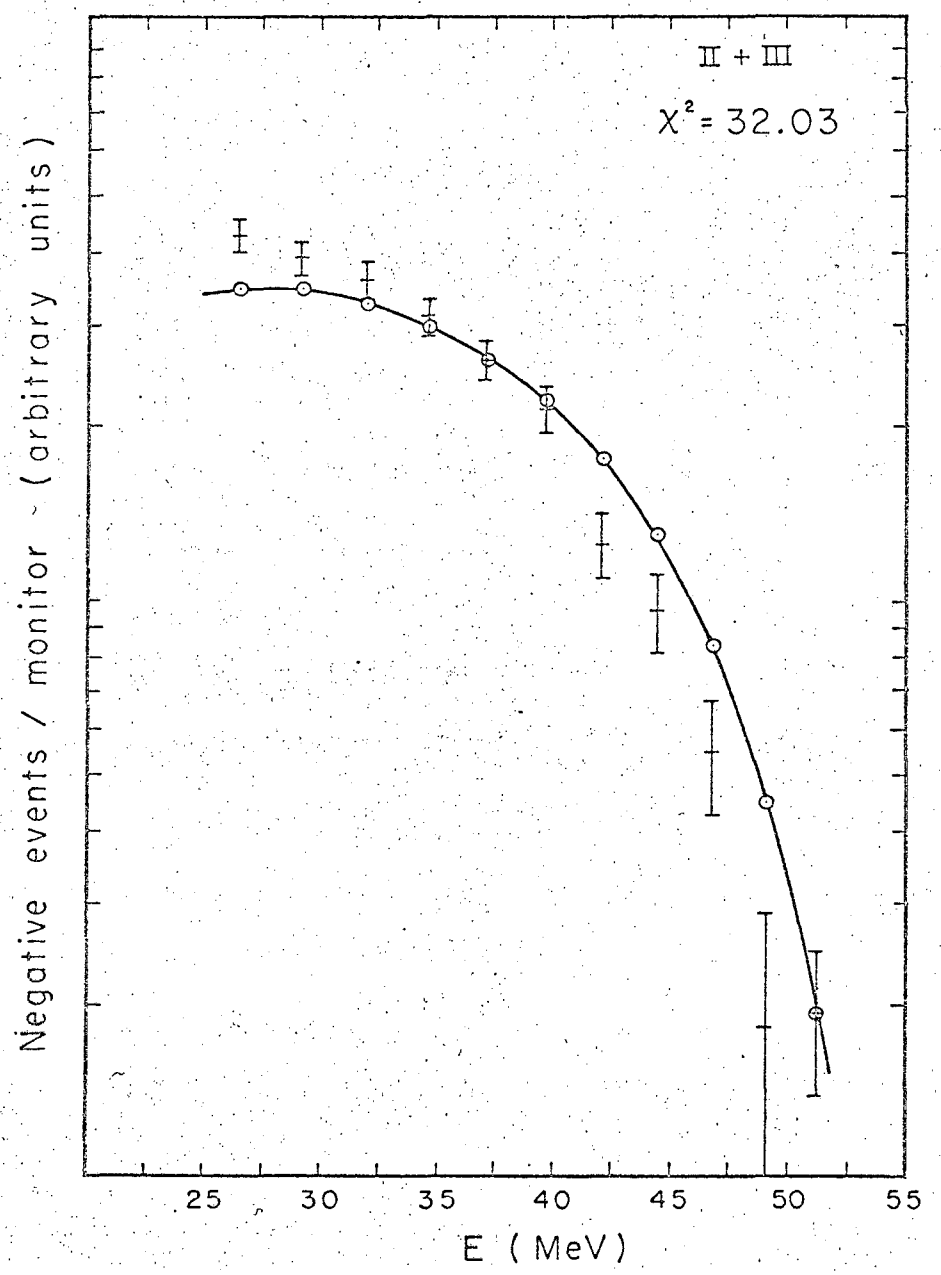

MUB-13030

Fig. 28. Negative spectrum from Tables II + III. $\rho_M = 0.75$.

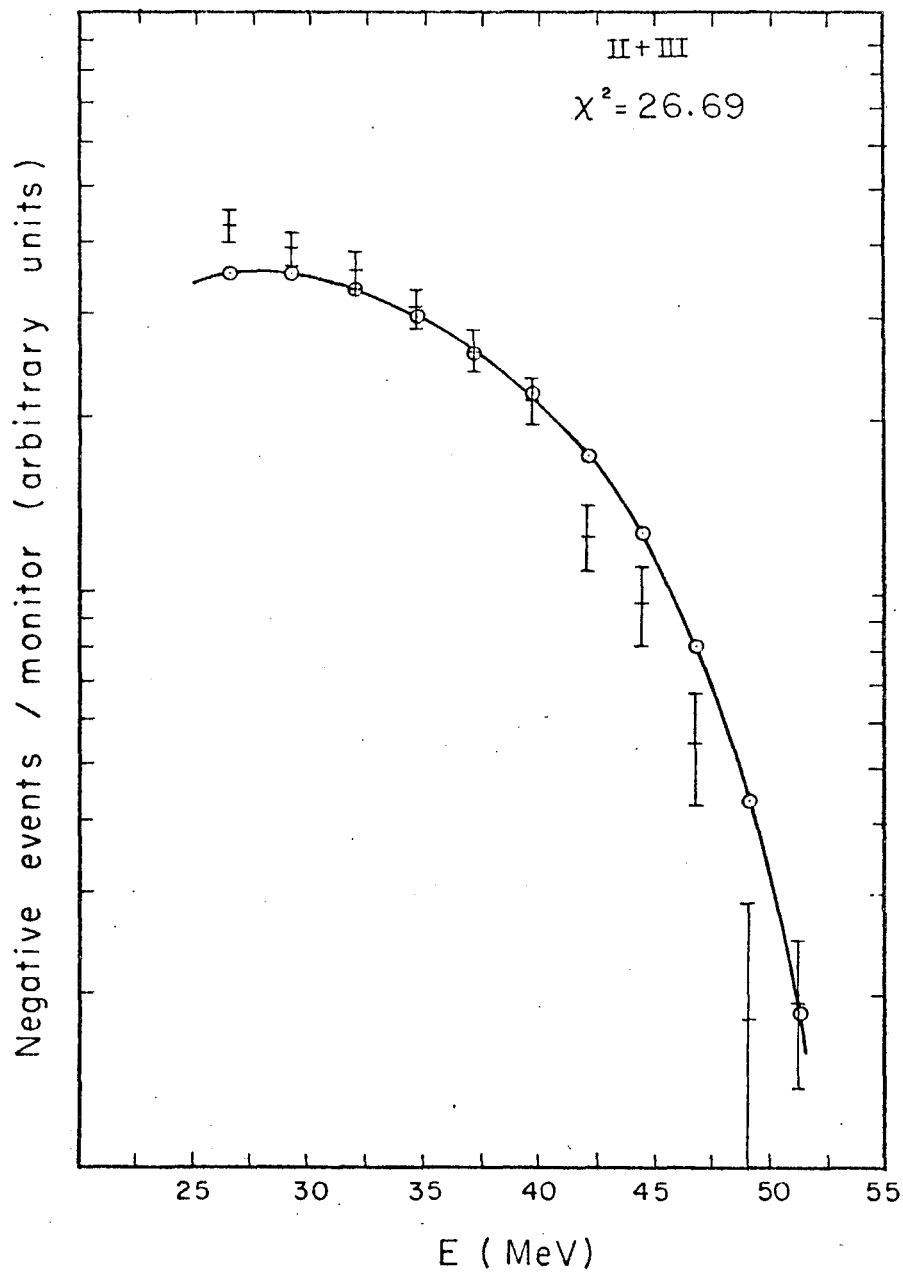

MUB-13031

Fig. 29. Negative spectrum from Tables II + III. $\rho_M = 0.70$.

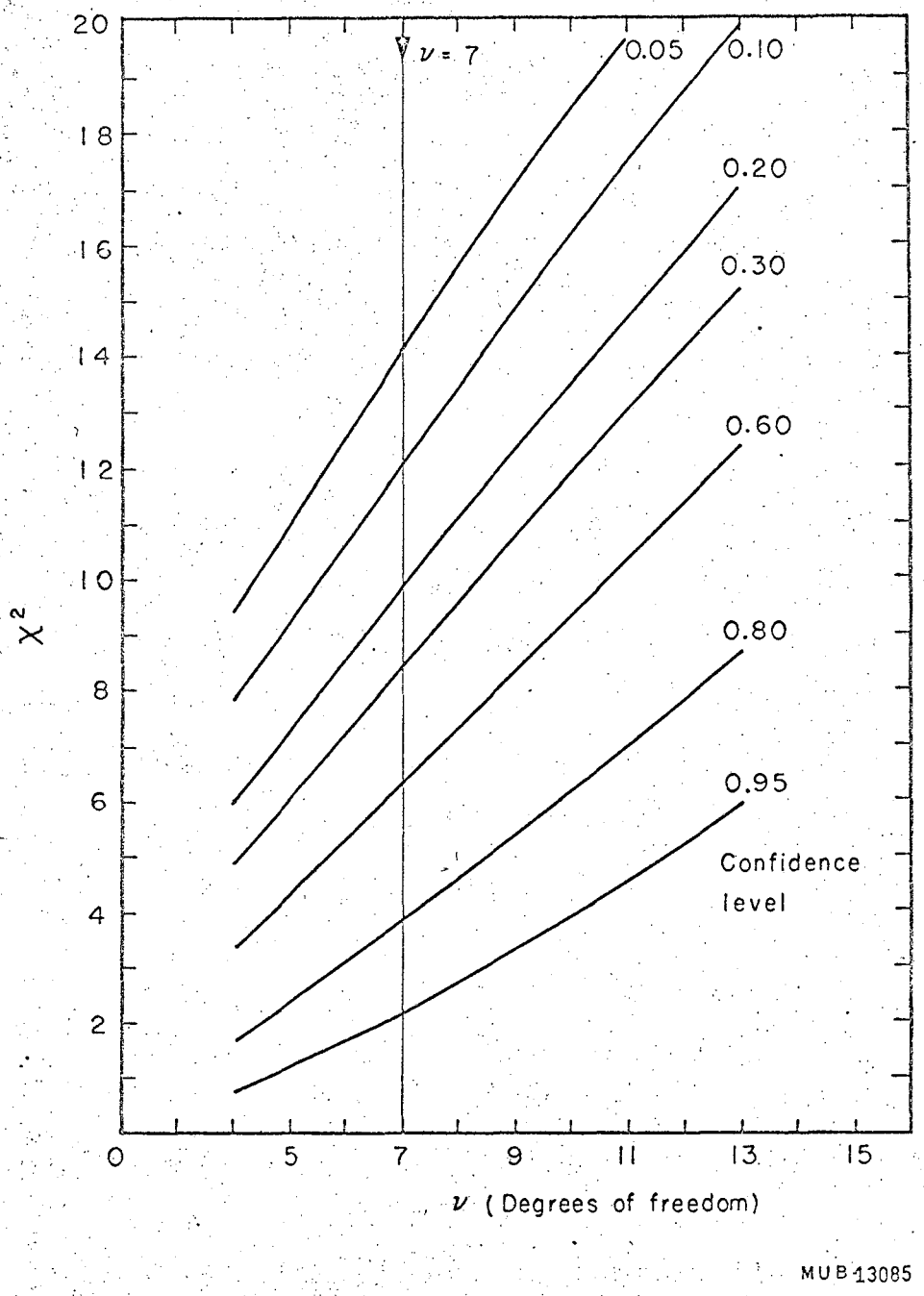

Fig. 30. Chi-square, χ^2, versus Degress of Freedom, ν.

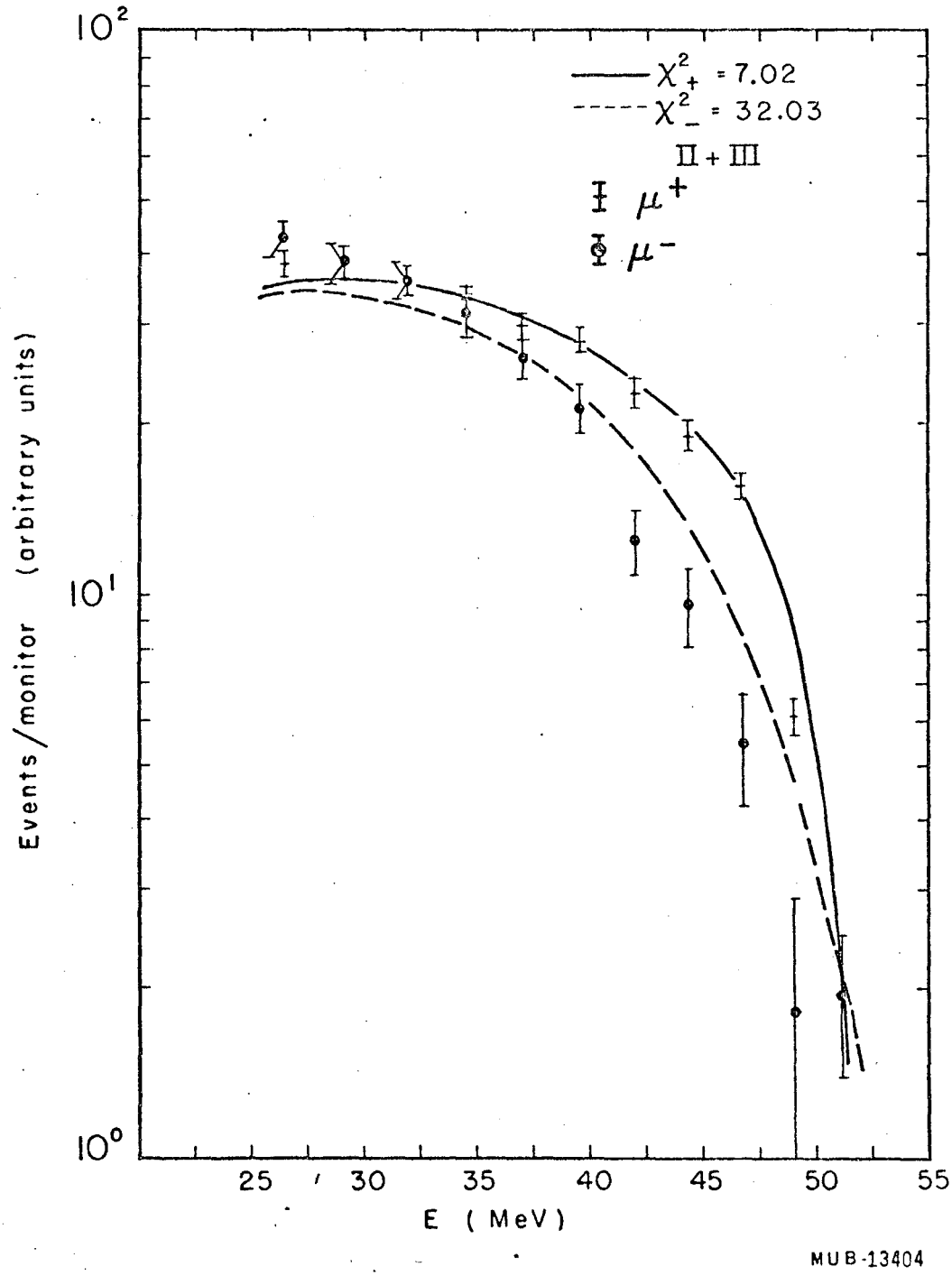

Fig. 31. Combined results from Figure 27 for the positive spectrum ($\rho_M = 0.75$) and from Figure 28 for the negative spectrum ($\rho_M = 0.75$).

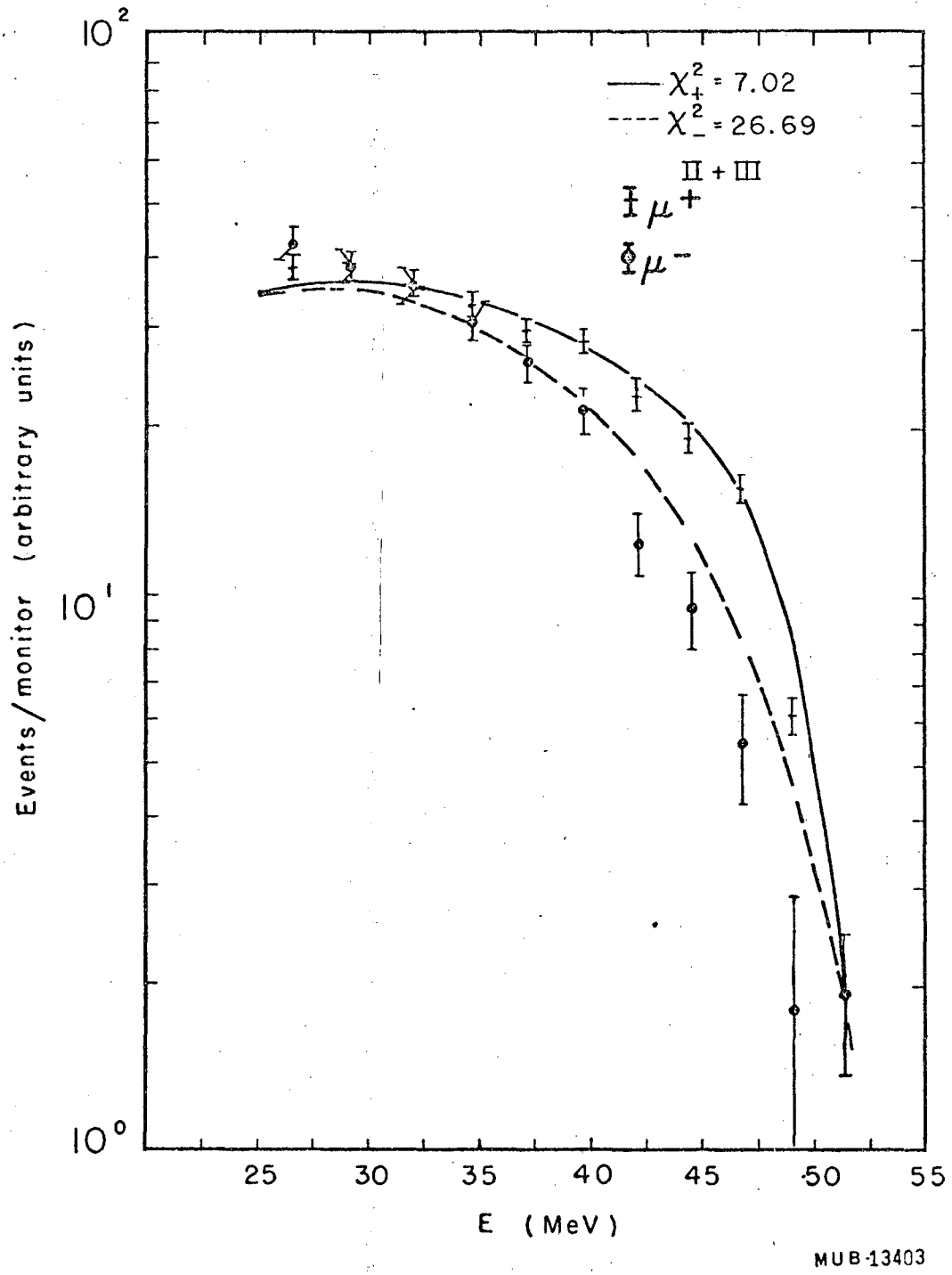

Fig. 32. Combined results from Figure 27 for the positive spectrum ($\rho_M = 0.75$) and from Figure 29 for the negative spectrum ($\rho_M = 0.70$).

C. Comparison of Results and Conclusions

From the many experiments designed to measure the muon decay spectrum only four (including this experiment) have tried to determine the bound muon decay spectrum in medium or high Z materials.[38,39,40] Some of the important experimental aspects are listed in Table VI below.

Table VI

	Target	Thickness* (g/cm^2)	Energy Resolution
Bergeson (1961)	Iron	5.0	---------
	Zinc	4.4	---------
Culligan (1961)	Iron	1.8	17% at 50 MeV
Nielsen (1962)	Titanium	7.3	---------
	Iron	7.5	---------
	Lead	3.5	---------
This experiment	Copper	2.8	12-1/2% at 44 MeV

*In direction of the electron detector.

Both Bergeson and Nielson used the same experimental techniques (and essentially the same apparatus) to measure the muon decay spectra. They stopped cosmic ray muons in the various targets and measured the decay electron energies utilizing a deep 12" carbon tetrachloride ($CC\ell_4$) total absorption Cerenkov counter. In order to decrease sensitivity to low energy gammas their counters were biased so as to discriminate against pulses corresponding to 6 to 11 MeV in magnitude.

The primary experimental problems were being able to distinguish between the negative and positive muon decays and the poor energy resolution of the $CC\ell_4$ Cerenkov counter. The resultant experimental spectra were too rough to conclude anything regarding Huff's theoretical prediction. Indeed Bergeson's data for the bound muon spectra in iron and zinc indicated that these spectra were not grossly different from the positive muon spectrum.

Culligan, et al., utilized a relatively thin iron target to stop negative muons from the Cern synchrocyclotron. To eliminate any residual polarization the target was placed in a high magnetic field of 10,000 gauss. The energy of the decay electrons were measured by a large (20 x 20 cm) NaI(Tℓ) counter. It was estimated that 20% of the incident events into the NaI counter gave no counts and these were attributed partly to gammas originating in muon capture. However, 8% of these events also were present in the positive muon decay events. These "no-count" events constituted about a 5 MeV lower energy cut-off. The measured decay spectrum was compared to Uberall's model with the NaI resolution folded in. There appeared to be reasonably good agreement except at energies below 20 MeV where an excess of events were noticed.

Experimentally the main difference between this experiment and the other three experiments is the use of the magnetic spectrometer for energy analysis rather than the use of a total absorption counter. The low end energy cut-off of $\sim$ 20 MeV in this experiment is due primarily to the solid angle cut off of the focal plane counters.

Since the focal plane scintillation counters are shielded from direct line of sight with the copper target, no low energy gammas or neutrons from the target were counted. The main source of background difficulty appears to originate from muon decays occurring in the 1/8" thick T counter immediately in front of the copper target. Indeed, the background with the target removed agrees crudely with the positive decay spectrum both for positive and negative muon decays as one would predict for muons decaying in low Z material such as polystyrene (CH).

The experimental spectra for the positive decays show fairly good agreement with theory as indicated by the chi-square test. The negative data, on the other hand, shows indications of not being in agreement. Even when ρ_M is reduced from 0.75 to 0.70 for the negative spectrum, hopefully to compensate for not including the internal radiative corrections, the probabilities do not improve markedly. There still appears to be a distinct tendency for the negative spectrum to fall off faster at the high energy end of the spectrum than theory would predict. Any large correction applied to the negative spectrum must necessarily be applied likewise to the positive spectrum. The positive spectrum however, does not appear to require any correction of the magnitude necessary to bring the negative spectrum into agreement.

In view, however, of the large energy dependent corrections made to the theoretical spectra before they were compared to the data, one must be cautious before laying the blame entirely at the feet of the theory. Certainly the general predictions of the theory regarding a downward energy shift in the bound spectrum are clearly born out by

the experimental data. The negative data is distinctly different from the positive and is shifted toward lower energies. The predicted Doppler smearing of the spectrum is also present but is not seen very distinctly due to the poor statistics at the upper energy end of the spectrum. The disagreement between the rate at which the experimental bound spectrum and the theoretical spectrum fall off with energy may be indicative of the need for larger internal radiative corrections in the presence of a heavy nucleus.

ACKNOWLEDGMENTS

I would like to thank Professor Kenneth M. Crowe for suggesting this experiment and for his criticisms during the carrying out of the experiment and the subsequent data analysis. It is a pleasure to acknowledge the many useful discussions regarding theoretical aspects of the bound muon decay spectra with Dr. Robert Huff. Dr. Robert Riddell was of great help in improving the accuracy of the bremsstrahlung calculation. For assistance with computer programing problems I would like to thank Mr. Loren Meissner, Miss Margery Simmons, and Miss Elaine Horvorka.

The cyclotron crew under the direction of Mr. James Vale provided the many hours of steady beam. For assistance during the running of the experiment I would like to thank especially Dr. Tin Maung, Dr. Robert Beck, and Mr. Ned Dairiki. Lastly I would like to express my thanks to my wife for her patience and constant encouragement.

This work was performed under the auspices of the U. S. Atomic Energy Commission.

APPENDICES

A. Theoretical Spectrum

Calculation of $R_2^+(X)$

$$R_2^+(X) = \frac{4x^2[1 + h(x)]}{1 + \Lambda_1 + \frac{2}{3}\rho_M(\Lambda_2 - \Lambda_1)} \{3(1-x) + 2\rho_M[(4/3)x - 1)]\} \qquad (1)$$

$$x = \frac{p_e C}{p_e C_{max}} \text{ where } p_e C_{max} = \frac{M\mu^2 + m_e^2}{2M\mu} \approx \frac{M\mu}{2} = 52.83 \text{ MeV/c} \qquad (2)$$

$$\Lambda_{1,2} = 4\int_0^1 h(x)\ [3(1-x);x]\ x^2\ dx \qquad (3)$$

Integration result: $\Lambda_1 = 0.0132$,

$\Lambda_2 = -0.0216$

$$h(x) = \frac{\alpha}{2\pi}\frac{f(x)}{3-2x} \quad \alpha = \text{fine structure constant} = e^2/\hbar C = 1/137.039 \qquad (4)$$

$$f(x) = (6-4x)R(x) + (6-6x)\ln_e x + \left(\frac{1-x}{3x^2}\right)[(5 + 17x - 34x^2)(\omega + \ln_e x)$$

$$-22x + 34x^2] \qquad (5)$$

$$\omega = \ln_e \frac{m_\mu}{m_e} = 5.332 \qquad (6)$$

$$R(x) = 2\sum_{n=1}^{\infty} \frac{x^n}{n^2} - \frac{1}{3}\pi^2 - 2 + \omega[3/2 + 2\ln_e(\frac{1-x}{x})] - \ln_e x$$

$$\cdot\ (2\ln_e\ x-1) + (3\ln_e x-1-\frac{1}{x})\ \ln_e(1-x) \qquad (7)$$

$$\sum_{n=1}^{\infty} \frac{x^n}{n^2} = -L(x) = -\int_0^x \frac{dt}{t} \ln(|1-t|) \qquad (8)$$

where L(x) is called Spence's function.[58]

B. Bremsstrahlung

With the kind permission of Dr. Riddell of the Lawrence Radiation Laboratory, the main outline of his bremsstrahlung calculation is presented in the following discussion.

Let $n(E,t)$ = number of electrons of energy E, at a depth t in the target.

Then,

$$\frac{\partial[n(E,t)dE]}{\partial t} = \underbrace{\int_{E}^{E_o} \Phi(E',E)dE\ n(E',t)dE}_{I_I} - \underbrace{\int_{0}^{E} \Phi(E,E')dE'\ n(E,t)dE}_{I_{II}} \qquad (1)$$

where $\Phi(E',E)dE$ = prob. electron changes energy from $E' \rightarrow \{E, E + dE\}$ per unit distance

In I_I:

$$E = (1-v)E' \quad \text{where } v = \frac{E'-E}{E'} \qquad (2)$$

so

$$E' = \frac{E}{1-v} \qquad (3)$$

can write

$$\Phi(E',E)dE = \Xi(E',v)dv \qquad (4)$$

so

$$I_I = \int_{E}^{E_o} \Xi(E',v)dv\ n(E',t)dE' \qquad (5)$$

and

$$dE' = \frac{dE}{1-v} \tag{6}$$

Thus

$$I_I = \int_0^1 \Xi(\frac{E}{1-v}, v) n(\frac{E}{1-v}, t) \frac{dE\, dv}{(1-v)} \tag{7}$$

In I_{II}

$$E' = (1-v)E \tag{8}$$

and

$$I_{II} = \int_0^1 \Xi(E,v)\, n(E,t)\, dE\, dv \tag{9}$$

Thus

$$\frac{\partial n(E,t)}{\partial t} = \int_0^1 \Xi(\frac{E}{1-v}, v) n(\frac{E}{1-v}, t) \frac{dv}{(1-v)} - \int_0^1 \Xi(E,v) n(E,t) dv \tag{10}$$

ansatz:

$$\begin{aligned} \Xi(E,v) &= \phi_o(v) + E\, \phi_1(v) + E^2(v) + \ldots . \\ &= \psi_o(u) + E\, \psi_1(u) + E^2(u) + \ldots . \end{aligned} \tag{11}$$

let

$$u = \ln \frac{1}{1-v} \tag{12}$$

$$\exp(u) = \frac{1}{1-v} \tag{13}$$

$$y = \ln \frac{E_o}{E} \tag{14}$$

$$\frac{E}{1-v} = E_o \exp(-y + u) \tag{15}$$

$$dv = \exp(-u)du \tag{16}$$

Equation 10 becomes

$$\frac{\partial n(y,t)}{\partial t} = \int_0^\infty \{\exp(u)\, n(y-u,t)[\psi_o(u) + \exp(-(y-u))E_o\, \psi_1(u) + \ldots]$$

$$-n(y,t)[\psi_o(u) + E_o \exp(-y)\psi_1(u) + \ldots]\}\exp(-u)du \tag{17}$$

Multiply both sides by $\exp(-\xi\, y)$ and integrate over y from 0 to ∞

$$\frac{\partial p(\xi,t)}{\partial t} = \int_0^\infty \exp(-\xi u)dy \int_0^y du\; n(y-u,t)[\psi_o(u)+E_o\exp(-(y-u))\psi_1(u)+\ldots]$$

$$-\int_0^\infty \exp(-\xi y)dy \int_0^\infty n(y,t)\exp(-u)du[\psi_o(u)+E_o\exp(-y)\psi_1(u)+\ldots] \tag{18}$$

$$=\int_0^\infty \exp(-\xi u)du \int_u^\infty dy\; \exp[-\xi(y-u)]n(y-u,t)[\psi_o(u)+E_o\exp(-(y-u))\cdot$$

$$\cdot\, \psi_1(u)+\ldots]$$

$$-\int_0^\infty \exp(-\xi y)dy\; n(y,t) \int_0^\infty \exp(-u)du[\psi_o(u)+E_o\exp(-y)\psi_1(u)+\ldots]$$

$$\frac{\partial p(\xi,t)}{\partial t} = p(\xi,t)\int_0^\infty (\exp(-\xi u)-\exp(-u))\psi_o(u)du$$

$$+p(\xi+1,t)E_o\int_0^\infty (\exp(-\xi u)-\exp(-u))\psi_1(u)du+ \ldots \tag{19}$$

where

$$p(\xi,t) = \int_0^\infty \exp\,(-\xi y)\; n(y,t)dy \tag{20}$$

Now let

$$\psi_o(u) = \sum_{n=1}^{\infty} a_n\, u^{n-1} = \frac{a_o}{u} + \sum_{n=1}^{\infty} a_n\, u^{n-1} \tag{21}$$

Consider the first integral in Eq. 19.

$$I_o(\xi) = \int_0^\infty (\exp\,(-\xi u) - \exp(-u))\; \psi_o(u)du \tag{22}$$

$$\frac{dI_o(\xi)}{d\xi} = -\int_0^\infty \exp(-\xi u)\{a_o + \sum_{n=1}^{\infty} a_n u^n\}du = -\;[\frac{a_o}{\xi} + \sum_{n=1}^{\infty} \frac{a_n\; n!}{\xi^{n+1}}\;] \tag{23}$$

Integrating

$$I_o(\xi) = -a_o \ln\xi + \sum_{n=1}^{\infty} a_n (n-1)!\,[\frac{1}{\xi^n} - 1] = -a_o \ln\xi + \Theta_o(\xi) \tag{24}$$

Rewriting Eq. 19

$$\frac{\partial p(\xi,t)}{\partial t} = -a_o p(\xi,t)\ln\xi + p(\xi,t) \sum_{n=1}^{\infty} a_n (n-1)!\,[\frac{1}{\xi^n} - 1]$$

$$+\; p(\xi+1,t) E_o I_1(\xi) \tag{25}$$

$$\exp\,(-a_o t\, \ln\xi)\; \frac{\partial[p(\xi,t)\exp(a_o t\, \ln\xi)]}{\partial t} = p(\xi,t) \sum_{n=1}^{\infty} a_n (n-1)!\,[\frac{1}{\xi^n} - 1]$$

$$+\; p(\xi+1,t) E_o I_1(\xi) \tag{26}$$

Integrating over t

$$[p(\xi,t)\exp(a_o t \ln\xi)-p(\xi,0)]=\int_0^t \exp(a_o t' \ln\xi)\{p(\xi,t')\Theta_o(\xi) + p(\xi+1,t')\cdot$$

$$\cdot\ \Theta_1(\xi) + \ldots\}\, dt' \qquad (27)$$

$\Theta_1(\xi)$ is term when $\psi_1(u)$ replaces $\psi_o(u)$ in Eq. 22.

$$P(\xi,t) \simeq p(\xi,0)\exp(-a_o t \ln\xi)+\exp(-a_o t \ln\xi)\int_0^t\{p(\xi,0)\Theta_o(\xi)+\exp(a_o t'\ln(\tfrac{\xi}{\xi+1}))$$

$$\cdot\ p(\xi+1,0)\ \Theta_1(\xi) + \ldots\}\, dt'$$

$$= p(\xi,0)\exp(-a_o t \ln\xi)+tp(\xi,0)\Theta_o(\xi)\exp(-a_o t \ln\xi)+p(\xi+1,0)\exp(-a_o t \ln\xi)$$

$$\cdot\ \Theta_1(\xi)\int_0^t \exp(a_o t' \ln(\tfrac{\xi}{\xi+1}))dt' + \ldots \qquad (28)$$

$$\int_0^t \exp\,(a_o t' \ln(\tfrac{\xi}{\xi+1}))\, dt' = \frac{1}{a_o \ln(\frac{\xi}{\xi+1})}\,[\exp(a_o t \ln \tfrac{\xi}{\xi+1})-1] \qquad (29)$$

Substituting Eq. 29 back into Eq. 28

$$p(\xi,t) \simeq \exp(-a_o t \ln\xi)[1+t\,\Theta_o(\xi)]p(\xi,0)$$

$$+\ \Theta_1(\xi)\ [\frac{\exp(-a_o t \ln(\xi+1)-\exp(-a_o t \ln\xi)}{a_o[\ln\xi-\ln(\xi+1)]}]\cdot\ P(\xi+1,0)+\ldots \qquad (30)$$

Consider the ψ_o terms first

$$p_o(\xi,t) \simeq p(\xi,0)\ \exp(-a_o t \ln\xi)[1+t\Theta_o(\xi)]$$

$$= p(\xi,0)\xi^{-a_o t}[1+t\sum_{n=1}^{\infty} a_n(n-1)!(\frac{1}{\xi^n} - 1)] \qquad (31)$$

Taking the inverse transform of $p(\xi,t)$

$$n(y,t) \simeq \int_0^y n(y',0)F(y-y',t)dy' \qquad (32)$$

where

$$F(y,t) = L^{-1}\{\xi^{(-a_o t)}(1-t\sum_{n=1}^{\infty} a_n(n-1)!+t\sum_{n=1}^{\infty} a_n(n-1)!\ \xi^{(a_o t-n)}\}$$

$$= [1-t\sum_{n=1}^{\infty} a_n(n-1)!]\frac{y^{a_o t-1}}{\Gamma(a_o t)} + t\sum_{n=1}^{\infty}\frac{a_n(n-1)!}{\Gamma(n+a_o t)}\ y^{a_o t+n-1}$$

$$= [1-t\sum_{n=1}^{\infty} a_n\Gamma(n+a_o t)]\frac{y^{a_o t-1}}{\Gamma(a_o t)} + t\sum_{n=1}^{\infty} a_n\ y^{a_o t+n-1}$$

$$= y^{a_o t-1}\{[1-t\sum_{n=1}^{\infty} a_n\ \Gamma(n+a_o t)]\frac{1}{\Gamma(a_o t)} + t\sum_{n=1}^{\infty} a_n y^n\} \qquad (33)$$

Now

$$\sum_{n=1}^{\infty} a_n\Gamma(n+a_o t) = \sum_{n=1}^{\infty} a_n\int_0^{\infty}\exp\ (-y)y^{n+a_o t-1}dy$$

$$= \int_0^{\infty}\exp\ (-y)\ (\sum_{n=1}^{\infty} a_n y^n)y^{a_o t-1}dy \qquad (34)$$

and

$$\psi_o(y) = \sum_{n=1}^{\infty} a_n y^{n-1} + \frac{a_o}{y} \qquad (35)$$

Substituting Eqs. 34 and 35 into Eq. 33

$$F(y,t) = \frac{y^{a_o t-1}}{\Gamma(a_o t)}\left\{1-t\int_0^{\infty}[\psi_o(y')-\frac{a_o}{y}]y'^{a_o t}\exp(-y')dy'\right.$$

$$+ y^{a_o t}\ t[\psi_o(y) - \frac{a_o}{y}] \qquad (36)$$

In terms of energy variables F(y,t) becomes

$$F(\frac{E'}{E},t) = \frac{(\ln\frac{E'}{E})^{a_o t-1}}{\Gamma(a_o t)}\left\{1-t\int_0^{\infty}[\psi_o(y')-\frac{a_o}{y'}](y')^{a_o t}\exp(-y')dy'\right\}$$

$$+ (\ln\frac{E'}{E})^{a_o t}\ t\ \{\psi_o(y) - \frac{a_o}{y}\} \qquad (37)$$

Since

$$\psi_o(y) = \phi_o(v) \tag{38}$$

$$y = \ln \frac{E'}{E} \tag{39}$$

$$\exp\ (y) = \frac{E'}{E} \tag{40}$$

$$\exp\ (-y) = \frac{E}{E'} \tag{41}$$

$$v = 1 - \frac{E}{E'} = 1 - \exp\ (-y) \tag{42}$$

$$1-v = \exp(-y) \tag{43}$$

$$-y = \ln(1-v) \tag{44}$$

$$dy = \frac{dv}{1-v} \tag{45}$$

$$\psi_o(y) - \frac{a_o}{y} = \phi_o(v) + \frac{a_o}{\ln(1-v)} \tag{46}$$

Using Eqs. 38.-46., Eq. 37 becomes

$$F(\frac{E'}{E},t) = \frac{(\ln \frac{E'}{E})^{a_o t-1}}{\Gamma(a_o t)} \left\{ 1 - t \int_0^1 [\phi_o(v) + \frac{a_o}{\ln(1-v)}][\ln(\frac{1}{1-v})]^{a_o t} dv \right\}$$

$$+ (\ln \frac{E'}{E})^{a_o t}\ t \left\{ \phi_o(1 - \frac{E}{E'}) - \frac{a_o}{\ln \frac{E'}{E}} \right\} \tag{47}$$

Now, for the case including $\psi_1(v)$

$$\frac{\partial p(\xi,t)}{\partial t} = -a_o p(\xi,t) \ln\xi + p(\xi,t)\ \Theta_o(\xi) + p(\xi+1,t) I_1(\xi) \tag{48}$$

Integrating over t

$$p(\xi,t) = p(\xi,0)\exp(-a_o t \ln\xi) + \exp(-a_o t \ln\xi) \int_0^t p(\xi,0)\Theta_o(\xi) + \exp(a_o t' \ln(\frac{\xi}{\xi+1})$$

$$\cdot\ p(\xi+1,0)\ I_1(\xi) \Big\}\ dt' \tag{49}$$

Now expanding the exponential in the integrand

$$\exp(a_o t' \ln(\frac{\xi}{\xi+1}) \simeq 1+a_o t' \ln(\frac{\xi}{\xi+1}) + \ldots. \tag{50}$$

Then integrating over t, the second term yields

$$\int_0^t t' \, dt' \to \frac{t^2}{2} \tag{51}$$

which is higher order in t. [In the prior case, we have $\exp(a_o t \ln\xi)$ and this was <u>not</u> put = 1.]

Here,

$$\ln(\frac{1}{1+\frac{1}{\xi}}) = \frac{1}{\xi} - \frac{1}{2\xi^2} + \frac{1}{3\xi^2} - \ldots. \tag{52}$$

Taking the inverse Laplace transform

$$L^{-1} (\ln(\frac{1}{1+\xi})) = 1 - \frac{y}{2!} + \frac{y^2}{3!} - \ldots. \tag{53}$$

The first correction to $p_o(\xi,t)$ becomes

$$p_1(\xi,t) = \xi^{-a_o t} \, t \, p(\xi+1,0) \, I_1(\xi) \tag{54}$$

where

$$I_1(\xi) = E_o \int_0^\infty (\exp(-\xi u)-\exp(-u))\psi_1(u)du = E_o[L\{\psi_1(u)\}-\int_0^\infty \exp(-u)\psi_1(u)du] \tag{55}$$

If we let

$$\psi_1(u) = \sum_{n=0}^{\infty} b_n u^n \tag{56}$$

$$L\{\psi_1(u)\} = \sum_{n=0}^{\infty} n! \, b_n \, \xi^{-n-1} \tag{57}$$

The inverse transform of $p_1(\xi,t)$ becomes

$$n_1(y,t) = \int_0^y n(y',0)\exp(-y')\, E_o t\, F_1(y-y',t)dy' \qquad (58)$$

where

$$F_1(y,t) = \sum_{n=0}^{\infty} \frac{n!\, b_n y^{n+a_o t}}{(n+a_o t+1)} - \sum_{n=0}^{\infty} n!\, b_n x \frac{y^{a_o t-1}}{\Gamma(a_o t)} \qquad (59)$$

$$\sum_{n=0}^{\infty} n!\, b_n = \int_0^{\infty} (y'')^{a_o t}\, \psi_1(y'')\exp(-y'')dy \qquad (60)$$

Thus

$$n_1(y,t) = \int_0^y d\, y'\; n(y',0)\exp(-y')E_o t\Big\{(y-y')^{a_o t}\psi_1(y-y') - \frac{(y-y')^{a_o t-1}}{\Gamma(a_o t)}\int_0^{\infty}(y'')^{a_o t}\, \psi_1(y'')\exp(-y'')dy''\Big\} \qquad (61)$$

Since

$$y = \ln\frac{E_o}{E} \qquad (62)$$

$$E = E_o \quad \exp(-y) \qquad (63)$$

Eq. 61 may be rewritten in terms of the energy variables

$$n_1(E,t) = \int_E^{E_o} n(E',0)\, \frac{dE'}{E'}\, E' t(\ln\frac{E'}{E})^{a_o t}[\phi_1(v) - \frac{(\ln\frac{E'}{E})^{-1}}{\Gamma(a_o t)}\int_0^{\infty}(\ln\frac{E}{E''})^{a_o t}\cdot \psi_1\left(\frac{E}{E''}\right)\frac{dE''}{E}] \qquad (64)$$

Thus

$$n(E,t) = \int_E^{E_o} \frac{dE'}{E'}\, n(E',0)\Big\{\frac{(\ln\frac{E'}{E})^{a_o t-1}}{\Gamma(a_o t)}[1-t'\int_0^1[\phi_o(v) + \frac{a_o}{\ln(1-v)} + E'\phi_1(v)]\,(\ln\frac{1}{1-v})^{a_o t}dv] + t(\ln\frac{E'}{E})^{a_o t}[\phi_o(v) + \frac{a_o}{\ln(1-v)} + E'\phi_1(v)]\Big\} \qquad (65)$$

Now

$$v = 1 - \frac{E}{E'} \tag{66}$$

$$dv = \frac{dE''}{E'} \quad \text{in} \int_0^1 dv \tag{67}$$

Using Eqs. 66 and 67, eq. 65 becomes

$$n(E,t) = \int_E^{E_o} \left\{ \frac{dE'}{E'} n(E',0) \frac{(\ln\frac{E'}{E})^{a_o t-1}}{\Gamma(a_o t)} [1 - t \int_0^{E'} \frac{dE''}{E'} [\Phi_{L.W.}(E',E'') + \frac{a_o}{\ln(1-v)}](\ln \frac{1}{1-v})^{a_o t}] \right\} + t \int_E^{E_o} \frac{dE'}{E'} n(E',0)(\ln \frac{E'}{E})^{a_o t} \cdot$$

$$\cdot [\Phi_{L.W.}(E',E) + \frac{a_o}{\ln(\frac{E}{E'})}] \tag{68}$$

Note that in the integrand of the first term

$$\frac{1 \cdot \ln(E'/E)^{a_o t-1}}{E'\Gamma(a_o t)}$$

is the same as the probability derived by Heitler.[57]

Corrections for varying thickness in stopping muons. We had

$$\cdots\cdots \frac{(\log \frac{E'}{E})}{\Gamma(\overline{b\ell})} \left\{ 1 - \sum_i t_i \int \cdots\cdots \right\} + \text{----} \tag{69}$$

We will now average this expression for various $b\ell$'s.

$(b\ell)a\ell$ + CH + Cu + Air

$$\int_{(b\ell)a\ell + CH + Air} \frac{d(b\ell)}{(b\ell)} \quad \frac{b\ell}{\Gamma(1+b\ell)} \exp(\log(\log \frac{E'}{E}) \cdot (b\ell - 1)) \tag{70}$$

The (-1) in exp is not affected by ℓ variation. We approximate

$\Gamma(1+b\ell)$ by $\Gamma(1+\bar{b}\bar{\ell})$.

Then we get

$$\approx \frac{1}{\Gamma(1+\overline{b\ell})} \frac{1}{(b\ell)_{cu}} \left\{ \frac{(\log \frac{E'}{E})^{b\ell}}{\log(\log(E'/E))} \cdot \right.$$

$$\left. \cdot (b\ell - \frac{1}{\log(\log \frac{E'}{E})}) \right\}_{(b\ell)_{a\ell} + CH + Air}^{(b\ell)_{cu} + a\ell + CH + Air} \tag{71}$$

[Note: In the computer program $\bar{b}\bar{\ell}$ for Cu was taken as 1/2 actual thickness as the average. Thus here $(b\ell)_{cu}$ would be 2 x $\bar{b}\bar{\ell}_{cu}$ as computed.]

We also have to evaluate the singularity region. There we had:

$$n(\bar{E}) \left\{1\text{-SING}(\bar{E})\right\} \frac{(\log \frac{E+\Delta}{E})^{\bar{b}\bar{\ell}}}{\Gamma(1+\bar{b}\bar{\ell})} \tag{72}$$

This will now also be averaged to get

$$\approx \frac{1}{\Gamma(1+\bar{b}\bar{\ell})} \int [\log(\frac{E+\Delta}{E})]^{b\ell} \frac{db\ell}{(b\ell)_{cu}} = \tag{72}$$

$$= \frac{1}{\Gamma(1+\bar{b}\bar{\ell})} \frac{(\log\frac{E+\Delta}{E})^{(b\ell)_{A\ell+CH+Cu}} - (\log\frac{E+\Delta}{E})^{(b\ell)_{A\ell+CH}}}{(b\ell)_{cu} \log(\log\frac{E+\Delta}{E})}$$

$\Phi_{L.W}$ is the Lamb-Wheeler cross section for radiation of a photon in the frequency range $d\nu$ by incident electron of energy E_i (where $E_i \gg m_e c^2$).[50]

$$\Phi_{L.W.}\, d\nu = (\Phi_{INELASTIC} + \Phi_{ELASTIC})\, d\nu \tag{73}$$

where

$$\Phi_{INELASTIC}\, d\nu = \frac{Ze^4}{137 m_e^2 C^4} \frac{d\nu}{E_i^2 \nu} \left\{ [E_i^2 + E_f^2][\psi_i(\epsilon) - \frac{8}{3} \ln_e Z] - \frac{2}{3} E_i E_f \cdot [\psi_2(\epsilon) - \frac{8}{3} \ln Z] \right. \tag{74}$$

and

$$\Phi_{ELASTIC}\, d\nu = \frac{Z^2 e^4}{137 m_e^2 C^4} \frac{d\nu}{E_i^2 \nu} \left\{ [E_i^2 + E_f^2][\phi_1(\gamma) - \frac{4}{3} \ln Z] - \frac{2}{3} E_i E_f \cdot [\phi_2(\gamma) - \frac{4}{3} \ln Z] \right. \tag{75}$$

where

$$E_f = E_i - \nu = \text{final electron energy} \tag{76}$$

$$\gamma = \frac{100\, m_e C^2 h\nu}{E_i E_f\, Z^{1/3}} \tag{77}$$

$$\epsilon = \frac{1}{Z^{1/3}} \gamma \tag{78}$$

} arguments of Fermi-Thomas screening factors $\phi_{1,2}(\gamma)$ and $\psi_{1,2}(\epsilon)$.[50]

$\phi_1(\gamma)$ and $\phi_2(\gamma)$ were taken from Figure 2, page 862 of Wheeler Lamb, P.R. 55, 858, (1939), up to a value of $\gamma = 1.42$. The values for $\psi_{1,2}(\epsilon)$ were obtained from Figure 1, page 862 up to $\epsilon = 1.50$. For larger values of the argument ϵ, ψ was obtained from the expression for free electrons $\psi_{1,2} = 19.19 - 4 \ln_e \epsilon$.

From $\gamma = 1.42$ to 2.0 the values for $\phi_1(\gamma)$ and $\phi_2(\gamma)$ were taken from the extended curves in Rossi, page 49, Figure 2.11.1.

The remaining values of $\phi_1(\gamma)$ and $\phi_2(\gamma)$ were obtained from the formula $\phi_1(\gamma) = \phi_2(\gamma) = 19.1 - 4 \ln_e \gamma - 4\, C(\gamma)$ where the function

$C(\gamma)$ was obtained from Table I, page 49.[55]

C. Ionization Straggling

The following formulae are from a paper by Rohrlich and Carlson[52] in which account is taken of the differences in straggling of electrons and positrons.

$$L^{\pm}(E_i,E_f) = (1/\xi)f^{\pm}(x,\Delta)d\Delta = (1/\xi)\exp[-\alpha^{\pm}(\lambda+\ln\alpha^{\pm})]\phi(\lambda)d\lambda \qquad (1)$$

$$\xi = x\,\frac{2\pi N_o e^4 \rho}{mv^2}\,\frac{\Sigma Z}{\Sigma A}\ (g/cm^2) \qquad (2)$$

N_o = Avogadro's number

ρ = density (g/cm^3)

m = mass of electron (gms)

e = charge of incident particle

Z = atomic number

A = atomic weight

x = thickness (g/cm^2)

v = velocity of incident particle

$$\alpha^{\pm} = C^{\pm}\xi \qquad (3)$$

$$C^{+} = \beta^2[2-(\gamma+1)^{-2}]\ ,\ \gamma = 1/1-\beta^2 \qquad (4)$$

$$C^{-} = (2\gamma-1)/\gamma^2 \qquad (5)$$

$$\xi = NZ\cdot\left(\frac{2\pi e^4}{mv^2}\right)\cdot x/T\ ,\ T = (\gamma-1)mc^2 \qquad (6)$$

$\lambda = (\Delta-\Delta_o)/\xi$, Δ = energy loss, Δ_o = most probable energy loss (7)

$$\phi(\lambda) = (1/2\pi i)\int_{-i\infty+\sigma}^{i\infty+\sigma} \exp(u \ln u + \lambda u)du \tag{8}$$

$\phi(\lambda)$ is Landau's distribution function.[51] $L^{\pm}(E_i,E_f)$ reduces to $\phi(\lambda)$ when $C^{\pm} = 0$.

Landau numerically evaluated $\phi(\lambda)$ out to $\lambda = 15$. For the infrequent large collision losses Landau derived an expression for the tail of the straggling function given by

$$\phi = \frac{1}{\omega(\omega+1)} \tag{9}$$

where ω is obtained by numerical interpolation from the relation

$$\lambda = \frac{\Delta-\Delta_o}{\xi} = \omega+\ln\omega - 0.37 \tag{10}$$

Values for Δ_o are obtained from formulas derived by Sternheimer[59] for the various materials through which the decay electrons pass.

D. Chi Square Test

The chi square test is used to estimate the degree of agreement between the theoretically predicted number of events in each focal plane counter with the number actually counted.

$$X^2_{\pm} = \sum_{i=1}^{11} [(\alpha\, N^i_{THEOR.} - N^i_{EXPTL.})/\epsilon^i]^2_{\pm} \tag{1}$$

$N^i_{EXPTL.}$ is the measured (TARGET IN-TARGET OUT) number of events in the ith counter (corrected for counter efficiency) both normalized to the same incident beam flux.

$$N^i_{EXPTL} = \left(\frac{\Sigma^i_{IN}}{\Sigma_{IN}(W_1)} - \frac{\Sigma^i_{OUT}}{\Sigma_{OUT}(W_1)}\right)/eff_i \tag{2}$$

The + and - refer to the positive and negative data respectively. α is a scale factor which slides the unnormalized N^i_{THEOR} up or down on the semi-log scale such that X^2 is a minimum. ϵ^i is the error on N^i_{EXPTL} and includes an estimated systematic error of $\sim 5\%$ as well as the statistical errors made during target in-out data runs.

$$\epsilon^i = \sqrt{\left[\left(\frac{\partial N^i_{EXPTL}}{\partial \Sigma^i_{IN}}\right)^2 (\epsilon^i(\Sigma^i_{IN}))^2 + \left(\frac{\partial N^i_{EXPTL}}{\partial \Sigma^i_{OUT}}\right)^2 (\epsilon^i(\Sigma^i_{OUT}))^2 + \left(\frac{\partial N^i_{EXPTL}}{\partial\, eff_i}\right)^2 (\epsilon_i(eff))^2\right]} \tag{3}$$

$$\frac{\partial N^i_{EXPTL}}{\partial \Sigma^i_{IN}} = \frac{1}{\Sigma_{IN}(W_1)\cdot eff_i} \tag{4}$$

$$\frac{\partial N^i_{EXPTL}}{\partial \Sigma^i_{OUT}} = \frac{-1}{\Sigma_{OUT}(W_1)\cdot eff_i} \tag{5}$$

$$\frac{\partial N^i_{EXPTL}}{\partial (eff_i)} = -\frac{1}{(eff_i)^2}\cdot\left(\frac{\Sigma^i_{IN}}{\Sigma_{IN}(W_1)} - \frac{\Sigma^i_{OUT}}{\Sigma_{OUT}(W_1)}\right) \tag{6}$$

$$(\epsilon^i(\Sigma^i_{IN}))^2 = \Sigma^i_{IN} \tag{7}$$

$$(\epsilon^i(\Sigma^i_{OUT}))^2 = \Sigma^i_{OUT} \tag{8}$$

Substituting Equations (4) through (8) into Equation (3),

$$\epsilon^i = \sqrt{\left[\frac{\Sigma^i_{IN}}{(\Sigma_{IN}(W_1)\cdot eff_i)^2} + \frac{\Sigma^i_{OUT}}{(\Sigma_{OUT}(W_i)\cdot eff_i)^2} + \frac{1}{(eff_i)^2}\left(\frac{\Sigma^i_{IN}}{\Sigma_{IN}(W_1)} - \frac{\Sigma^i_{OUT}}{\Sigma_{OUT}(W_1)}\right)^2 \cdot \left(\frac{\epsilon_i(eff_i)}{eff_i}\right)^2\right]} \tag{9}$$

Factoring out

$$N^i_{EXPTL} = \frac{\Sigma^i_{IN}}{\Sigma_{IN}(W_1)} - \frac{\Sigma^i_{OUT}}{\Sigma_{OUT}(W_1)} \tag{10}$$

$$\epsilon^i = N^i_{EXPTL} \sqrt{\left[\frac{\Sigma^i_{IN}}{(\Sigma_{IN}(W_1)\cdot eff_i \cdot N^i_{EXPTL})^2} + \frac{\Sigma^i_{OUT}}{(\Sigma_{OUT}(W_1)\cdot eff_i \cdot N^i_{EXPTL})^2} + \left(\frac{\epsilon_i(eff_i)}{eff_i} \right)^2 \right]} \tag{11}$$

E. Summary of Systematic Errors

Table VII. Summary of Systematic Errors in Calculated Corrections

Calculated Correction	Estimate of error (%) (approximate)
1. Solid Angle	1.0
2. Focal Plane Counter Efficiencies	4.0
3. Energy Losses	2.0
4. Non-uniform Target Stopping Distribution	2.0

F. OMEGAH Orbit Tracking Program

The initial momentum, the spatial coordinates and the direction of the electron orbit were generated using the Monte Carlo technique. The spatial coordinates of the electron were determined relative to a Cartesian coordinate system. The Z and X axis were parallel to the

median plane of the spectrometer while the y axis lay normal to the pole tips.

From measurements of the axial field components furnished by LRL Magnet Testing Group, (good to 0.1%) polynomial expressions for the magnitude of the axial field as a function of the spatial coordinates were derived.

The orbit was treated as being a sequence of small helical arcs. The step from the beginning of each arc to its end was determined using the following matrix transformation,

$$\begin{bmatrix} \Delta x_i \\ \Delta y_i \\ \Delta z_i \end{bmatrix} = \begin{bmatrix} A & 0 & B \\ 0 & \delta \tan \psi & 0 \\ B & 0 & -A \end{bmatrix} \begin{bmatrix} \rho_i \cos \bar{\theta}_i \\ \rho_i \\ \rho_i \sin \bar{\theta}_i \end{bmatrix}$$

where

$$x_{i+1} = x_i + \Delta x_i$$

$$y_{i+1} = y_i + \Delta y_i$$

$$z_{i+1} = z_i + \Delta z_i$$

$\rho_i = 1312\ pc/B_y(x,y,z)$, inches

δ = fixed angular increment

$A = 1 - \cos \delta$

$B = \sin \delta$

$\rho_i \delta$ = projection of helical arc in Z-X plane

ψ = angle orbit makes with median (Z-X) plane

$$\Delta\psi = -\frac{y}{\rho_i} \tan \epsilon$$

ϵ is the angle the orbit makes with the normal to the pole tip entrance (or exit). $\overline{\theta}_i$ is the angle the projection of the arc in the z-x plane makes with z axis.

The change in direction of the trajectory in the z-x plane is given by the following transformation

$$\begin{bmatrix} \sin \overline{\theta}_{i+1} \\ \cos \overline{\theta}_{i+1} \end{bmatrix} = \begin{bmatrix} (1-A) & B \\ -B & (1-A) \end{bmatrix} \begin{bmatrix} \sin \overline{\theta}_i \\ \cos \theta_i \end{bmatrix}$$

The orbit tracking continued until either the focal plane was crossed or the orbit crossed into an inaccessible region.

REFERENCES

1. R. B. Leighton, C. D. Anderson, and A. J. Seriff, Phys. Rev. 75, 1432 (1949).

2. J. Tiomno and J. A. Wheeler, Rev. Mod. Phys. 21, N. 1, 144 (1949).

3. L. Michel, Proc. Phys. Soc. A63, 514 (1950).

4. T. Muto, M. Tanifuji, K. Inoue and T. Inoue, Prog. Theor. Phys. 8, N. 1, 13 (1952).

5. L. Michel, Rev. Mod. Phys. 29, N. 2, 223 (1957).

6. T. D. Lee and C. N. Yang, Phys. Rev. 105, 1671 (1957).

7. R. P. Feynman and M. Gell-Mann, Phys. Rev. 109, 193 (1958).

8. T. D. Lee and C. N. Yang, Phys. Rev. 108, 1611, (1957).

9. A. Sirlin, Phys. Rev. 111, 337 (1958).

10. S. Bludman and A. Klein, Phys. Rev. 109, 550 (1958).

11. R. J. Finkelstein and R. E. Behrends, Phys. Rev. 97, 568 (1955). Also, Errata, Phys. Rev. 98, 1870 (1955).

12. T. Kinoshita and A. Sirlin, Phys. Rev. 107, 593 (1957).

13. S. M. Berman, Phys. Rev. 112, 267 (1958).

14. T. Kinoshita and A. Sirlin, Phys. Rev. 113, 1652 (1959).

15. C. E. Porter and H. Primakoff, Phys. Rev. 83, 849 (1951).

16. H. Uberall, Phys. Rev. 119, 365 (1960).

17. L. Tenaglia, Nuovo Cimento 13 284(1959).

18. V. Gilinsky and J. Mathews, Phys. Rev. 120, 1450 (1960).

19. R. W. Huff, Annals of Physics 16, 288 (1961).

20. K. W. Ford and J. G. Wills, Los Alamos Scientific Laboratory Report LAMS-2387 (1960)(unpublished).

21. L. Krueger and J. Rothleitner, Z. Physik 164, 330 (1961).

22. M. V. Terent'ev, Soviet Physics JETP 12, 1211 (1961).

23. A. Lagarrigue and C. Peyrou, J. Physics. Radium 12, 848 (1948).

24. H. J. Bramson, W. W. Havens Jr., and A. M. Seifert, Phys. Rev. 88, 304 (1952).

25. H. W. Hubbard, UCRL-1623.

26. J. A. Vilain and R. W. Williams, Phys. Rev. 94, 1011 (1954).

27. C. P. Sargent, M. Reinhart, L. M. Lederman, and K. C. Roger, Phys. Rev. 99, 885 (1955).

28. A. Bonnetti, R. Levi-Setti, M. Panetti, G. Rossi, and E. G. Tomasini, Nuovo Cimento 3, 33 (1956).

29. K. M. Crowe, R. H. Helm, and G. W. Tautfest. Proceedings of the Sixth Rochester Conference on High Energy Nuclear Physics, Preliminary Report 1956.

30. L. Rosenson, Phys. Rev. 109, 958 (1958).

31. A. O. Vaisenberg, Soviet Physics JETP 36, 722 (1959).

32. H. L. Anderson, T. Fujii, R. H. Miller, and L. Tau, Phys. Rev. Letters 2, 53 (1959).

33. W. Dudziak, R. Sagane, and J. Vedder, Phys. Rev. 114, 336 (1959).

34. R. A. Plano, Phys. Rev. 119, 1400 (1960).

35. M. M. Block, E. Fiorini, and T. Kikuchi. Proceedings of the Annual Internation Conference on High-Energy Physics at Rochester. University of Rochester. August 25-Sept.1,1960.

36. A. O. Vaisenberg, Soviet Physics USPEKHI 3, 195 (1960).

37. H. Kruger, UCRL-9322. Feb. 1961.

38. H. E. Bergeson, Thesis (Ph.D.) Univ. of Utah. (Aug. 1961).

39. G. Culligan, D. Harting, N. H. Lipman and G. Tibell, The Aix-En

Province International Conference on Elementary Particles. (Sept. 1961).

40. L. C. Nielsen. (Ph.D. Thesis) University of Utah. (1962).

41. A. Hogan, (Ph.D. Thesis) Catholic University of America

42. A. Vaisenberg, E. Pesolskaya, V. Smirnit-ski, Soviet Physics JETP 14, 734 (1962).

43. J. Barlow, P. S. L. Booth, L. J. Carroll, G. R. Court, J. D. Davies, D. N. Edwards, R. G. Johnson and J. R. Wormald. Proceedings Phys. Soc. 84, 239 (1964).

44. M. Bardon, P. Norton, J. Peoples, and A. M. Sachs, Phys. Rev. Letters 14, 449 (1965).

45. J. Bounin, R. Ehrlich, D. Fryberger, R. Powers, B. Sherwood, V. Telegdi, EFINS 66-8 University of Chicago (1965).

46. J. B. Pontecorvo and R. M. Sulyaev, Soviet JNP 1, N.2 (1965).

47. J. C. Sens, Phys. Rev. 113, 679 (1959).

48. J. Borggreen, B. Elbek and L. P. Nielsen, Nuc. Inst. and Methods 24, 1 (1963).

49. T. Nunamaker and A. Bjerke, Zero Crossing Coincidence Circuit (schematic 5 x 2374). 6342A Photomultiplier socket for Zero Crossing Coincidence. Schematic (5x2203).

50. W. T. Scott, Phys. Rev. 76, 213 (1949).

51. C. N. Yang, Phys. Rev. 84, 599 (1951).

52. J. A. Wheeler and W. E. Lamb, Phys. Rev. 55, 858 (1939).

53. L. Landau, Journ. of Phys. 8, 201 (1944).

54. F. Rohrlich and B. C. Carlson, Phys. Rev. 93, 38 (1954).

55. F. B. Hildebrand, Introduction to Numerical Analysis (1956)

McGraw Hill publishers New York, New York.

56. M. J. Berger and S. M. Seltzer, Nuclear Science Series, No. 39

57. B. Rossi, High Energy Particles (Published by Prentice-Hall, Englewood Cliffs, New Jersey, 1952).

58. P. A. M. Dirac, Proc. Cambridge Phil. Soc. 26, 361 (1930).

59. W. Heitler, The Quantum Theory of Radiation 3rd Edition, (Published by Oxford University Press, London, 1954),p.385.

60. K. Mitchell, Phil. Mag. 40, 351 (1949).

61. Private communication. D. G. Hill, Brookhaven National Laboratory (1964), mentioned an experiment using a 1/8" copper plate in a hydrogen bubble chamber with 5% energy resolution at 30 MeV.

This report was prepared as an account of Government sponsored work. Neither the United States, nor the Commission, nor any person acting on behalf of the Commission:

A. Makes any warranty or representation, expressed or implied, with respect to the accuracy, completeness, or usefulness of the information contained in this report, or that the use of any information, apparatus, method, or process disclosed in this report may not infringe privately owned rights; or

B. Assumes any liabilities with respect to the use of, or for damages resulting from the use of any information, apparatus, method, or process disclosed in this report.

As used in the above, "person acting on behalf of the Commission" includes any employee or contractor of the Commission, or employee of such contractor, to the extent that such employee or contractor of the Commission, or employee of such contractor prepares, disseminates, or provides access to, any information pursuant to his employment or contract with the Commission, or his employment with such contractor.